ΣΤΑΥΡΟΥΛΑ ΜΠΕΓΝΗ

ΣΧΟΛΗ ΜΗΧΑΝΟΛΟΓΩΝ ΜΗΧΑΝΙΚΩΝ

Τεχνο-οικονομική αξιολόγηση της επίδρασης του μεγέθους ενός αερόψυκτου συμπυκνωτή σε συστήματα Οργανικού κύκλου Rankine

Τομέας: Θεμότητας

Επιβλέπων: Κωνσταντίνος Μπραϊμάκης, Επίκουρος Καθηγητής ΕΜΠ

Αθήνα 2024

STAVROULA BEGNI

SCHOOL OF MECHANICAL ENGINEERING

A techno-economic evaluation of the impact of the sizing of an air-cooled condenser of ORC systems

Section: Thermal engineering

Supervisor: Konstantinos Braimakis. Assistant Professor NTUA

Athens 2024

<u>Υπεύθυνη δήλωση</u> για λογοκλοπή και για κλοπή πνευματικής ιδιοκτησίας:

Έχω διαβάσει και κατανοήσει τους κανόνες για τη λογοκλοπή και τον τρόπο σωστής αναφοράς των πηγών που περιέχονται στον οδηγό συγγραφής Διπλωματικών Εργασιών. Δηλώνω ότι, από όσα γνωρίζω, το περιεχόμενο της παρούσας Διπλωματικής Εργασίας είναι προϊόν δικής μου εργασίας και υπάρχουν αναφορές σε όλες τις πηγές που χρησιμοποίησα.

Οι απόψεις και τα συμπεράσματα που περιέχονται σε αυτή τη Διπλωματική εργασία είναι του συγγραφέα και δεν πρέπει να ερμηνευθεί ότι αντιπροσωπεύουν τις επίσημες θέσεις της Σχολής Μηχανολόγων Μηχανικών ή του Εθνικού Μετσόβιου Πολυτεχνείου.

Σταυρούλα Μπεγνή

Ευχαριστίες

Φτάνοντας στο τέλος της Διπλωματικής μου εργασίας και εν γένη της ακαδημαϊκης μου πορείας ως προπτυχιακή φοιτήρια, θα ήθελα να ευχαριστήσω τους ανθρώπους που ήταν δίπλα μου σε αυτό το ταξίδι.

Αρχικά, θα ήθελα να ευχαριστήσω τον υπεύθυνο καθηγητή της Διπλωματικής εργασίας, Κωνσταντίνο Μπραϊμάκη, για την εμπιστοσύνη που μου έδειξε, την άριστη συνεργασία και την άμεση καθοδήγηση σε όλη τη πορεία της Διπλωματικής μου εργασίας.

Θα ήθελα επίσης να ευχαριστήσω τους Ludwig Irrgang και Christopher Schifflechner από το Τεχνικό Πανεπιστήμιο του μονάχου (Technical University of Munich-TUM) για τη συνεργασία και τη καθοδήγηση σε ζητήματα της μοντελοποίησης του συστήματος στο πλαίσιο της εργασίας.

Θα ήθελα επίσης να ευχαριστήσω τους γονείς μου και τα αδέρφια μου Ελένη και Γιάννη για την στήριξη και την φροντίδα όλα τα χρόνια των σπουδών μου.

Περίληψη

Στην παρούσα μελέτη παρουσιάζεται μια τεχνο-οικονομική αξιολόγηση της επίδρασης των αερόψυκτων συμπυκνωτών με πτερύγια στα συστήματα οργανικού κύκλου Rankine. Η παρούσα διπλωματική εργασία στοχεύει στην ανάπτυξη ενός ενοποιημένου μοντέλου για την διαστασιολόγηση ενός αερόψυκτου συμπυκνωτή, ενσωματωμένου σε συστήματα ORC, και στη διεξαγωγή μιας παραμετρικής έρευνας στις βασικές θερμοδυναμικές και οικονομικές παραμέτρους του συστήματος.

Για τη διαστασιολόγηση του αερόψυκτου συμπυκνωτή (ACC), έχει αναπτυχθεί ένα ολοκληρωμένο μοντέλο σε κώδικα Matlab όπου ενσωματώθηκε σε ένα υπάρχον μοντέλο ORC. Για τη διεξαγωγή της παραμετρικής έρευνας, η ανάλυση επικεντρώνεται σε τέσσερις κύριες μεταβλητές: δύο μεταβλητές σχεδίασμου ORC (την ελάχιστη θερμοκρασιακή διαφορά αέρα-εργαζόμενου ρευστού κατά τη συμπύκνωση (PP_{ACC}) και την αύξηση της θερμοκρασίας του αέρα στον ACC (ΔT_{air})) και δύο γεωμετρικές μεταβλητές ACC (τον αριθμός των πάσων κάθε σωλήνα (N_{tp}) και το μήκος του σωλήνα του ACC (L_t)). Ένα πλήθος παραμέτρων διερευνώνται μεταβάλλοντας αυτές τις μεταβλητές σχεδιασμού, συμπεριλαμβανομένης της απαιτούμενης μεταφοράς θερμότητας ACC, της κατανάλωσης ισχύος του ανεμιστήρα του ACC, της καθαρής ισχύος εξόδου ORC και του ειδικού κόστους.

Τα αποτελέσματα της παραμετρικής ανάλυσης υπογραμμίζουν την ανάγκη για αντιστάθμιση μεταξύ της επιφάνειας μεταφοράς θερμότητας του ACC, της κατανάλωσης ισχύος του ανεμιστήρα ACC και της ηλεκτρικής απόδοσης του ORC. Μεταξύ των παραμέτρων που εξετάστηκαν, μελετήθηκε εκτενώς το ειδικό κόστος ανά kW παραγόμενης ισχύος του ACC το οποίο συνδυάζει τόσο θερμοδυναμικούς όσο και οικονομικούς παράγοντες στην ανάλυση. Μέσα από την ανάλυση προέκυψε ως βέλτιστο σημείο σχεδιασμού $PP_{ACC} = 14K, \Delta T_{air} = 30K, L_t = 10m$ $και$ $N_{tp} = 6.$ $με$ $C_{ACC,sp} = 1459\ USD/kWe$, ένα σχετικά υψηλό κόστος σε σύγκριση με το κόστος επένδυσης συστημάτων ORC.

Abstract

In the present study, a techno-economical assessment of the impact of finned air-cooled condensers in the Organic Rankine systems is presented. The thesis aims to develop a unified sizing model of the air-cooled condenser, integrated into ORC systems, and conduct a parametric investigation in the key thermodynamic and economic parameters of the system.

For the sizing model of the air-cooled condenser (ACC), a comprehensive model has been developed in Matlab code where it was combined with an existing ORC model. To conduct the parametric investigation, the analysis focuses on four primary variables: two ORC design variables (the condenser pinch point and air temperature rise in the ACC) and two ACC geometric variables (the number of tube passes and the length of the ACC tubes). Various parameters are investigated by varying these design variables, including ACC heat transfer area, ACC fan power consumption and, ORC net power output.

The results of the parametric investigation highlight the trade-off between the ACC heat transfer area, the ACC fan power consumption, and the electrical efficiency of the ORC. Among the parameters examined, the specific cost of the air-cooled condenser was introduced to combine both the thermodynamic and economic factors in the analysis. Through the analysis, it emerged as an optimal design point of $PP_{ACC} = 14K$, $\Delta T_{air} = 3, L_t = 10m,$ and $N_{tp} = 6$. with a $C_{ACC,sp} = 1459\ USD/kWe$, a relatively high cost compared to ORC investment costs.

Contents

List of Figures

List of Tables

Nomenclature

Abbreviations

ACC	air-cooled condenser
ORC	Organic Rankine Cycle
WHR	Waste Heat Recovery

Variables

A	area	(m^2)
C	cost	(USD)
d	diameter	m
e	temperature effectiveness	(-)
F	Correction factor	(-)
h	specific enthalpy	kJ/kg
k	the thermal conductivity	[W/m/K]
L	length	(m)
$\dot{m}$	mass flow rate	kg/s
N	number of tubes	(-)
Nu	Nusselt number	(-)
P	power	kW
p	pressure	Pa
Pr	Prandtl number	(-)
$\dot{Q}$	heat duty	kW
Re	Reynolds number	(-)
T	temperature	(K)
t	thickness	(m)
U	overall heat transfer coefficient	(kW/m^2K)
$\dot{V}$	volumetric flow rate	(m^3/s)
u	velocity	(v/s)
v	kinematic viscosity	(m/s2)
W	Width of ACC	(m)
x	vapor quality	(-)

Greek symbols

α	heat transfer coefficient	(kW/m^{2}K)
Δ	difference	-
η	efficiency	-
ξ	Drag efficiency	
ρ	density	kg/m^3

Subscripts

air	air
bare	base cost of ACC
c	cold
circle	circle area of the fin
cond	condensation
crit	critical point
D	Darcy
des	desuperheating
e	electricity
evap	evaporator
f	fin
face	face
fan	air-cooled condenser fan
fw	weighted fin
g	saturated phase
h	hot
i	about the inlet state
in	inlet
is	isentropic
lm	logarithmic mean
M	Metal
max	maximum
mean	mean
net	net

nom	outside the
o	outside, related to the outlet state
oil	heat transfer oil
p	tube pitch
periphery	fin periphery
pp	pinch point
pump	pump
rec	recuperator
red	reduced
rel	relative to design value
rp	rows per pass
t	total number of tubes
tot	total
tp	tube passes
tube	tube
turb	turbine
wf	working fluid
x	x direction, direction perpendicular to the airflow
y	y direction, in the flow direction

1. Introduction

1.1 Organic Rankine Cycle (ORC)

The history of ORC dates back to the 19th century and extends to the modern era. H. E. Willsie constructed the first two solar ORC systems, with capacities of 4.5 kW and 11 kW, using sulfur dioxide as the working fluid in 1904. Subsequently, in 1940, Luigi D'Amelio designed a geothermal ORC system using ethylene as the working fluid. The unit operated until 1950. Regarding commercial ORC installations, companies such as Ormat and Turboden lead the industry, providing solutions for waste heat recovery (WHR) in various industrial applications (oil and gas, biomass, cement, glass processing industries, etc.). Ormat has installed more than 3,000 units ranging from 4 kW and more than 500 units from 1 to 25 MW [1]. The first commercial ORC systems, utilizing solar and geothermal energy sources, emerged between the 1970s and 1980s. A large number of ORC installations have been deployed in countries such as the United States, Canada, Italy, and Germany, although applications have been observed in countries such as Finland, Belgium, Swaziland, Austria, Russia, Romania, India, and Morocco [2].

ORC shares the same operating principles as the conventional Steam Rankine Cycle (SRC) implemented in steam turbine power plants. It is a power generation cycle that is typically implemented for the conversion of thermal energy to power at low temperatures (<300℃) and/or power capacities from few kW to tens of MW [3]. In Figure 1.1 a 200 kW ORC system for wasted heat recovery is depicted as well as in Figure 1.2 a 5 MWe Geothermal ORC plant in Germany.

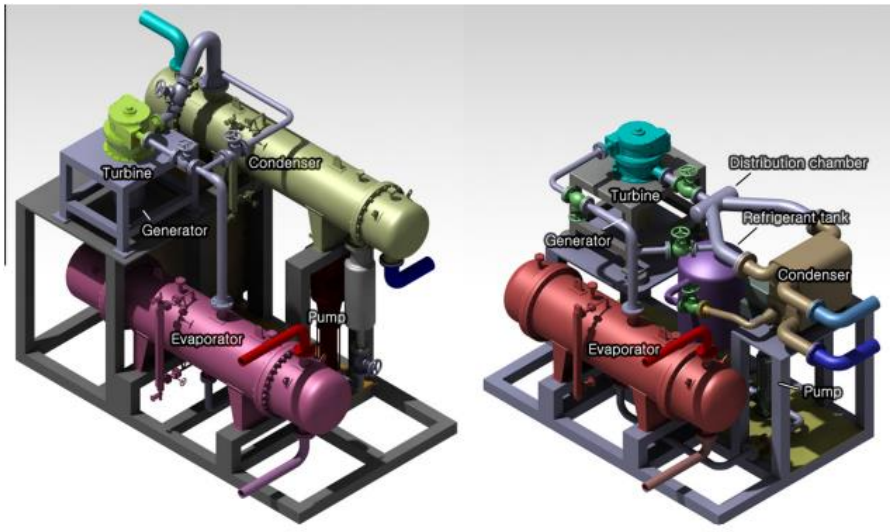

Figure 1.1: 200 kW ORC system for waste heat recovery [4]

Figure 1.2: 5.6 MWe Geothermal ORC plant in Germany [5]

As the name implies, the main feature of the ORC is the use of organic substances (such as alkanes, hydrofluorocarbons, hydrofluoroolefins, and siloxanes) as working fluids instead of water-steam [6] [7]. Furthermore, organic fluids allow the use of only one heat exchanger since their vaporization does not occur gradually (preheating-evaporation-superheating) as with water, but through a single process. [8].

In Figure 1.3 an ORC conceptual design with subcooler and recuperator is displayed

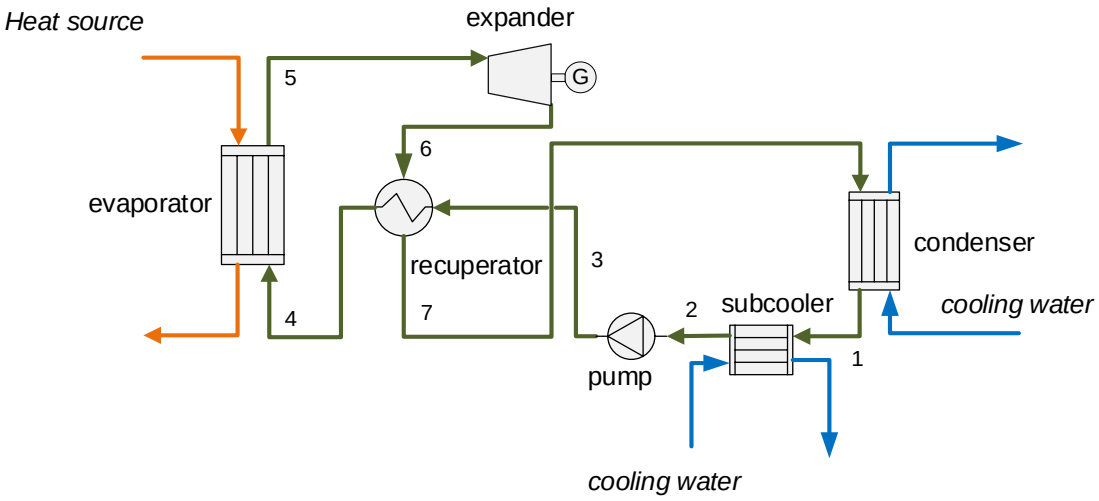

Figure 1.3 Organic Rankine Cycle (ORC) conceptual layout with sub-cooler and recuperator

The saturated liquid organic working fluid (refrigerant) exits the condenser and is subcooled (1-2) and pressurized in a pump (2-3), and subsequently heated up by the heat source in a heat exchanger (evaporator) turning into saturated or superheated vapor (4-5). The pressurized hot vapor exiting the evaporator is then driven to an expander and expands to produce mechanical power (5-6), which is then converted to electricity through a generator. The working fluid leaving the expander can then be used for preheating the liquid refrigerant leaving the pump (6-7 and 3-4) through an internal heat exchanger (recuperator). Eventually, it is driven to the condenser, where it is cooled down by a cooling fluid and condensed (7-1), before recirculating into the pump to repeat the processes. It has to be noted that the liquid refrigerant subcooler in the ORC does not constitute a fundamental process of the thermodynamic cycle neither the recuperator. However, subcooling is necessary as a measure to prevent cavitation from occurring in the refrigerant pump by providing enough net positive suction head (NPSH), a common issue in similar micro-scale ORC prototype. Recuperators contribute to the increase of the efficiency of the ORC. In Figure 1.4 the simplest conceptual layout of the ORC system is presented along with the T-S diagram.

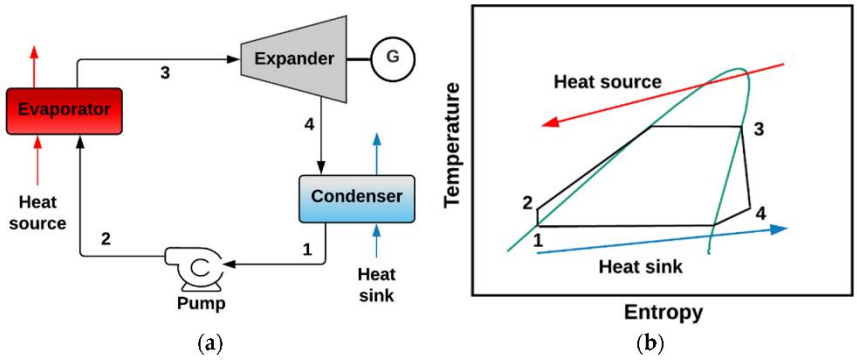

Figure 1.4: (a) ORC simplest conceptual layout, (b) T-S diagram for ORC cycle [9]

The efficiency of the organic Rankine cycle is relatively low, mainly due to the low operating temperatures. For this reason, various arrangements have been proposed to increase the cycle's efficiency, with the addition of a recuperator being the most prominent as mentioned. The recuperator's influence heavily relies on the heat source that is available and with its use final thermal efficiencies over 20% can be achieved [10]. The recuperator operates as a heat exchanger between the steam flow exiting the expander and the cooler flow of the working fluid before it enters the evaporator. Through this process, a reduction in the heat supplied to the cycle is achieved, thus increasing its efficiency. This arrangement is typically applied in cases where the working fluid has a positive slope on the saturation curve (dry fluids) and there is a greater margin for heat recovery [11-15]. Other arrangements proposed to increase the efficiency of the organic Rankine cycle include

regenerative preheating, supercritical cycles, multistage expansion, and the use of zeotropic mixtures as working fluids [6].

The key design boundary conditions of ORCs are the heat source stream (exhaust gas, heat transfer fluid, hot water, etc.) composition, mass flow rate, and temperature profile, which typically constrain and guide the selection of the maximum cycle temperature/pressure, as well as the cooling fluid type and available temperature (heat sink), which poses a lower bound on the minimum cycle temperature/pressure. Typically, the higher the difference between the maximum and lower temperature/pressure, the higher the thermal efficiency (electrical power output per unit of thermal input) of the cycle.

1.1.1 Thermal Sources

ORC's significant advantage is the flexibility it displays in terms of utilizing various heat sources on a wide temperature range [16]. These heat sources can be categorized into several distinct types, each offering unique advantages and challenges:

Waste heat recovery (WHR) *via* the Organic Rankine Cycle (ORC) is one of the most promising solutions to improve the overall efficiency of thermal processes and reduce fossil fuel consumption and associated greenhouse gas (GHG) emissions through the generation of electric power in industrial and transportation sectors [17-19]. It has been noted that over 50% of industrial waste heat is categorized as "low temperature" (meaning less than 230°C) [20]. For this reason, the ORC can be a viable and extremely useful technology as its main advantage lies in the utilization of low and medium-temperature heat. In waste heat recovery applications, the heat source typically consists of exhaust gas from engines or industrial processes. Efficient integration of waste heat recovery ORCs (WHR-ORCs) into heat sources that exhibit temporal variability regarding their temperature levels and mass flow rate is critical for maximizing electricity generation and energy savings, however, it requires accurate prediction of their performance under diverse operating conditions.

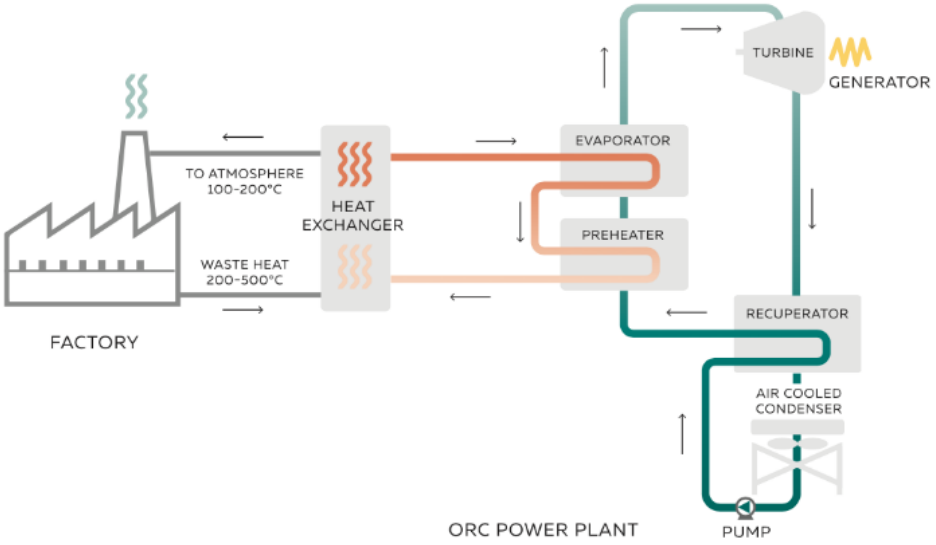

Figure 1.5: Wate heat recovery ORC system (WHR-ORCs) [21]

Solar Thermal Energy: Solar energy, abundant and renewable, presents a viable heat source for ORC systems, particularly in regions with ample sunlight. Concentrated solar power (CSP) systems concentrate solar radiation to produce high-temperature heat, which can be utilized by ORC systems to generate electricity [10].

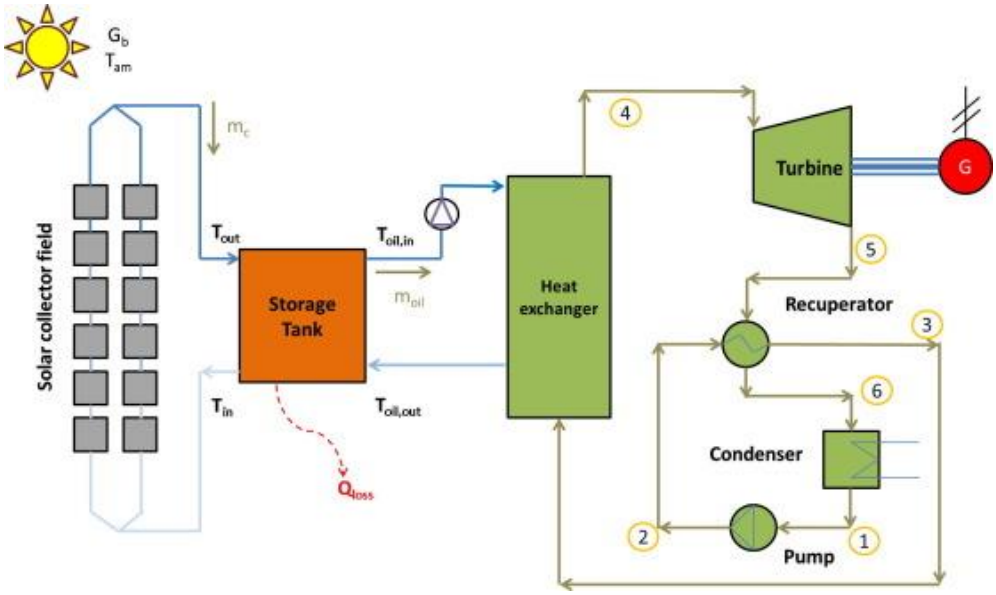

Figure 1.6: Integration of solar power system with ORC [22]

Geothermal Heat: Geothermal reservoirs, located beneath the Earth's surface, contain vast reservoirs of heat energy. ORC systems can tap into these geothermal resources, extracting heat from hot water or steam to drive power generation turbines. This application is particularly prevalent in areas with geothermal activity, such as geysers and hot springs [8].

Biomass Combustion: Biomass, derived from organic materials such as agricultural residues, forestry waste, and dedicated energy crops, can be combusted to produce heat for ORC systems. Biomass combustion not only provides a renewable heat source but also offers opportunities for waste management and carbon mitigation [8].

The utilization of diverse heat sources underscores the versatility and applicability of ORC systems. By harnessing low-grade heat from industrial processes, solar radiation, geothermal reservoirs, biomass combustion, and exhaust gases, ORC systems offer a compelling solution for sustainable power generation.

1.1.2 Working fluids

One other important aspect of the ORC systems is the selection of the working fluid. Fluids are most commonly categorized according to the saturation curve of their T-s diagram. A typical T-s diagram including all 3 types is presented below (Figure 1.7).

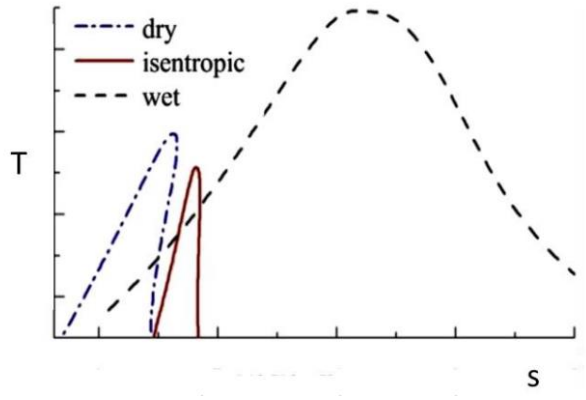

Figure 1.7: ***T-s diagrams for fluid types***

Fluids that display a positive vapor curve are referred to as dry, fluids with a nearly vertical curve are called isentropic and lastly, fluids with a negative vapor curve are described as wet. Water belongs in the last category, which mostly includes fluids of low molecular mass, while the highest is present

in dry fluids [7]. Wet fluids that operate at high pressures without being superheated lead to an increase in the percentage of the liquid state at the turbine's last stages. When the mixture contains a large percentage of liquid, the blades are greatly endangered by erosion and mechanical wear [23]. Hence, the practice of using a wet fluid without superheating is not recommended.

Most organic fluids demonstrate negative environmental effects and therefore two main indexes have been introduced that quantify their impact. The first one is called ODP (Ozone Depletion Potential) and is related to the destruction of the Ozone's layer and the second one is called GWP (Global Warming Potential) and is related to the atmosphere's temperature increase, due to their use. According to the Montreal Protocol that was signed in 1987, fluids that displayed high ODP values would not be permitted for use and thus, their replacement was deemed mandatory [24]. Besides their impact on the environment, organic fluids often present dangers for humans and the plant's overall safety, due to their toxicity, flammability, and corrosivity. Toxic fluids must be avoided because they are harmful to the plant's personnel when leakage occurs [11, 25, 26].

1.1.3 Condenser

In an ORC system, the condenser can be either water-cooled or air-cooled. Water-cooled condensers operate at lower temperatures of the cooling medium (approximately 22°C at an ambient temperature of 15°C - ISO conditions), while air-cooled condensers usually operate at higher temperatures of the cooling medium (approximately 35°C at an ambient temperature of 15°C) [11, 25, 26]. This results in water-cooled condensers being able to achieve higher cycle efficiency. However, they require a secondary circuit for the cooling water, which includes a pump and a cooling tower. The energy demand of the pump and the fans of the cooling tower is much higher than that of the fans of air-cooled condensers [27].

Air-cooled condensers are the primary choice for small systems but are also common for some large systems. This is mainly due to the limited availability of cooling water [28]. Water, if available, is a superior coolant and offers significant advantages in heat transfer characteristics, design flexibility, and opportunities for low-cost installation [29].

1.2 Air-cooled Condenser (ACC)

In this thesis an air-cooled condenser (ACC) will be used in the ORC system therefore in this section, further details on the characteristics of ACC will be presented.

Air-cooled condensers are integral components of thermal systems used for heat rejection in various industrial and commercial applications. One of the primary components of an air-cooled condenser is the finned tube bundle. The bundle consists of numerous finned tubes arranged in a configuration to maximize the heat transfer surface area [30]. The fins on these tubes serve to increase the heat transfer coefficient between the refrigerant inside the tubes and the ambient air flowing over the external surface [31]. In Figure 1.8 and Figure 1.9, both schematic and actual excamples of different forms of finned tubes are presented.

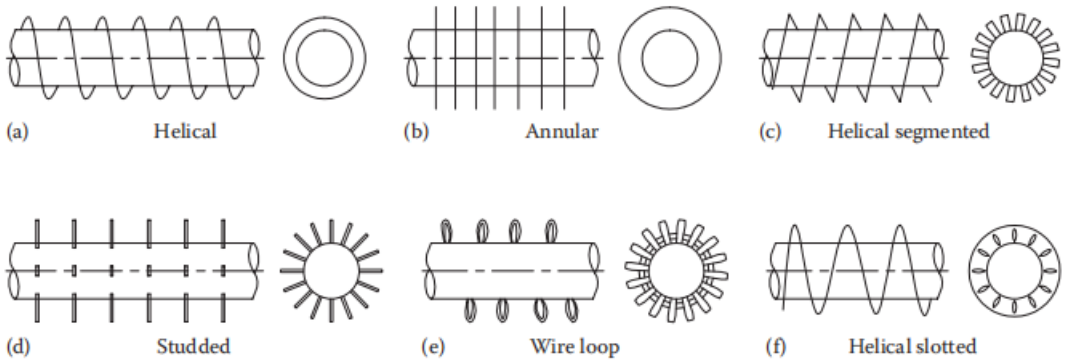

Figure 1.8: Forms of individually finned tubes. (a) Helical, (b) annular, (c) helical segmented, (d) studded, (e) wire loop, and (f) helical slotted.

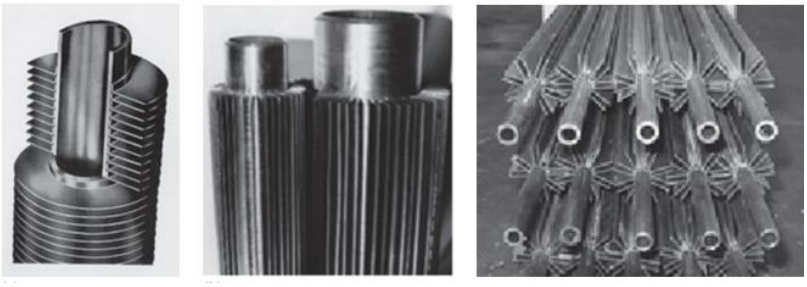

Figure 1.9: Finned tube heat exchanger examples

Air-cooled condensers can have 1,, 2, 3 or multiple configurations as presented in Figure 1.10. with each pass representing a path through which the refrigerant flows. In single-passe pass configuration, the refrigerant flows through the condenser tubes once before exiting, whereas in multi-pass

configurations, the refrigerant circulates through the condenser tubes multiple times to enhance heat transfer efficiency. The choice of the number of tube passes in an air-cooled condenser design is influenced by factors such as desired heat transfer performance, space limitations, and cost considerations.

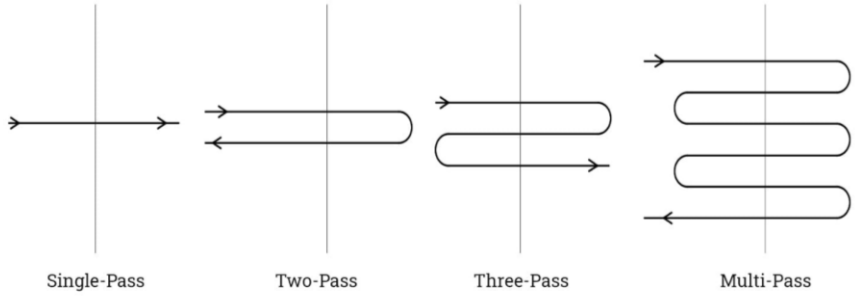

Figure 1.10: Types of passes [32]

Tube pitch is the distance from the center of 2 adjacent tubes. In air-cooled condensers various types of tube pitch can be found as displayed in Figure 1.11, influencing factors such as heat transfer performance, air-side pressure drop, and overall system efficiency [33].

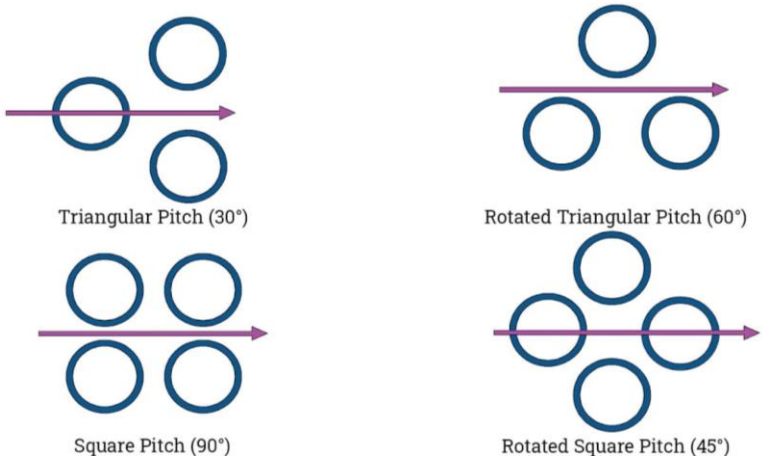

Figure 1.11: Various Types of Tube pitch

In addition to the finned tube bundle, air-cooled condensers feature axial fans or centrifugal blowers for inducing airflow across the finned surface. These fans draw ambient air into the condenser, where it absorbs heat from the refrigerant vapor, thereby facilitating the condensation process [34]. The design and configuration of these fans are crucial for ensuring adequate airflow and optimal heat transfer performance.

Air-cooled condensers are available in various configurations as displayed in Figure 1.12. In horizontal forced draft condensers (a), fans are positioned to force air over the finned tube bundle, while induced draft condensers, either horizontal (b) or vertical (c), utilize fans positioned to draw air through the bundle [35]. Both designs have their advantages and are selected based on factors such as space constraints, airflow requirements, and system efficiency. In Figure 1.12 the A-frame type (d) is also introduced where 2 tube bundles are placed angled with a forced draft fan.

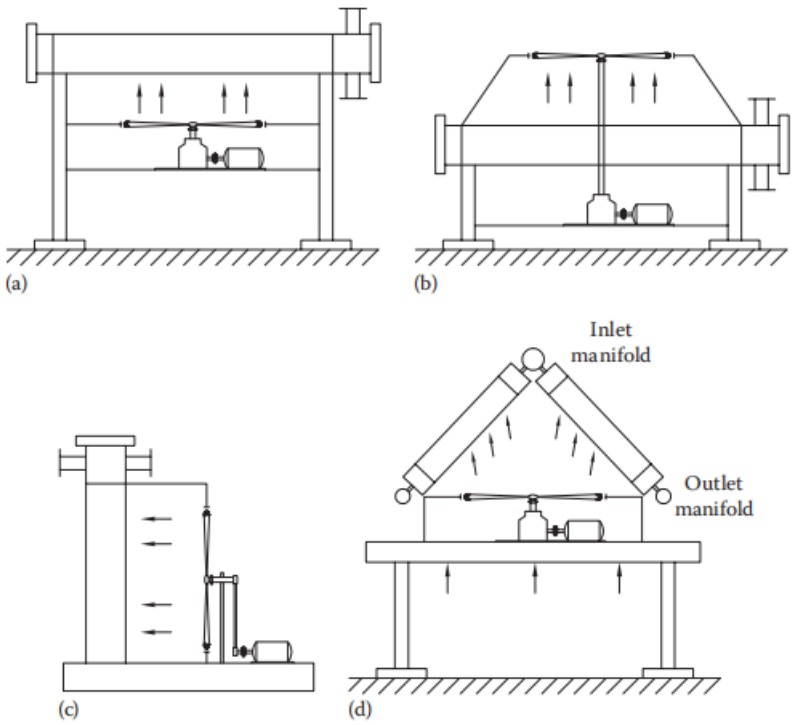

Figure 1.12: Orientation of ACC tube bundle—(a) horizontal, forced draft, (b) horizontal, induced draft, (c) vertical, and (d) A-frame [36]

Variations in tube bundle configurations are observed across various applications, with one common configuration being V-type air-cooled condensers (ACCs). In V-type ACCs, the tube bundles are arranged in a V-shaped configuration, contrasting with A-type ACCs where the tubes are aligned in the opposite direction. This configuration allows for efficient heat transfer and airflow distribution, particularly in industrial settings where space constraints and airflow optimization are critical considerations [33]. (Figure1.13)

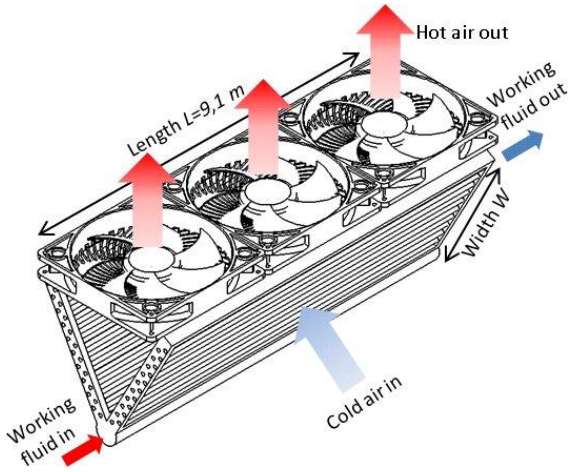

Figure1.13 : V-type air-cooled condenser [32]

Furthermore, air-cooled condensers may incorporate additional features such as louvers or dampers to control airflow and optimize heat transfer under varying operating conditions. Louvers are adjustable vanes located at the air inlet or outlet of the condenser, allowing for regulation of airflow rates and direction, while dampers enable modulation of air volume to maintain optimal system performance [37]. In Figure 1.14 and Figure 1.15, both small and large-scale air-cooled condenser (ACC) units are depicted, showcasing the diversity in size and capacity within the ACC technology.

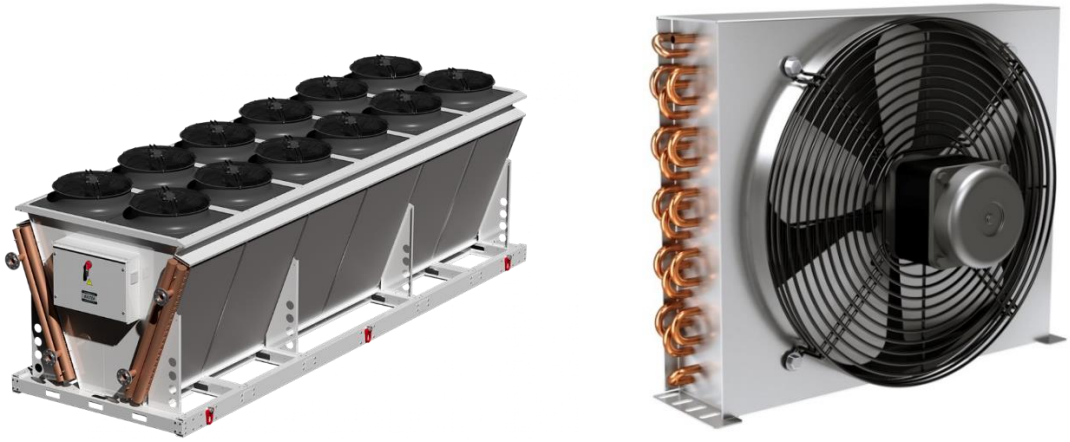

Figure 1.14: V-type ACC unit (left) and vertical ACC unit [38]

Figure 1.15 :6 MWe ORC installation withe the air-cooled condenser in Germany [39]

The performance of air-cooled condensers is influenced by factors such as ambient temperature, humidity, and air velocity [40]. Proper sizing and selection of condenser components, including fan size, tube geometry, and fin density, are critical for achieving the desired heat rejection capacity while minimizing energy consumption and operational costs.

1.3 Aim of the thesis

This thesis aims to comprehensively investigate the trade-offs inherent in the design and operation of Organic Rankine Cycle (ORC) systems, with a specific focus on the sizing of horizontal finned tube air-cooled condensers (ACCs). The primary objective is to develop a unified methodology for systematically exploring the relationship between ORC efficiency, ACC cost, and ACC fan power consumption, providing valuable insights into optimal design configurations.

To achieve this objective, the research will involve the development and integration of a comprehensive sizing model for horizontal finned tube ACCs within an existing ORC framework. The model will be utilized to conduct a parametric investigation focusing on four primary variables: two ORC design variables (the condenser pinch point and air temperature rise in the ACC) and two ACC geometric variables (the number of tube passes and length of the ACC tubes). By varying these design variables, various parameters will be investigated including ACC heat transfer area, ACC fan power consumption, ORC net power output, ACC specific cost.

Through this investigation, the study seeks to provide valuable insights into the techno-economic implications of ACC sizing in ORC systems. By examining how design variables interact with system performance indicators, the research aims to offer guidance to decision-makers, assisting in the creation of ORC system designs that are both efficient and cost-effective for a range of applications.

In summary, this structured investigation aims to advance understanding of the techno-economic implications of ACC sizing in ORC systems, contributing to the development of sustainable energy solutions.

2. Method

In this chapter, the modelling approach is described. The chapter is divided into three sections. In the first section, the ACC model is described in detail. In the second section, the ORC design model is described. In the third section, the integration of the ACC and ORC models is described. All models are developed in Matlab [41], while the thermophysical properties of all substances (working fluid, heat source, air) are calculated with REFPROP [42].

2.1 Air-cooled condenser modelling

In this chapter, a detailed methodology of the ACC modelling is presented. Figure 2.1 depicts the inputs and outputs of the model. There are two sets of inputs to the ACC model. The first set of inputs includes thermodynamic parameters: the ambient air pressure (p_{air}) and temperature ($T_{air,\mathrm{in}}$), the desired air temperature rise in the ACC (ΔT_{air}), as well as the working fluid mass flow rate ($\dot{m}_{wf}$), inlet temperature ($T_{wf,in}$) and desired desuperheating temperature difference of working fluid ($\Delta T_{wf,ds}$). The second set of inputs includes geometric parameters of the ACC: these are the tube internal (d_i) and external diameter (d_o), the fin diameter (d_f), spacing (L_{f}) and thickness (t_f), the tube length per pass (L_{t}), the tube pitch (L_{p}), the number of tube passes in the direction of flow (N_y) and the number of tube passes (N_{tp}).

The outputs of the model include certain geometric parameters of the ACC, namely the number of tubes in the direction that is perpendicular to the airflow (N_x), the width of the ACC (W_{tot}), the total required external heat transfer surface of the ACC (A_{ACC}), the face area of the ACC (A_{face}), the air-side pressure drop (ΔP_{air}), the ACC cost (C_{ACC}) and the electrical power consumption of the ACC fan ($P_{e,ACC,fan}$). A detailed description of the definitions of all these parameters is included in the following sections.

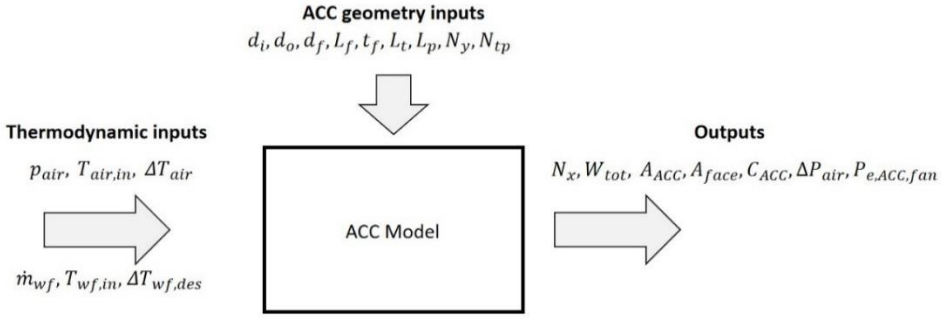

Figure 2.1: Inputs and outputs of the ACC model

2.1.1 Thermodynamic properties and energy balance

In the condenser, a heat exchange is happening between the air and the working fluid. In Figure 2.2 a diagram is presented to understand the phases of the condensation. The working fluid enters the ACC as superheated vapor (wf, in) and leaves it (wf, out) as saturated liquid (wf, sat). The desuperheating section covers the working fluid from the inlet state (wf, in) through the saturated vapor phase (wf, des, out). The condensation section covers the working fluid from saturated vapor to saturated liquid at the outlet of the ACC (wf, out). The air enters the condenser at a lower temperature (*air,in*) and it is heated by the working fluid to a higher temperature (air, out), undergoing a temperature rise equal to $\Delta T_{air.}$ At the point where the working fluid is a saturated vapor, the pinch point of the 2 streams (PP_{ACC}) is located.

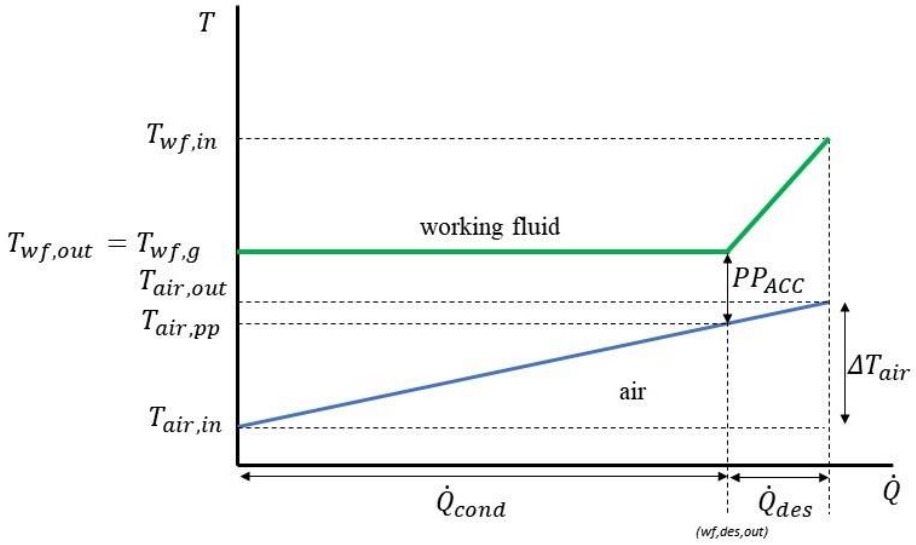

Figure 2.2: Temperature diagram of working fluid and air

The ACC modelling approach is based on partitioning the overall processes into a desuperheating and a condensation section. For each section, the average values of the thermophysical properties of the air and working fluid are used in all calculations. The energy balance equations in the desuperheating and condensation sections of the ACC, as well as in the overall heat exchanger are the following:

$$\dot{\boldsymbol{Q}}_{\boldsymbol{des}} = \dot{\boldsymbol{m}}_{\boldsymbol{wf}} \cdot \left(\boldsymbol{h}_{\boldsymbol{wf,in}} - \boldsymbol{h}_{\boldsymbol{wf,des,out}}\right) = \dot{\boldsymbol{m}}_{\boldsymbol{air}} \cdot \left(\boldsymbol{h}_{\boldsymbol{air,out}} - \boldsymbol{h}_{\boldsymbol{air,PP}}\right) \quad 2.1$$

$$\dot{\boldsymbol{Q}}_{\boldsymbol{cond}} = \dot{\boldsymbol{m}}_{\boldsymbol{wf}} \cdot \left(\boldsymbol{h}_{\boldsymbol{wf,ds,out}} - \boldsymbol{h}_{\boldsymbol{wf,out}}\right) = \dot{\boldsymbol{m}}_{\boldsymbol{air}} \cdot \left(\boldsymbol{h}_{\boldsymbol{air,PP}} - \boldsymbol{h}_{\boldsymbol{air,in}}\right) \quad 2.2$$

$$\dot{\boldsymbol{Q}}_{\boldsymbol{ACC}} = \dot{\boldsymbol{m}}_{\boldsymbol{wf}} \cdot \left(\boldsymbol{h}_{\boldsymbol{wf,out}} - \boldsymbol{h}_{\boldsymbol{wf,in}}\right) = \dot{\boldsymbol{m}}_{\boldsymbol{air}} \cdot \left(\boldsymbol{h}_{\boldsymbol{air,out}} - \boldsymbol{h}_{\boldsymbol{air,in}}\right) \quad 2.3$$

According to the developed ACC model, the inlet and outlet states and mass flow rates of the working fluid and air streams are known. By calculating the properties of the saturated vapor state of the refrigerant and solving Eq.1 or Eq.2, the thermophysical properties of the air at the pinch point (desuperheater outlet, condenser inlet) can be determined (air, PP).

2.1.2 ACC heat transfer area calculation based on geometry parameters

The ACC is modelled as a tube bank consisting of 60° staggered tubes, as shown in Figure 2.3. The working fluid is assumed to flow inside the tubes, while the cooling (ambient) air flows upwards through the space between them.

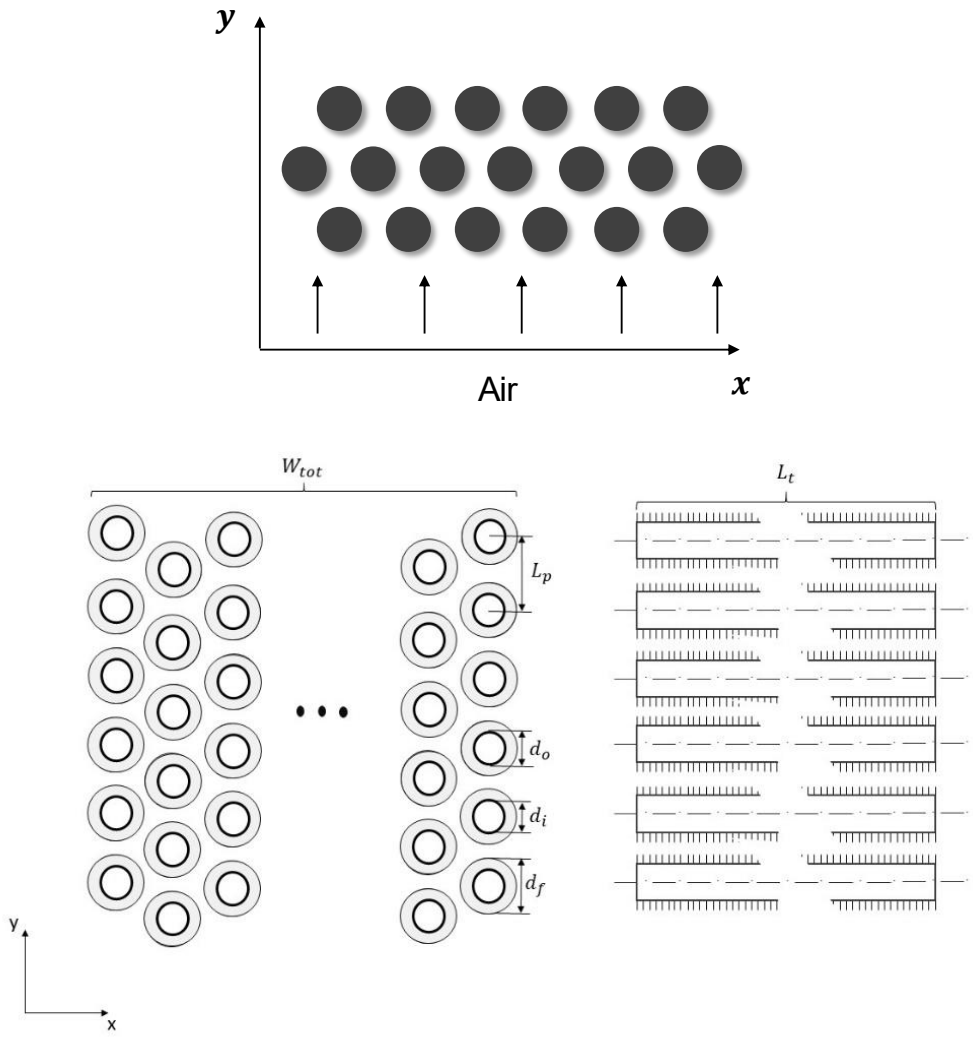

Figure 2.3. Staggered tube bank flow configuration

By definition, the total number of the tubes (N_t) is equal to the product of the number of tubes in the x direction (N_x) and tubes in the y direction (in the direction of the flow) (N_y):

$$\boldsymbol{N_t = N_x\, N_y} \quad 2.4$$

The tubes are characterized by their internal (d_i) and external diameters (d_o), while the distance between their centrelines is defined as the tube pitch (L_p). An additional key geometric parameter is the length of the tubes (L_t).

As shown in Figure 2.4, the projected distance between the centrelines of two successive tubes in the x direction is calculated from the following equation:

$$\boldsymbol{L_{p,x} = \sqrt{{L_p}^2 - \frac{{L_p}^2}{4}} = \sqrt{\frac{3{L_p}^2}{4}} = \frac{\sqrt{3}L_p}{2}} \quad 2.5$$

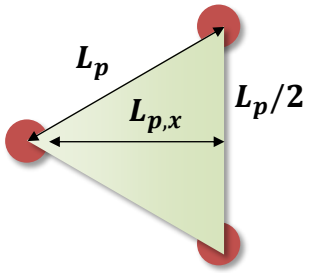

Figure 2.4. Projected distance between the centrelines of two successive tubes in x direction (60° staggered tubes)

Based on the number of tubes in the x direction, the total width of the ACC (W_{tot}) is calculated:

$$\boldsymbol{W_{tot} = (N_x - 1)L_{p,x} = (N_x - 1)\frac{\sqrt{3}L_p}{2} \approx N_x \frac{\sqrt{3}L_p}{2}} \quad 2.6$$

Therefore, the face area of the ACC, that is its projected area on the ground, is calculated from the following equation:

$$\boldsymbol{A_{face} = W_{tot}L_t = N_x \frac{\sqrt{3}L_p}{2} L_t = \frac{N_t}{N_y}\frac{\sqrt{3}L_p}{2} L_t} \quad 2.7$$

The total inner surface of all ACC tubes is calculated from the tube internal diameter, tube length, and number of tubes:

$$\boldsymbol{A_i = \pi \cdot d_i \cdot L_t \cdot N_t} \quad 2.8$$

The tubes of the ACC are finned. The fins are characterized by the fin spacing (i.e. the distance between two successive fins (L_f)), tube thickness (t_f), and fin diameter (d_f). The number of fins in each tube is calculated according to the illustration in Figure 2.5.

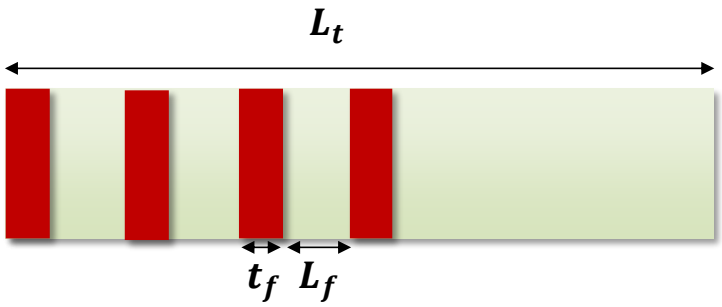

Figure 2.5. Number of fins

Ultimately, it is calculated by the following formulas:

$$L_t = (N_f - 1)L_f + N_f t_f = N_f L_f - L_f + N_f t_f \quad (2.9)$$

$$L_t = N_f(L_f + t_f) - L_f \quad (2.10)$$

$$N_f = \frac{L_t + L_f}{L_f + t_f} \quad (2.11)$$

The total outer surface of all ACC tubes (A_o) is calculated as the product of the outer surface of a single tube multiplied by the total number of tubes, according to the following equation:

$$A_o = N_t A_{o,tube} \quad (2.12)$$

The outer single tube area is calculated as the difference total tube area excluding the area covered by the base of the fins ($N_{fins}\pi d_o t_f$) plus the external area of all fins ($N_{fins}\ A_{fin}$):

$$A_{o,tube} = \pi d_o L_t - N_f \pi d_o t_f + N_f\ A_{fin} \quad (2.13)$$

The external area of each fin (A_{fin}) is the sum of the circular area of the fin ($\mathrm{A_{f,circle}}$) plus its peripheral area:

$$A_f = \mathrm{A_{f,circle}} + A_{f,periphery} \quad (2.14)$$

The circular area is defined according to the following formula:

$$A_{f,circle} = 2\pi \cdot \left(\frac{\mathrm{d_f^2}}{4} - \frac{\mathrm{d_o^2}}{4}\right) = \frac{\pi}{2}(\mathrm{d_f^2} - \mathrm{d_o^2}) \quad (2.15)$$

The peripheral fin area is defined according to the following formula:

$$A_{f,periphery} = \pi \cdot d_f \cdot t_f \quad (2.16)$$

Therefore, the total external area of the tubes is calculated according to the following formula:

$$A_o = N_t A_{o,tube} = N_t(d_o L_t - N_f \pi d_o t_f + N_f\ A_f) = N_t\left(d_o L_t - N_f(A_f - \pi d_o t_f)\right) \quad (2.17)$$

The total external tube area that is in direct contact with air is given by the following formula:

$$A_{o,air} = \pi d_o(L_t - t_f N_f)N_t \quad (2.18)$$

The relative inner and outer tube areas are calculated in equations 2.19-2.20.

$$A_{i,rel} = \frac{A_i}{A_o} \quad (2.19)$$

$$A_{o,rel} = \frac{A_{o,air}}{A_o} \quad (2.20)$$

2.1.3 Required heat transfer area calculation

In the previous section, the calculation of the internal and external heat transfer area of the ACC was presented based on a series of geometrical parameter inputs. In the present section, the calculation of the required heat transfer area of the ACC is described. It must be clarified that the heat transfer area is defined according to the external surface of the ACC, therefore:

$$A_{ACC} = A_o \quad (2.21)$$

Because of the largely different heat transfer conditions of the working fluid in the desuperheating and condensation regions, the calculation is carried out for each section separately.

The required heat transfer area in the desuperheating section ($A_{ACC,des}$) is calculated from the desuperheating heat duty ($\dot{Q}_{des}$), the logarithmic mean temperature difference for counter-current flow ($\Delta T_{lm,des}$), a flow correction factor ($F_{T,des}$) and the overall heat transfer coefficient (U_{des}) by the following equation:

$$A_{ACC,des} = \frac{\dot{Q}_{des}}{U_{des} F_{T,des} \Delta T_{lm,des}} \quad (2.22)$$

Accordingly, the required transfer area in the condensation section ($A_{ACC,cond}$) is calculated from the desuperheating heat duty ($\dot{Q}_{des}$), the logarithmic mean temperature difference for counter-current flow ($\Delta T_{lm,des}$), a flow correction factor ($F_{T,des}$) and the overall heat transfer coefficient (U_{des}) by the following equation:

$$A_{ACC,cond} = \frac{\dot{Q}_{cond}}{U_{cond} F_{T,cond} \Delta T_{lm,cond}} \quad (2.23)$$

Finally, the total required heat transfer area is calculated as the sum of the desuperheating and condensation required heat transfer areas:

$$A_{ACC} = A_{ACC,des} + A_{ACC,cond} \quad (2.24)$$

2.1.3.1 Desuperheating section

The desuperheating overall heat transfer coefficient expressed using the external tube heat transfer area (A_o) is calculated according to the following equation:

$$\boldsymbol{U_{des}^{-1}} = \frac{\mathbf{1}}{\boldsymbol{a_{wf,des}A_{i,rel}}} + \frac{\boldsymbol{A_o}}{\boldsymbol{N_t \pi L_t}} \frac{\boldsymbol{ln\left(\frac{d_o}{d_i}\right)}}{\mathbf{2}\boldsymbol{k_t}} + \frac{\mathbf{1}}{\boldsymbol{a_{air}\eta_{fw}}} \quad 2.25$$

Where $k_t = 16\ W/mK$ is the thermal conductivity of the tube material (stainless steel, [43]).

For the evaluation of all thermophysical properties of the air and working fluid that are used in subsequent equations, their mean temperatures in the desuperheating are considered:

$$\boldsymbol{T_{air,mean,des}} = \frac{\boldsymbol{T_{air,out} + T_{air,pp}}}{\mathbf{2}} \quad 2.26$$

$$\boldsymbol{T_{wf,mean,des}} = \frac{\boldsymbol{T_{wf,in} + T_{wf,g}}}{\mathbf{2}} \quad 2.27$$

The heat transfer coefficient of air (a_{air}) is calculated from the following equation based on the Nusselt number (Nu_{air}), external tube diameter (d_o) and thermal conductivity ($\overline{k_{air}}$).

$$\boldsymbol{a_{air}} = \boldsymbol{Nu_{air}} \cdot \frac{\boldsymbol{\overline{k_{air}}}}{\boldsymbol{d_o}} \quad 2.28$$

The Nusselt number (Nu_{air}) is calculated from the Reynolds (Re_{air}) and Prandtl (Pr_{air}) numbers as well as the relative external heat transfer area ($A_{o,rel}$) according to the following formula [44]:

$$\boldsymbol{Nu_{air}} = \mathbf{0.38}\boldsymbol{Re_{air}^{0.6} Pr_{air}^{1/3} A_{o,rel}^{0.15}} \quad 2.29$$

The Reynolds number is calculated according to the following equation:

$$\boldsymbol{Re_{air}} = \boldsymbol{d_o u_{air,max}} \frac{\boldsymbol{\bar{\rho}_{air}}}{\boldsymbol{\bar{v}_{air}}} \quad 2.30$$

Where $\bar{\rho}_{air}$ is the air density and $\bar{v}_{air}$ is the air kinematic viscosity evaluated at and $u_{air,max}$ is the maximum velocity of the air as it flows between the tubes of a staggered bank consisting of finned tubes:

$$\boldsymbol{u_{air,max}} = \boldsymbol{u_{air,face} L_p} \frac{\boldsymbol{L_f + t_f}}{\boldsymbol{L_p(L_f + t_f) - d_o L_f - d_f t_f}} \quad 2.31$$

In the previous equation, $u_{air,face}$ is the face velocity of the air that is calculated based on its mass flow rate, density, and ACC face area:

$$\boldsymbol{u_{air,face}} = \frac{\boldsymbol{\dot{m}_{air}}}{\boldsymbol{A_{face}\bar{\rho}_{air}}} \quad 2.32$$

The heat transfer coefficient of organic fluid in the desuperheating section ($a_{wf,des}$) is calculated from [45], according to the following equation:

$$\boldsymbol{a_{wf,des}} = \boldsymbol{Nu_{wf,des}} \frac{\boldsymbol{\overline{k_{wf,des}}}}{\boldsymbol{d_i}} \quad 2.33$$

The Gnielinski correlation [46] is used for the calculation of the Nusselt number inside the tubes based on the Reynolds ($Re_{wf,des}$), Prandtl ($Pr_{wf,des}$) numbers and the Darcy friction factor (F_D).

$$\boldsymbol{Nu_{wf,des} = \frac{\frac{F_D}{8}\left(Re_{wf,des} - 1000\right)Pr_{wf,des}}{1 + 12.7\sqrt{\frac{F_D}{8}}\left(\overline{Pr_{wf,des}^{2/3}} - 1\right)}} \quad 2.34$$

The Reynolds number for tubular flow is calculated according to the following equation:

$$\boldsymbol{Re_{wf,des} = \frac{4m_{wf,tube}}{\pi d_i \overline{v_{wf,des}}}} \quad 2.35$$

For its calculation, the mass flow rate of the working fluid in each tube ($m_{wf,tube}$) must be calculated. This mass flow rate depends on the total number of tubes and rows per pass (N_{rp}). This is illustrated graphically for two cases in Figure 2.6.

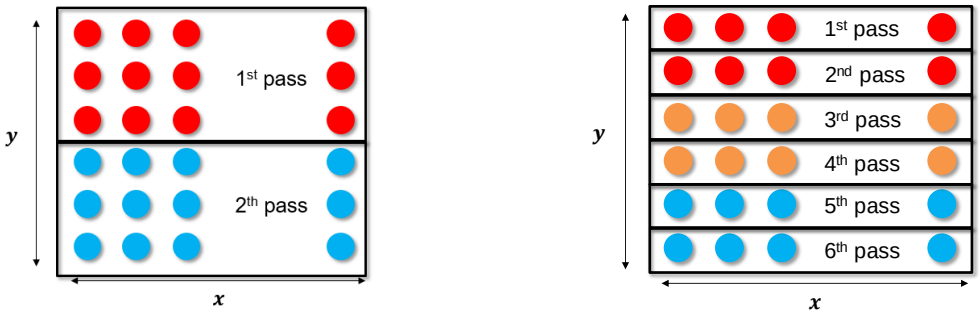

Figure 2.6. Example arrangements of 6 rows and 2 passes (left) and 6 passes (right)

As the working fluid enters the ACC, it is split into a number of tubes that is equal to the product of the number of tubes in the x direction and the number of rows per pass:

$$\boldsymbol{\dot{m}_{wf,tot} = \dot{m}_{tube} N_x N_{rp} = \dot{m}_{tube} \frac{N_t}{N_y} N_{rp}} \quad 2.36$$

However, by definition, the number of rows per pass is equal to the total number of rows (N_y) divided by the number of passes (N_{tp}):

$$\boldsymbol{N_y = N_{rp} N_{tp}} \quad 2.37$$

Therefore, combining the previous two equations, the tube mass flow rate is calculated according to the following equation:

$$\boldsymbol{\dot{m}_{tube} = \dot{m}_{tot} \frac{N_{tp}}{N_t}} \quad 2.38$$

Therefore, the Reynolds number is calculated from the following formula:

$$\boldsymbol{Re_{wf,des} = \frac{4\dot{m}_{wf,tot} N_{tp}}{\pi d_i N_t \overline{v_{wf,des}}}} \quad 2.39$$

The Darcy friction factor is calculated according to the following equation:

$$\boldsymbol{F_D = \left(0.782 \cdot ln\left(Re_{wf,des}\right) - 1.51\right)^{-2}} \quad 2.40$$

To account for the presence of fins in the calculation of the overall heat transfer coefficient, the fin efficiency (η_f) and weighted fin efficiency (η_{wf}) are introduced and calculated according to [43].

The eqs. 2.41-2.44 result from the solution of a 2nd degree differential equation that emerged from an energy balance in the fin. Then a simplified equation of η_f was introduced by [47].

energy balance in the fins,$k_f = 237\ W/m\ K$ is the thermal conductivity of the aluminum fins.

$$\boldsymbol{\eta_f = \frac{q_{fin}}{q_{max}} \cong \frac{tanh(\varphi \cdot \omega)}{\varphi \cdot \omega}} \quad 2.41$$

$$\boldsymbol{\varphi = \sqrt{\frac{2a_{air}}{k_f \cdot t_f}}} \quad 2.42$$

$$\boldsymbol{\omega = \frac{d_f + t_f - d_o}{2}\left(1 + 0.35 ln\left(\frac{d_f + t_f}{d_o}\right)\right)} \quad 2.43$$

$$\boldsymbol{\eta_{fw} = \frac{A_{o,air} + \eta_f A_f}{A_{ACC}}} \quad 2.44$$

Eventually combining all the factors and variables needed the overall heat transfer coefficient ($U_{wf,des}$) in the desuperheating section is calculated [43].

The logarithmic mean temperature difference of the streams in the desuperheating is calculated according to the following equation:

$$\boldsymbol{\Delta T_{lm,des} = \frac{(T_{wf,in} - T_{air,out}) - (T_{wf,sat} - T_{air,pp})}{ln\left(\frac{T_{wf,in} - T_{air,out}}{T_{wf,g} - T_{air,pp}}\right)}} \quad 2.45$$

Because the ACC is a cross-flow and not a counter-current heat exchanger, a correction factor is introduced to correct the value of $\Delta T_{lm,des}$. Because in the desuperheating the temperature of both the air and the working fluid inside the tubes changes during heat transfer a correction factor is introduced to calculate the overall heat transfer coefficient, which is defined according to the following equation introducing a surrogate model according to [48].:

$$\begin{aligned} \boldsymbol{F_{T,des}^{-1}} = {} & \boldsymbol{0.60127 - 1.9843 tanh(3.1595 - 2.3103 e_h - 1.6979 e_c) + 1.9843} \\ & \boldsymbol{\cdot tanh(3.8096 + 2.0196 e_h - 2.3837 e_c) - 0.22447} \\ & \boldsymbol{\cdot tanh(9.6024 - 6.5102 e_h - 9.3455 e_c) + 0.61916} \\ & \boldsymbol{\cdot tanh(2.8588 - 2.7623 e_h - 1.2156 e_c)} \end{aligned} \quad 2.46$$

In this equation, e_h and e_c is the effectiveness of the hot and cold streams:

$$e_h = \frac{T_{wf,in} - T_{wf,g}}{T_{wf,in} - T_{air,pp}} \quad (2.47)$$

$$e_c = \frac{T_{air,out} - T_{air,pp}}{T_{wf,in} - T_{air,pp}} \quad (2.48)$$

2.1.3.2 Condensation section

Likewise, the overall heat transfer coefficient in the condensation section considering the outer heat transfer area of the ACC is:

$$U_{cond}^{-1} = \frac{1}{a_{wf,cond} A_{i,rel}} + \frac{\frac{A_{ACC}}{N_t}}{\pi L_t} \frac{ln\left(\frac{d_o}{d_i}\right)}{2k_t} + \frac{1}{a_{air}\eta_{fw}} \quad (2.49)$$

The heat transfer coefficient of air in the condensation section is calculated in the same manner presented in the desuperheating section. However, all thermophysical properties of air are evaluated at the mean temperature corresponding to the condensation section:

$$T_{air,mean,cond} = \frac{T_{air,in} + T_{air,pp}}{2} \quad (2.50)$$

The heat transfer coefficient of the working fluid in the tubes within the condensation section ($\alpha_{wf,cond}$) is calculated starting from the local heat transfer coefficient the following equation proposed by Shah [49]:

$$\alpha_{wf,cond} = 0.023 Re_{wf,g}^{0.8} Pr_{wf,g}^{0.4} \frac{k_{wf,g}}{d_i} F_x \quad (2.51)$$

In the above equation, the quantities with subscript "g" are calculated for the saturated vapor state of the working fluid [49, 50].

The Reynolds number is calculated according to the following equation, considering the mass flow rate of the working fluid in each tube, as it was described in the previous section:

$$R_{wf,g} = \frac{4 m_{wf} N_{tp}}{\pi d_i N_t v_{wf,g}} \quad (2.52)$$

The general expression of F_x is given by the following formula:

$$F_x = (1 - x)^{0.8} + \frac{3.8 x^{0.76} (1 - x)^{0.04}}{p_{wf,red}} \quad (2.53)$$

In the above equation, x is the quality of the working fluid, while p_{red} is its reduced pressure, defined as the ratio of its pressure divided by the critical pressure.

$$p_{red} = \frac{p}{p_{crit}} \quad (2.54)$$

Because the quality of the working fluid changes during the condensation process from 1 to 0, its heat transfer coefficient also changes. However, as proposed by Shah, a linear variation is assumed and the integral of the F_x is calculated and used in the heat transfer coefficient calculation:

$$\overline{F_x} = \int_0^1 F_x dx = \frac{5}{9} + \frac{2.0434}{p_{wf,red}^{0.38}} \quad 2.55$$

Therefore, the heat transfer coefficient of the working fluid is ultimately calculated according to the following equation:

$$\bar{a}_{wf,cond} = 0.023 Re_{wf,g}^{0.8} \cdot \overline{Pr}_{wf,g}^{0.4} \frac{\bar{k}_{wf,g}}{d_i} \cdot \overline{F_x} \quad 2.56$$

The logarithmic mean temperature difference of the streams in the condenser is calculated according to the following equation:

$$\Delta T_{lm,cond} = \frac{(T_{wf,g} - T_{air,pp}) - (T_{wf,g} - T_{air,in})}{lm\left(\frac{T_{wf,g} - T_{air,pp}}{T_{wf,g} - T_{air,in}}\right)} \quad 2.57$$

Because the temperature of the working fluid in the condensation section is constant, the correction factor for this section is equal to unity ($F_{T,cond} = 1$).

2.1.4 Air-side pressure drop calculation

The air pressure drop in the ACC is very important since it greatly affects the ACC fan motor power consumption. It is calculated through the equation 2.63 according to [51, 52]. The variables a, b, and h are used in the calculation of. According to the Reynolds number, the appropriate equation is used, and then the air pressure drop as well as the complete air pressure drop is calculated.

The pressure drop of the air as it passes through the ACC is calculated according to the following equation: [53]

$$\Delta P_{air} = \xi N_y \bar{\rho}_{air} \frac{u_{air,max}^2}{2} \quad 2.58$$

In the above equation, the density of the air is calculated at its mean temperature throughout the whole ACC:

$$T_{air,mean,ACC} = \frac{T_{air,in} + T_{air,our}}{2} \quad 2.59$$

ξ is the Drag coefficient of air, which according to the Reynolds Number is calculated in one of the equations below:

$$\xi = 290 \cdot Re_{air}^{-0.7} \cdot j^{-0.55} \cdot z^{-0.5} \cdot \left(1 - \frac{t_f}{d_o}\right)^{1.8} \cdot \left(1 - \frac{s}{d_o}\right)^{-1.4}, \; 10^2 < Re_{air} < 10^3 \quad 2.60$$

$$\xi = 13 \cdot Re_{air}^{-0.25} \cdot j^{-0.55} \cdot z^{-0.5} \cdot \left(1 - \frac{t_f}{d_o}\right)^{1.8} \cdot \left(1 - \frac{s}{d_o}\right)^{-1.4}, 10^3 < Re_{air} < 10^5 \quad (2.61)$$

$$\xi = 0.74 \cdot m^{-0.55} \cdot j^{-0.5} \cdot \left(1 - \frac{t_f}{d_o}\right)^{1.8} \cdot \left(1 - \frac{s}{d_o}\right)^{-1.4}, 10^5 < Re_{air} < 10^6 \quad (2.62)$$

j, z, and s parameters are calculated according to the following equations:

$$j = L_p / d_o \quad (2.63)$$

$$z = \frac{\sqrt{5}}{2} \cdot \frac{L_p}{d_o} \quad (2.64)$$

$$s = \frac{d_f - d_o}{2} \quad (2.65)$$

The fans should provide a sufficient pressure increase to sustain the flow of air in the ACC. Therefore, the pressure rise of the fans is calculated considering a 20% additional pressure compared to the ACC pressure drop:

$$\Delta P_{air,fan} = 1.2 \Delta P_{air} \quad (2.66)$$

The fan motor power consumption is calculated according to the following equation:

$$P_{e,fan} = \Delta P_{air,fan} \frac{\dot{V}_{air}}{\eta_{fan}} \quad (2.67)$$

In the above equation, $\dot{V}_{air}$ is the volume flow rate of the air, while η_{fan} is the fan motor efficiency. The air volume flow rate is calculated according to the following equation:

$$\dot{V}_{air} = \frac{\dot{m}_{air}}{\bar{\rho}_{air}} \quad (2.68)$$

2.1.5 Cost of ACC

The cost of the ACC is calculated through the equations 2.69-2.71 using the method from Astolfi [54]. $C_{ACC,bare}$ is the base equipment cost for a component operating at ambient pressure and made from carbon steel. Effects on the pressure and labor are taken into account by multiplying with the factory in eq. 2.70. The cost of the ACC is updated using the chemical engineering plant cost index (CEPCI) of 2023.

$$C_{ACC,bare} = 10^{K_1 + K_2 \cdot log(A_{ACC}) + K_3 \cdot (log(A_{ACC}))^2} \quad (2.69)$$

$$C_{ACC,2000} = C_{ACC,bare} \cdot (B1 + B2 \cdot FM) \quad (2.70)$$

$$C_{ACC,2023} = C_{ACC,2000} \cdot \frac{CEPCI_{2023}}{CEPCI_{2000}} \quad (2.71)$$

The table above displays the coefficients used in the equations.

Table 2.1: Coefficients for ACC cost correlation	
$K_1 = 4.0336$	$B_1 = 0.96$
$K_2 = 0.2341$	$B_2 = 1.21$
$K_3 = 0.0497$	$F_M = 1.8\ \ (AL)$

In Figure 2.7 the ACC cost correlation vs the ACC heat transfer area is presented.

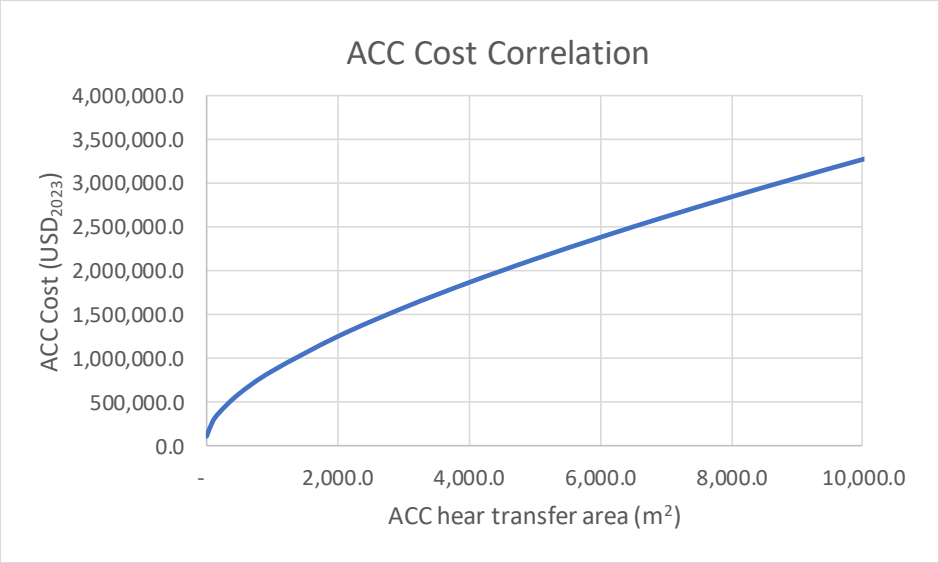

Figure 2.7: ACC Cost correlation vs ACC heat transfer area

As it can be concluded from the diagram, the ACC costs are extremely high considering the investment costs of ORC units in the literature. One reason is that costs have been adapted to 2023 values using the CEPCI index, under which an increase of 50% is considered compared to prices before 2019. Also, it needs to be noted that the ACC cost correlation has a valid range equal to $10 - 10000m^2$. In the parametric analysis, higher ACC areas will be examined and the respective costs will be listed indicatively.

2.1.6 ACC sizing model in Matlab

In Figure 2.8 a flowchart of the ACC sizing model is depicted. As mentioned previously the model was developed in Matlab, applying the methodology of sections 2.1.1-2.1.5. The code starts with the setting of thermodynamic inputs for air (p_{air}, $T_{air_{in}}$, ΔT_{air}) and organic fluid ($\dot{m}_{wf}, T_{wf,in}, \Delta T_{wf,ds}$), as well as ACC geometry inputs ($d_i, d_o, d_f, L_f, t_f, L_t, L_p, N_y, N_{tp}$). Right after all the necessary thermophysical property calculations are made $(p, h, T, \rho, Pr, k, v)$ for air and organic fluid using Refprop. More specifically the thermophysical properties of both air and organic fluid are calculated in the inlet, pinch point, and outlet of the condensation, including also calculation

of mean values for condensation and desuperheating section respectively. An energy balance in the ACC is made according to eqs. 2.1-**Error! Reference source not found.** resulting in the estimation of $mair$, and eventually $Tair,pp$.

The repeated procedure starts with an initial guess about the ACC heat transfer area (A_{ACC}). According to the A_{ACC} value, the code calculates the total number of tubes (N_t) from the eq. 2.17 of the definition of the total external area of the tubes (A_o), where $A_o = A_{ACC}$ according to eq. 2.21. The rest of the geometry-related calculations follow including the calculation of A_{face} (eq. 2.7), $A_{o,rel}$ (eq. 2.20), $A_{i,rel}$ (eq. 2.19), and A_f (eq. 2.14).

A set of calculations follow in order to estimate the overall heat transfer coefficient in the condensation ($U_{cond}, eq. 2.49$) and desuperheating section ($U_{des}, eq.\ 2.25$) respectively. At first, the heat transfer coefficient of air (a_{air}, eqs. 2.28-2.32) is calculated. For the condensation section, the heat transfer coefficient of working fluid ($a_{wf,cond}$, eq. 2.56) is calculated. For the desuperheating section except from the heat transfer coefficient of working fluid ($a_{wf,des}$, eq. 2.33-2.35), the correction factor ($F_{T,des}$, eq. 2.46) and the weighted fin efficiency (η_{wf}, eq.2.44) needs also to be calculated. The detailed methodology of the correlations for both desuperheating (2.1.3.1) and condensation (2.1.3.2) is explained in the previous respective sections.

The mean logarithmic temperature difference for desuperheating ($\Delta T_{lm,des}$, eq. 2.45) and condensation ($\Delta T_{lm,cond}, eq.\ 2.57$) section is then calculated. The new ACC heat transfer area ($A_{ACC,new}$) is calculated as the sum of the desuperheating ($A_{ACC,des}$) and condensation $A_{ACC,cond}$ required heat transfer areas through equations 2.22-2.23. The codes check if the subtraction of new and previous A_{ACC} is smaller than 0.01. If it isn't, the repeated procedure starts from the beginning having as A_{ACC} =$A_{ACC,new}$.

When the repeated procedure is over, the air pressure drop (ΔP_{air}, eqs. 2.63-2.62), the ACC power fan consumption ($P_{e,ACC,fan}$, eq.2.67) and ACC cost (C_{ACC}, eqs. 2.69-2.71) are calculated and the code ends.

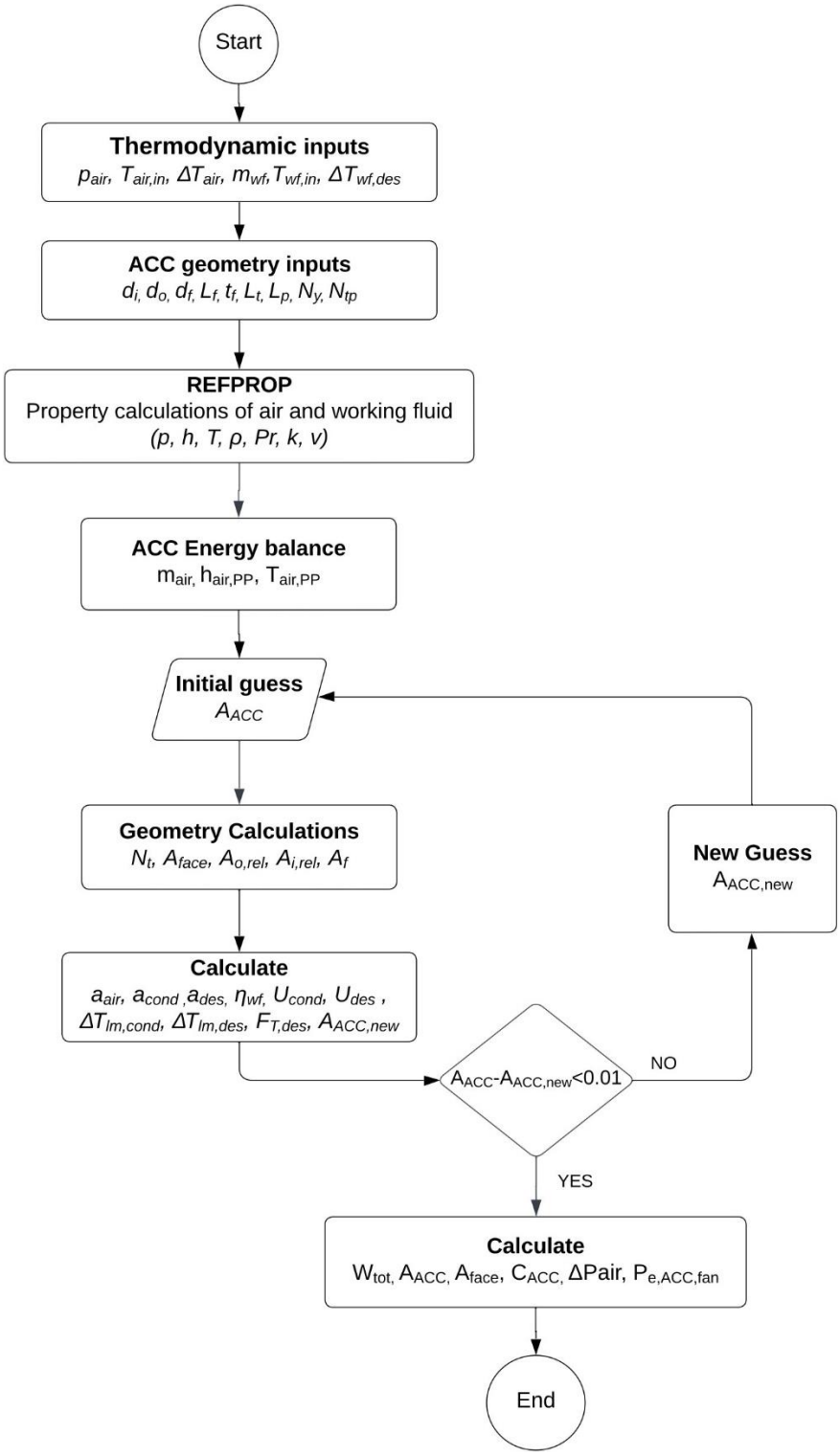

Figure 2.8: Flow chart of ACC modelling in Matlab

2.2 ORC design modelling

The ACC sizing model is integrated into an ORC design model. The ORC model is based on a standard, recuperative ORC configuration, as the one illustrated in Figure 1.3. The inputs of the model and additional modelling assumptions summarized in Table 2.2. The thermodynamic design is based on a large-scale industrial waste heat recovery (*WHR*) ORC that was developed in the context of the Decagone project [55].

Table 2.2 ORC model inputs

ORC model input parameters	**Values**
Expander isentropic efficiency	65%
Pump isentropic efficiency	65%
Electromechanical efficiency of expander-generator	96%
Pump motor efficiency	85%
Heat source fluid	Therminol T-66
Heat source temperature at ORC evaporator inlet	310℃
Heat source temperature at ORC evaporator outlet	130℃
Heat source mass flow rate	9.74 kg/s
Working fluid	Cyclopentane
Working fluid temperature at ORC evaporator outlet	240℃
Working fluid superheating at ORC evaporator outlet	31.76 K
Pinch point in recuperator	30.98 K
Pinch point in air-cooled condenser	investigated
Ambient air temperature	15℃
Ambient air temperature rise in air-cooled condenser	investigated

The output variables of the model are summarized in Table 2.3

Table 2.3 ORC model outputs

Working fluid condensation temperature (℃)
Working fluid condensation pressure (bar)
Working fluid mass flow rate (kg/s)
Air-cooled condenser air mass flow rate (kg/s)
Working fluid temperatures at the inlet and outlet of the recuperator cold and hot sides (℃)
Heat duties of all heat exchangers (kW_{th})

Expander hydraulic power (kW)
Expander generator electric power output (kW_e)
Pump hydraulic power (kW)
Pump motor electric power consumption (kW_e)
Air-cooled condenser fan motor electric power consumption (kW_e)
ORC net power output (kW_e)
ORC electric efficiency (%)

The modeling of the cycle is based on the energy balance equations of all components (heat exchangers, pumps, and turbines).

$$\dot{\boldsymbol{Q}}_{\boldsymbol{evap}} = \dot{\boldsymbol{m}}_{\boldsymbol{wf}}\left(\boldsymbol{h}_{\boldsymbol{wf,exp,in}} - \boldsymbol{h}_{\boldsymbol{wf,evap,in}}\right) = \dot{\boldsymbol{m}}_{\boldsymbol{oil}}\left(\boldsymbol{h}_{\boldsymbol{oil,in}} - \boldsymbol{h}_{\boldsymbol{oil,out}}\right) \quad 2.72$$

$$\dot{\boldsymbol{Q}}_{\boldsymbol{ACC}} = \dot{\boldsymbol{m}}_{\boldsymbol{wf}}\left(\boldsymbol{h}_{\boldsymbol{wf,cond,in}} - \boldsymbol{h}_{\boldsymbol{wf,cond,out}}\right) = \dot{\boldsymbol{m}}_{\boldsymbol{air}}\left(\boldsymbol{h}_{\boldsymbol{air,out}} - \boldsymbol{h}_{\boldsymbol{air,in}}\right) \quad 2.73$$

$$\dot{\boldsymbol{Q}}_{\boldsymbol{rec}} = \dot{\boldsymbol{m}}_{\boldsymbol{wf}}\left(\boldsymbol{h}_{\boldsymbol{wf,pump,out}} - \boldsymbol{h}_{\boldsymbol{wf,evap,in}}\right) = \dot{\boldsymbol{m}}_{\boldsymbol{wf}}\left(\boldsymbol{h}_{\boldsymbol{wf,turb,out}} - \boldsymbol{h}_{\boldsymbol{cond,in}}\right) \quad 2.74$$

$$\boldsymbol{P}_{\boldsymbol{wf,pump}} = \dot{\boldsymbol{m}}_{\boldsymbol{wf}}\left(\boldsymbol{h}_{\boldsymbol{wf,pump,out}} - \boldsymbol{h}_{\boldsymbol{wf,cond,out}}\right) \quad 2.75$$

$$\boldsymbol{P}_{\boldsymbol{wf,turb}} = \dot{\boldsymbol{m}}_{\boldsymbol{wf}}\left(\boldsymbol{h}_{\boldsymbol{wf,turb,in}} - \boldsymbol{h}_{\boldsymbol{wf,turb,out}}\right) \quad 2.76$$

Furthermore, the isentropic efficiency of the pump and expander is used for calculating the outlet state of the refrigerant at each component according to the following equations:

$$\boldsymbol{\eta}_{\boldsymbol{pump,is}} = \frac{\left(\boldsymbol{h}_{\boldsymbol{wf,pump,out,is}} - \boldsymbol{h}_{\boldsymbol{wf,pump,in}}\right)}{\left(\boldsymbol{h}_{\boldsymbol{wf,pump,out}} - \boldsymbol{h}_{\boldsymbol{wf,pump,in}}\right)} \quad 2.77$$

$$\boldsymbol{\eta}_{\boldsymbol{turb,is}} = \frac{\left(\boldsymbol{h}_{\boldsymbol{wf,turb,in}} - \boldsymbol{h}_{\boldsymbol{wf,turb,out}}\right)}{\left(\boldsymbol{h}_{\boldsymbol{wf,turb,in}} - \boldsymbol{h}_{\boldsymbol{wf,turb,out,is}}\right)} \quad 2.78$$

The net power production of the plant is:

$$\boldsymbol{P}_{\boldsymbol{e,net}} = \boldsymbol{P}_{\boldsymbol{e,turb}} - \boldsymbol{P}_{\boldsymbol{e,pump}} - \boldsymbol{P}_{\boldsymbol{e,ACC,fan}} \quad 2.79$$

The electrical efficiency is defined as:

$$\boldsymbol{\eta}_{\boldsymbol{e}} = \frac{\boldsymbol{P}_{\boldsymbol{e,net}}}{\dot{\boldsymbol{Q}}_{\boldsymbol{evap}}} \quad 2.80$$

2.3 ORC-ACC modeling

As mentioned previously, the ACC sizing model is integrated with the ORC design model. The interaction between the two models is shown in Figure.

The overall parametric investigation is carried out for 4 variables; 2 ORC design variables (the condenser pinch point and air temperature rise in the ACC) and 2 ACC geometric variables (the number of tube passes and total length of the ACC). Regarding the ACC geometry, one constraint is considered. In particular, it is assumed that the aspect ratio of the ACC (i.e. the ratio of the tube length divided by the ACC width) should range from 1 to 7. This practically means that designs in which the width of the ACC is higher than the length or designs in which the length of the ACC is far too high than the width are rejected. An additional practical constraint concerns the net power output of the ORC. In particular, designs for which the ACC fan motor power consumption is higher than 50% of the gross power output of the ORC expander minus the power consumption of the ORC pump (i.e. extreme cases in which the ORC is not capable of producing any electricity) are rejected, as they are practically infeasible.

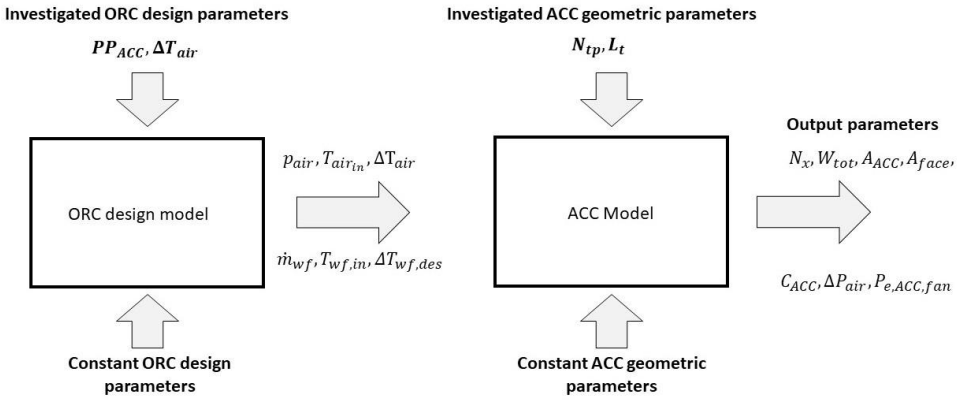

Figure 2.9. Interaction between ORC design model and ACC sizing models

The investigated parameters and their ranges are shown in Table 2.4.

Table 2.4 ORC-ACC investigated parameters and their ranges

Parameter	**Range**
ACC pinch point	2-30 K
Air temperature rise in ACC	5-30 K
Number of tube passes	2, 6
ACC tube length	10, 15, 20 m
Constraint	1<aspect ratio<7, $P_{e,ACC,fan} < 0.5(P_{e,turb} - P_{e,pump})$

With the exception of the tube length and the number of tube passes, all other input geometric parameters of the ACC are considered constant. Their values are summarized in Table 2.5. Each

variable along with its value is explained. The assumed tube and fin geometry for the ACC is taken from [43, 56].

Table 2.5 Fixed ACC geometry parameters	
Number of tubes in x dimensions (N_x)	6
Tube pitch (L_p)	69.85 mm
Fin spacing (L_f)	2.3 mm
Outer tube (d_o)	31.75 mm
Inner tube (d_i)	28.25 mm
Fin (d_f)	63.5 mm
Fin thickness (t_f)	0.3 mm

For each set of investigated parameters of Table 2.4, the net power output of the ORC (also considering the ACC fan motor power consumption), the heat transfer area of the ACC, and its cost are calculated, among other parameters. A parameter that can be used for providing a combined thermodynamic and economic evaluation of the system is the specific ACC cost, which is defined as the ratio of the ACC cost divided by the net power output, according to the following equation:

$$\boldsymbol{C_{sp,ACC} = \frac{C_{ACC,2023}}{P_{e,net}}} \quad 2.81$$

If the specific ACC cost is very high, the cost of the ACC is disproportionately high compared to the net power output and thus the system is not very cost-effective. On the other hand, if the ACC cost is very low, the cost of the ACC is very small compared to the net power output, thus the system is more cost-effective. Of course, the specific ACC cost is not in itself fully capable of evaluating the techno-economic performance of the system but is useful as a preliminary indicator.

3. Results

In this chapter, the results of the parametric investigation are presented. The overall parametric investigation is carried out for 4 variables; 2 ORC design variables (the condenser pinch point and air temperature rise in the ACC) and 2 ACC geometric variables (the number of tube passes and length of the ACC tubes). To conclude successive and combined results from the parametric investigation, the parameters below are investigated:

1. ACC heat transfer area (A_{ACC})
2. ACC face area (A_{face})
3. ACC fan power consumption ($P_{e,ACC,fan}$)
4. ACC air side pressure drop (ΔP_{air})
5. ORC net power output ($P_{e,ORC,net}$)
6. ORC electrical efficiency ($\eta_{e,net}$)
7. ACC cost (C_{ACC})
8. ACC specific cost ($C_{ACC,sp}$)

For each parameter, a diagram is displayed vs the pinch point (PP_{ACC}) range. Each curve corresponds to a different air temperature rise (ΔT_{air}) in the ACC. For each parameter, 2 diagrams are presented corresponding to 2 and 6-tube pass (N_{tp}) configurations. In total, three sets of results are presented for 10, 15, and 20 m total tube length)

3.1 Parametric analysis of ACC pinch point and air temperature rise 2, 6 tube passes and 10 m total ACC tube length

In Figure 3.1 the A_{ACC} vs PP_{ACC} is depicted for 2 and 6 tube passes for a tube length of 10 m. Each curve corresponds to a different ΔT_{air}. It is observed that each curve has a different feasible PP_{ACC} range. This happens because of the rejection of results according to the constraints (related to acceptable ACC aspect ratios and fan power consumption values) that were described in the previous section. It can be concluded that for higher ΔT_{air} values, the accepted PP_{ACC} is expanded.

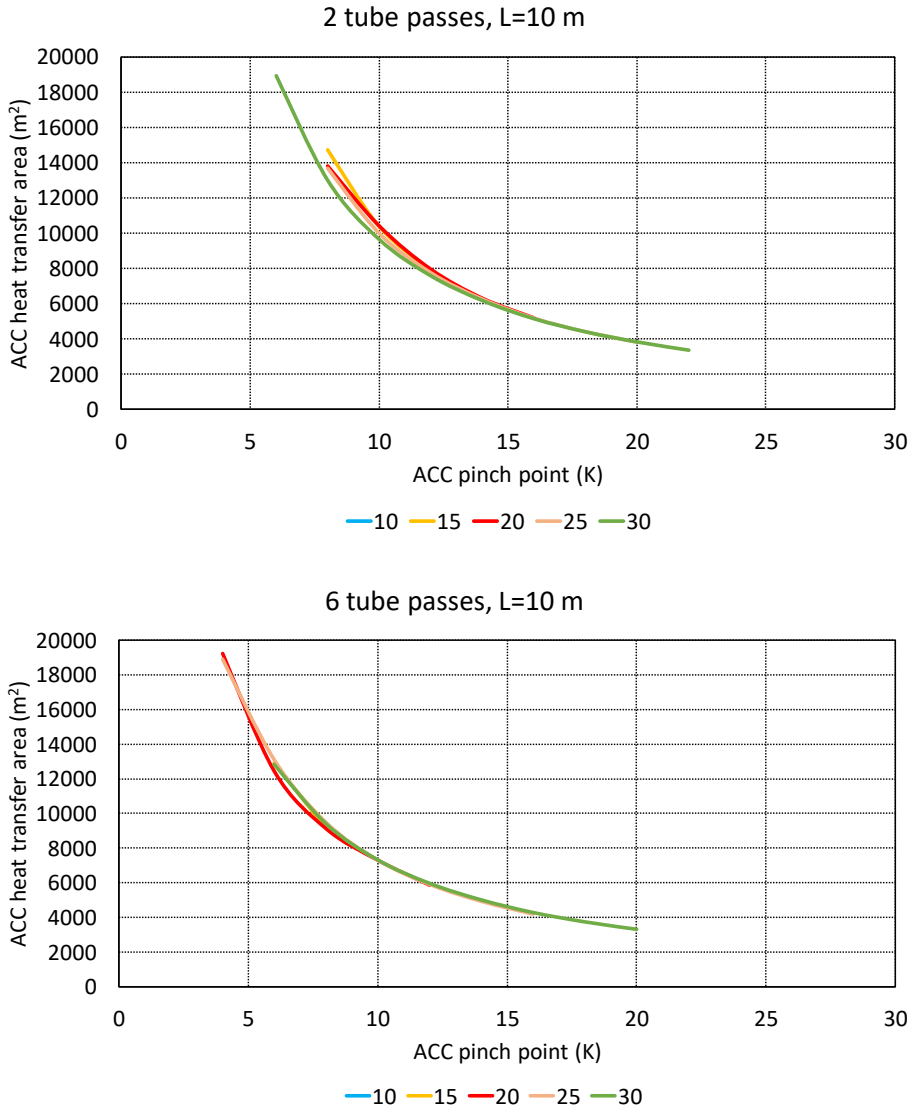

Figure 3.1: ACC heat transfer area vs ACC pinch point for 2 & 6 tube pass configuration and 10m total tube length. Each curve corresponds to a different air temperature rise.

For a fixed ΔT_{air}, as PP_{ACC} increases, the condensation temperature/pressure of the ORC increases. As a result, the thermal efficiency of the cycle decreases, which increases $\dot{Q}_{cond}$, as more heat is rejected because of the decreasing thermal efficiency. Meanwhile, as the PP_{cond} increases, the temperature difference between the air and working fluid increases, resulting in an increasing ΔT_{lm} in the ACC. Ultimately, considering eq. 2.23, the effect of increasing ΔT_{lm} is more significant than the impact of increasing $\dot{Q}_{ACC}$, and thus the area of the ACC is decreased. Notably, for PP_{ACC} values below 10 K, the area of the ACC increases dramatically by almost 100% for a further decrease of the pinch point value by 5 K.

It can also be observed that the influence of ΔT_{air} in the ACC area is insignificant, since, for the same PP_{ACC}, the ACC area is almost the same for different values of ΔT_{air}. Essentially, when, for a fixed pinch point value, the ΔT_{air} increases, the condensation temperature/pressure of the cycle increases, resulting in a decrease in the thermal efficiency and hence an increase in $\dot{Q}_{ACC}$. However, it should be noted that the variation of $\dot{Q}_{ACC}$ for different ΔT_{air} values in the ACC is very small. At the same time, the variation of ΔT_{lm} for variable ΔT_{air} values is also very small. Therefore, also considering eq. 2.23, the overall impact of ΔT_{air} in the ACC area.

Furthermore, comparing the 2 diagrams for 2 and 6 tube passes it can be concluded that for the same PP_{ACC}, the 6 tube passes configuration requires a smaller ACC heat transfer area. This phenomenon is observed because, in the 2-pass configuration, the working fluid stream is divided into 3 different streams. This results in smaller Reynolds numbers and therefore in smaller Nusselt numbers that lead to reduced heat transfer coefficients, as made clear from equations 2.33-2.35, resulting in increased required heat transfer surfaces.

In Figure 3.2 A_{face} vs PP_{ACC}, is displayed. A_{face} is closely related to the A_{ACC} as shown by equations 2.6-2.17 where the geometry of the ACC is explained. In particular, for a given tube length and pitch, as the face area increases, the number of tubes in the x direction (N_x) increases. Therefore, the same conclusions with the ACC heat transfer area can be made for the ACC face area. While the ACC heat transfer area is directly related to the cost of the ACC, the face area of the ACC is more relevant to practical considerations. Depending on the spatial availability on the site of the ORC installation, there is a limit on the maximum ACC face area.

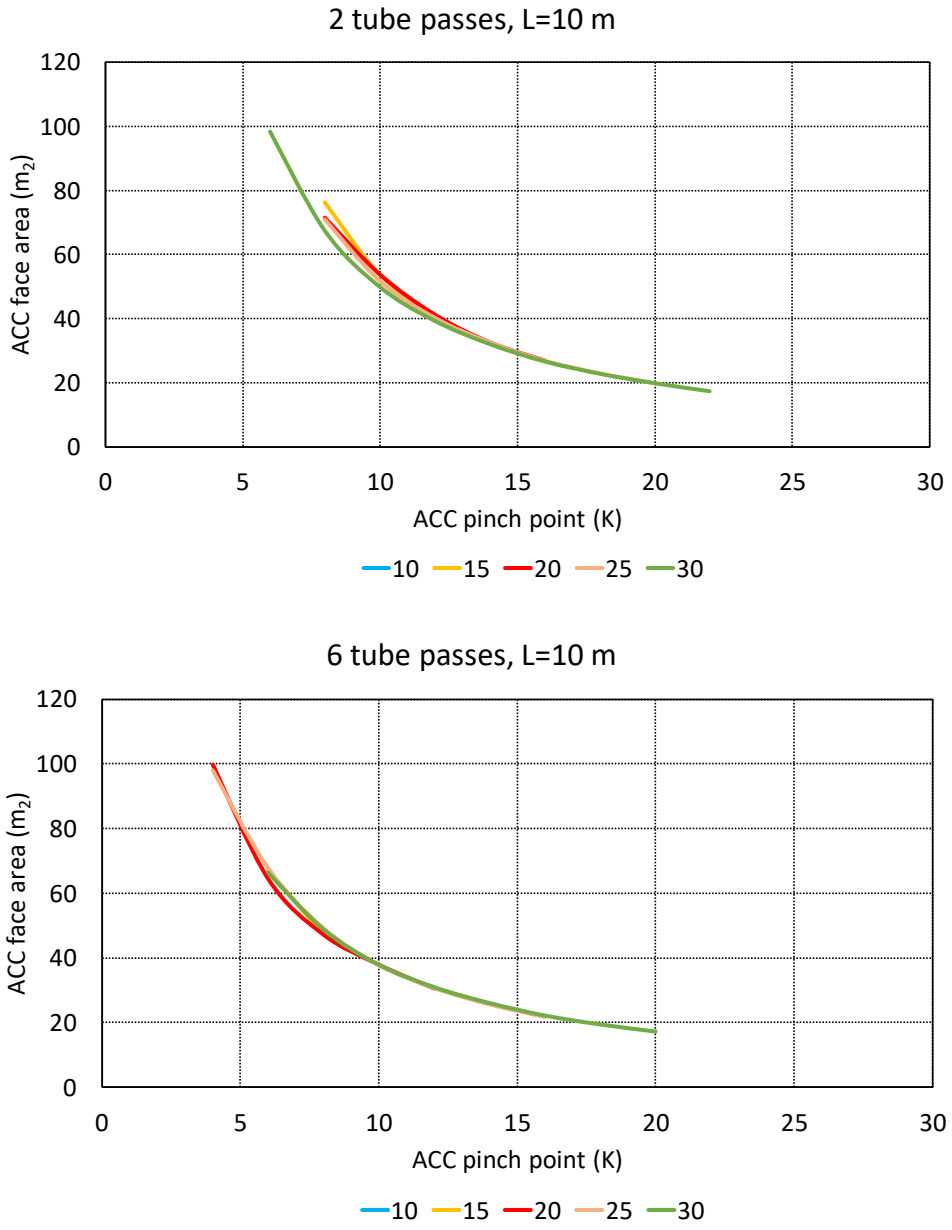

Figure 3.2: ACC face area vs ACC pinch point for 2 & 6 tube pass configuration and 10m total tube length. Each curve corresponds to a different air temperature rise.

Figure 3.3 illustrates the correlation between the ACC fan power consumption and PP_{ACC}.

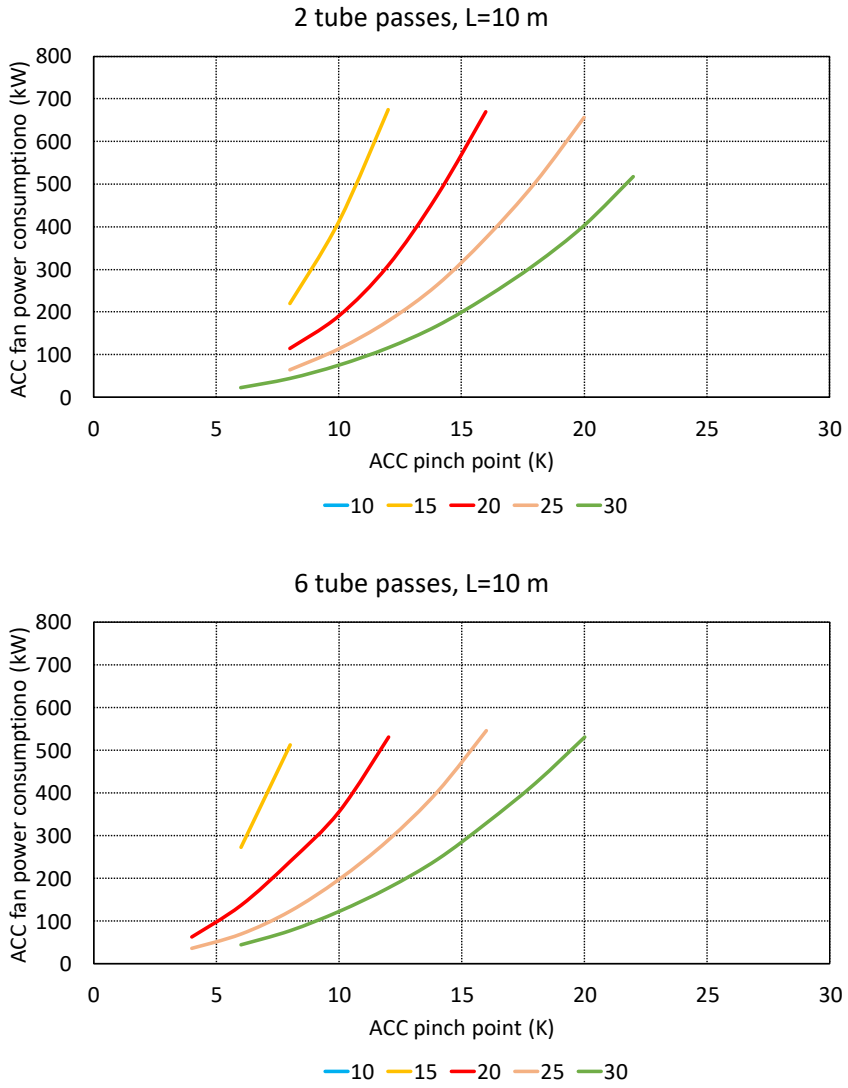

Figure 3.3: ACC fan motor power consumption vs ACC pinch point for 2 & 6 tube pass configuration and 10m total tube length. Each curve corresponds to a different air temperature rise.

The fan power consumption is a crucial factor of the cycle as it influences the overall efficiency of the ORC. ACC fan motor power consumption is defined in equation 2.67, where the direct connection with the air pressure drop and air mass flow rate is observed. Air pressure drop is connected again with air mass flow rate as shown in equations 2.58, 2.31, and 2.32. Higher air mass flow rates and pressure drop values in the ACC result in increased fan motor power consumption, which is detrimental to the overall net power output and thus the electric efficiency of the ORC. To interpret the results, the air pressure drop in the ACC is also plotted, shown in Figure 3.4.

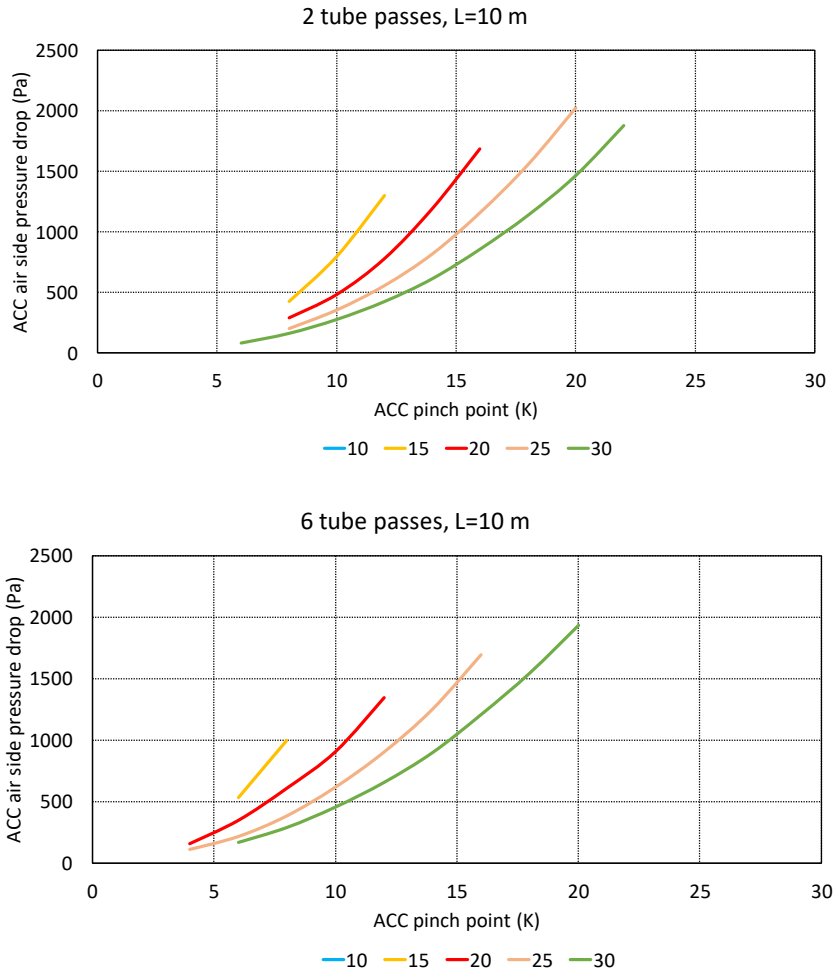

Figure 3.4: Air pressure drop vs ACC pinch point for 2 & 6 tube pass configuration and 10m total tube length. Each curve corresponds to a different air temperature rise.

As it can be observed in Figure 3.3 for a fixed ΔT_{air}, increasing PP_{ACC}, results in higher $P_{e,ACC,fan}$. As PP_{ACC}, is increased, $\dot{Q}_{ACC}$ is increased while A_{face} is decreased, as it was discussed previously. Because of the increasing $\dot{Q}_{ACC}$, $\dot{m}_{air}$ is increased. Meanwhile, because of the increased $\dot{m}_{air}$ and decreased A_{face}, the velocity of the air as it flows between the tubes of the ACC is increased. The combined result of the increased $\dot{m}_{air}$ and air velocity is a significant increase of the pressure drop and $P_{e,fan}$.

As it was previously discussed, ΔT_{air} has an insignificant impact on A_{face}. However, increasing ΔT_{air} results in a very slight decrease in $\dot{Q}_{ACC}$ and a significant decrease in $\dot{m}_{air}$. Because of the significant increase in $\dot{m}_{air}$, the air-side pressure drop along with the fan power consumption are decreased.

In Figure 3.5 the ORC net power output (also considering the fan power consumption) vs the ACC pinch point is presented for 2 and 6 tube passes.

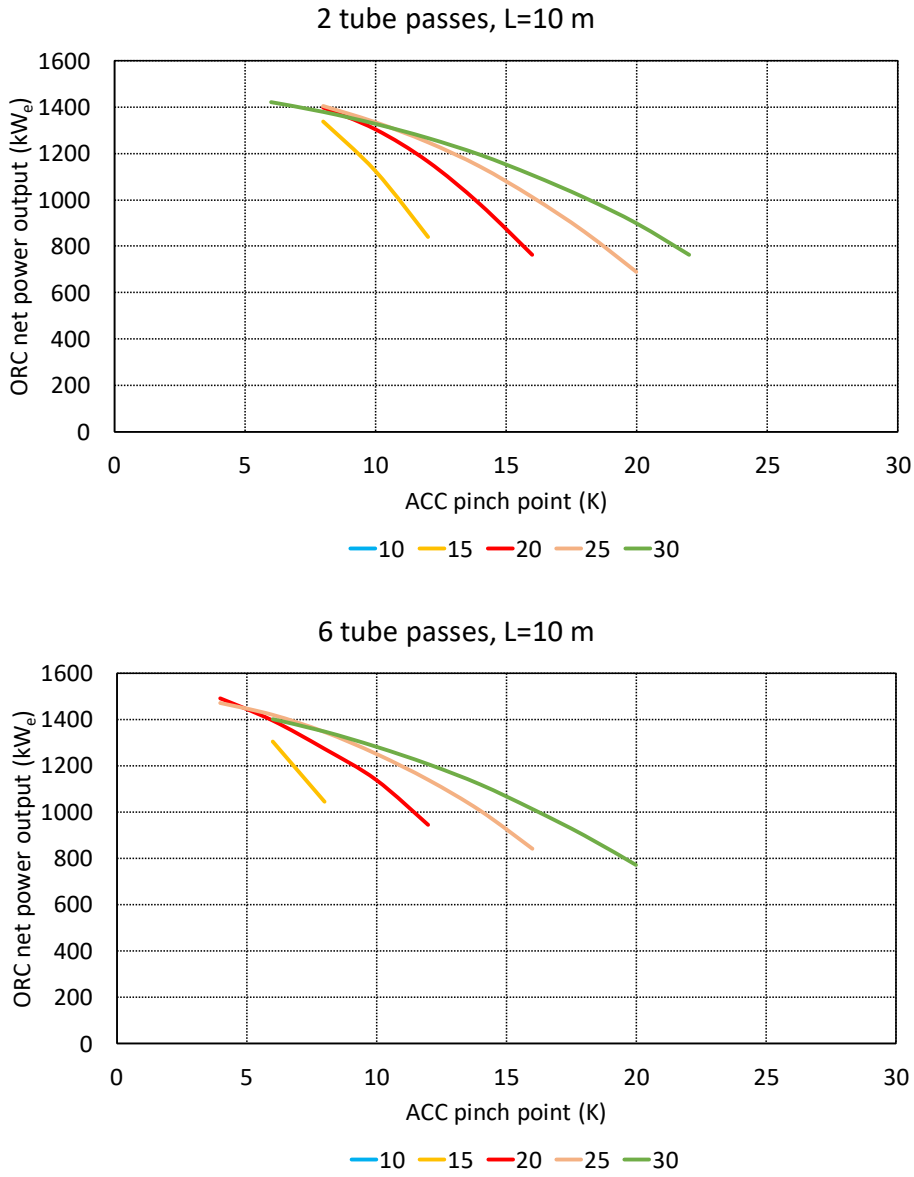

Figure 3.5: ORC net power output vs ACC pinch point for 2 & 6 tube pass configuration and 10m total tube length. Each curve corresponds to a different air temperature rise.

The variation of the net power output is directly mirrored by the variation of the electric efficiency, which is shown in Figure 3.6. Therefore, the results are discussed together.

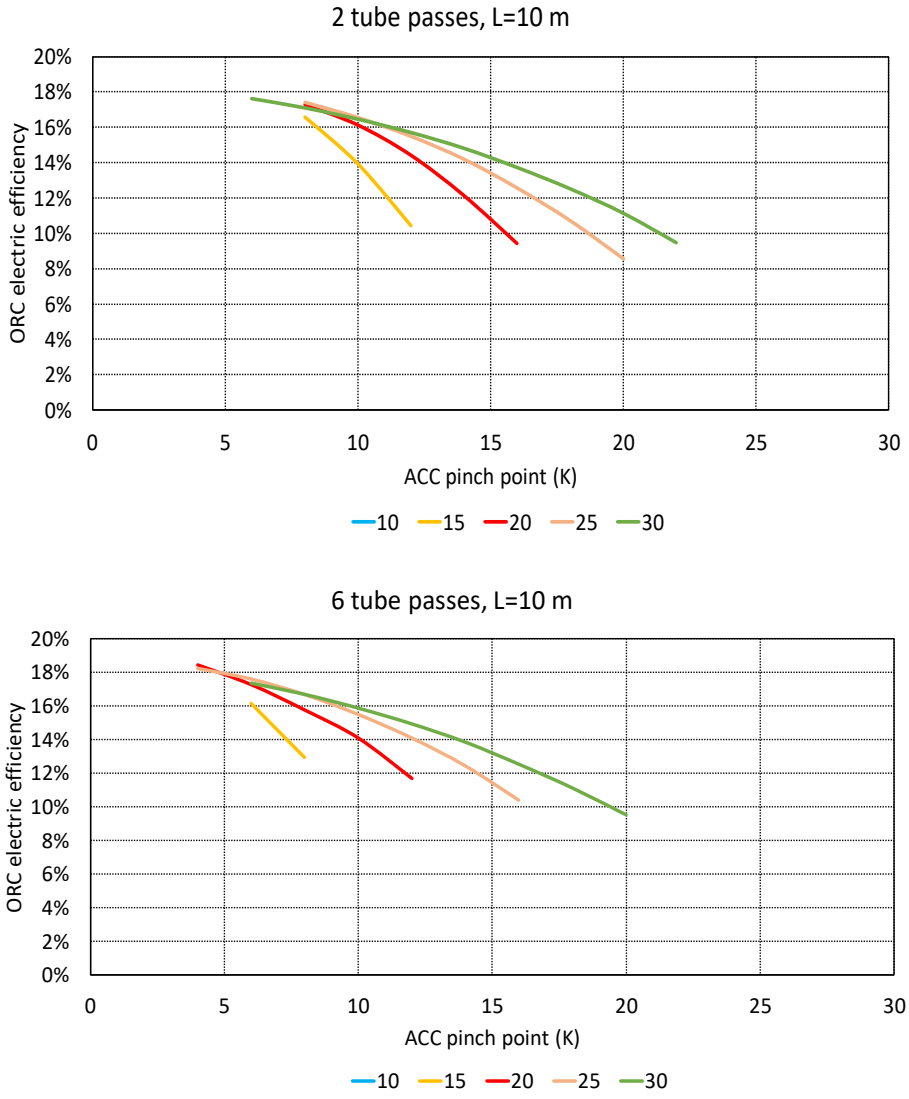

Figure 3.6: ORC electric efficiency vs ACC pinch point for 2 & 6 tube pass configuration and 10m total tube length. Each curve corresponds to a different air temperature rise.

As it was discussed previously, on one hand, for a constant ΔT_{air}, as PP_{ACC} is increased, $P_{e,ACC,fan}$ is increased. On the other hand, because of the increasing condensation temperature/pressure of the ORC, the net power produced by the ORC (excluding the ACC fan power consumption), is decreased. Consequently, increasing the pinch point value results in a substantial deterioration of $P_{e,net}$ and thus of the overall electric efficiency. As showcased in Figure 3.5 and Figure 3.6, this deterioration is far more significant for lower ΔT_{air} values, for which the fan power consumption is considerably higher. As a matter of fact, for the same $PP_{ACC,}$ the net power output is dramatically lower for lower

ΔT_{air}, values. At the same time, for lower ΔT_{air} the decrease in the net power output (and electric efficiency) for increasing PP_{ACC} is far steeper.

In Figure 3.7 the ACC cost is depicted for 2 and 6 tube passes. The ACC cost is closely related to the heat transfer area of the ACC. Therefore, for increasing PP_{ACC} values, under which the ACC area is decreased, the ACC cost is reduced accordingly. For the same reason, the ACC configuration (2 vs 6 passes) and tube length have very little impact on the ACC cost.

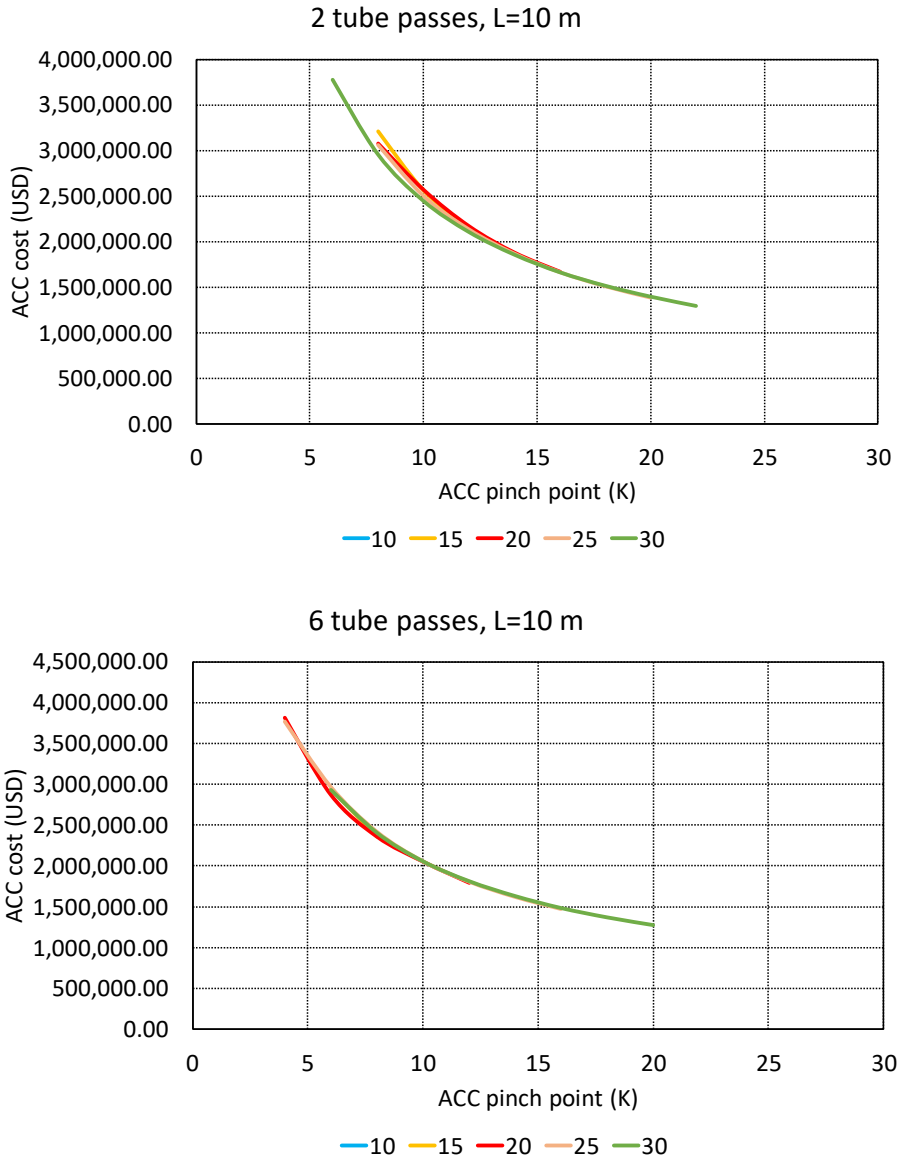

Figure 3.7: ACC Cost vs ACC pinch point for 2 & 6 tube pass configuration and 10m total tube length. Each curve corresponds to a different air temperature rise.

As it was discussed in the previous section of the thesis, both technical and economic criteria must be evaluated. Regarding the ACC, one parameter that can be used for a combined evaluation of the techno-economic influence of the ACC design is the specific cost of the ACC, which was introduced in eq. 2.69.

In Figure 3.8 the specific cost of the ACC vs the ACC pinch point is presented. On one hand, a decrease in PP_{ACC} results in higher net electrical power output, presenting a favorable outcome. However, the cost of the ACC because of the increasing ACC area has also increased. According to Figure 3.8, for each value of ΔT_{air}, there is an optimal PP_{cond} which minimizes the specific ACC cost, presenting an optimal techno-economic design. The optimal PP_{ACC} is strongly related to ΔT_{air}. More specifically, higher PP_{ACC} values are optimal for increasing ΔT_{air} values. The reason is that as ΔT_{air} is increased, the fan motor power consumption tends and the net power output is reduced at a much lower rate for increasing PP_{ACC} values. Therefore, for higher ΔT_{air} values, as the PP_{ACC} is increased, the penalty in the net power output is not that significant, while the ACC area is reduced at the same rate (Figure 3.7). Generally, it can be observed that the optimal PP_{cond} ranges between a minimum of 8-10 K to a maximum of around 15 K for ΔT_{air} values of 20 K and 30 K, respectively. The global minimum of the specific ACC cost appears for the highest ΔT_{air} and is equal to around 1500 €/kW$_e$. Notably, this value is very high considering the reported specific investment costs of ORC units in the literature. However, it must be highlighted that in the present thesis, the costs have been adapted to 2023 values using the CEPCI index, under which an increase of 50% is considered compared to prices before 2019. Finally, it must be noted that the same conclusions hold for both 2- and 6-tube pass configurations.

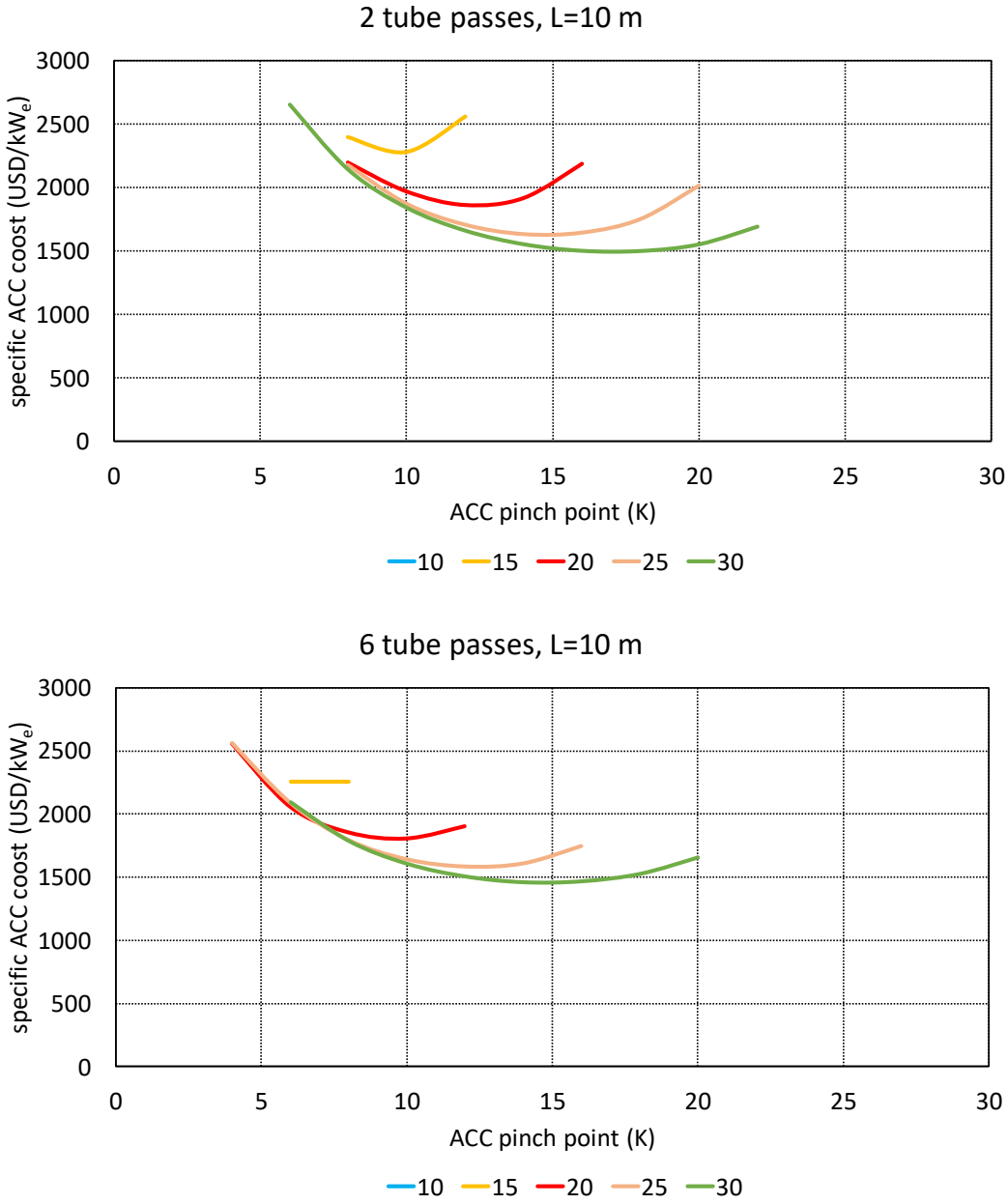

Figure 3.8: Specific ACC cost vs ACC pinch point for 2 & 6 tube pass configuration and 10m total tube length. Each curve corresponds to a different air temperature rise.

3.2 Parametric analysis of ACC pinch point and air temperature rise 2, 6 tube passes and 15 m total ACC tube length

In Figure 3.9-Figure 3.16: Specific ACC cost vs ACC pinch point for 2 & 6 tube pass configuration and 15m total tube length. Each curve corresponds to a different air temperature rise the parametric analysis for the 15 m total tube length is presented. All diagrams are of the same type as those that were presented in the previous section, corresponding to a tube length of 10 meters. Generally, the qualitative relationships between the investigated parameters are similar to what was discussed in the previous section. Therefore, all explanations and conclusions made in section 3.1 apply to this set of results too. However, there are some explanations regard to calculated quantities, which are discussed.

Generally, it can be observed that the acceptable PP_{ACC} ranges (considering the constraints taken into account in the ACC model) of the curves are smaller and transposed toward smaller pinch point values. This happens because of the constraint for the aspect ratio of the ACC. In particular, because the tube length is longer, the required ACC area is obtained with fewer tubes in the x dimension and thus with lower ACC widths. Therefore, generally, the aspect ratios of the ACC designs in the case of longer tube lengths are higher. For higher PP_{ACC} values, the required ACC area is lower, therefore, the ACC sizing model tends to produce designs with even smaller ACC widths, which are not acceptable based on the aspect ratio constraint.

In Figure 3.9 the ACC heat transfer area vs the ACC pinch point is presented for 2 and 6 tube passes. Compared to the 10 m length tube, the ACC heat transfer area in the 15m tube length is smaller, for the PP_{ACC} for which valid designs appear. This phenomenon can be explained by the equations of section 2.1.3 where the required heat transfer area $\mathrm{A_{ACC}}$ is calculated. It appears that for longer tubes the overall heat transfer coefficient (U) is higher. By analysing eq. 2.25 of the U_{des}, both a_{air}, $a_{wf,des}$ and η_{fw} have higher values in 15m tube length, resulting in a higher value of U_{des}. The same conclusions apply to the U_{cond} as well. At the same time in equation 2.23 of heat duty in the ACC, the heat duty remains the same for the same temperature conditions. So an increase in the heat transfer coefficient results in a reduction in the ACC heat transfer area.

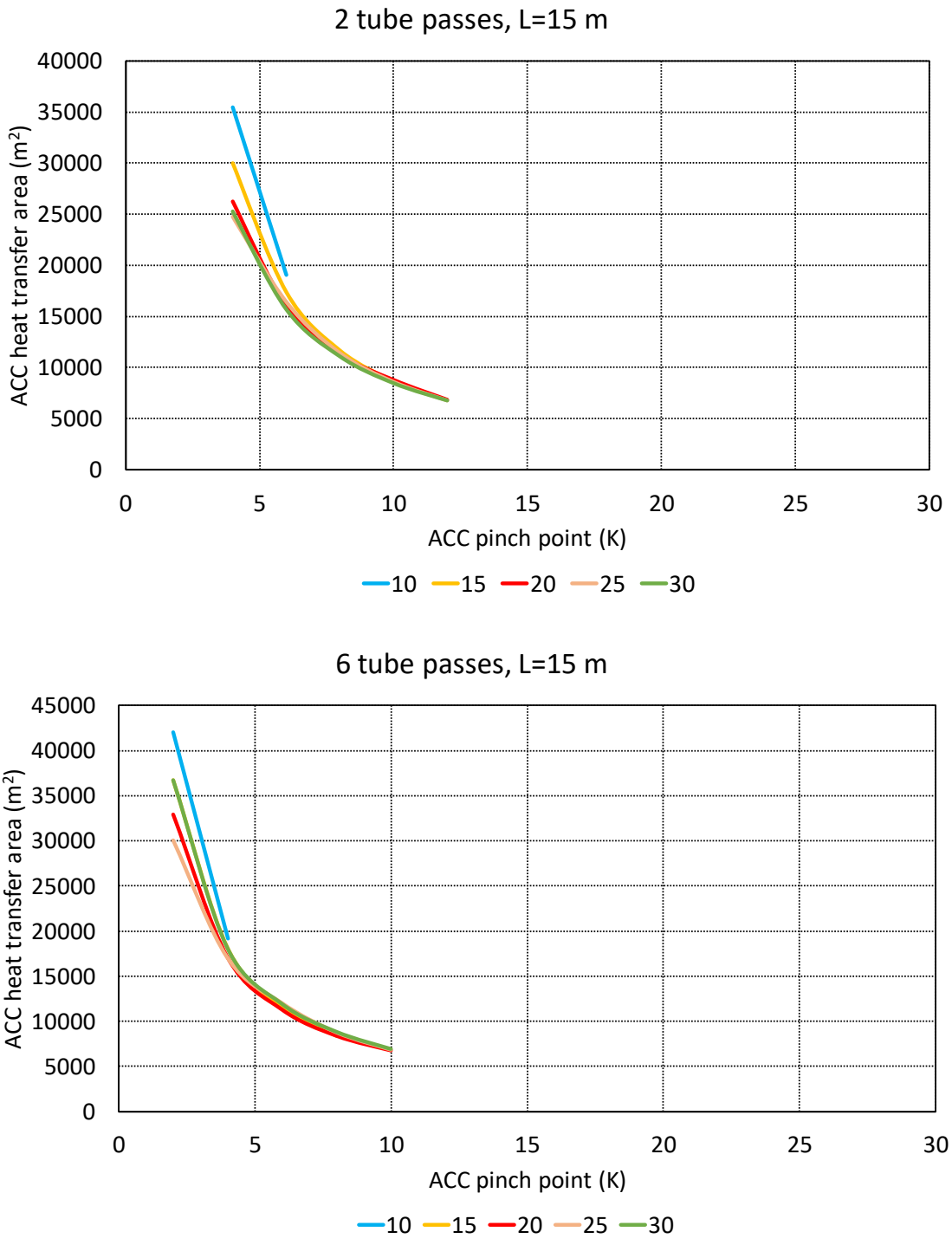

Figure 3.9: ACC heat transfer area vs ACC pinch point for 2 & 6 tube pass configuration and 15m total tube length. Each curve corresponds to a different air temperature rise.

In Figure 3.10 the A_{face} vs the PP_{ACC} is presented for 2 and 6 tube passes. The surface area in the 15 m tube length follows the same behaviour as the ACC heat transfer area. Specifically, for this scenario, it seems that the valid pinch point range generally requires bigger surfaces to cover the heat duty of the ACC.

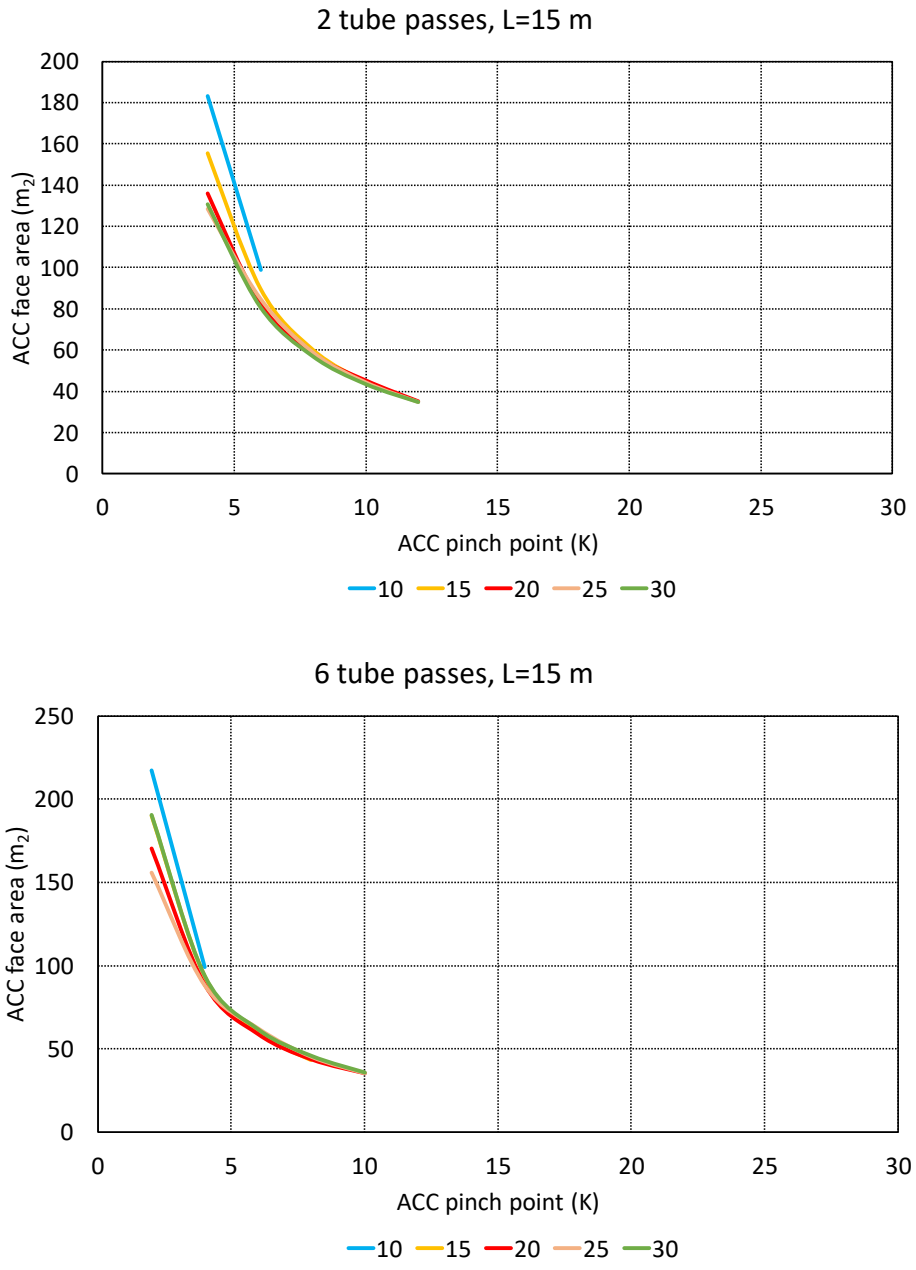

Figure 3.10: ACC face area vs ACC pinch point for 2 & 6 tube pass configuration and 15m total tube length. Each curve corresponds to a different air temperature rise.

Figure 3.11 illustrates the connection between the $P_{e,ACC,fan}$ vs the PP_{ACC} for 2 and 6-tube passes. To interpret the results, the air pressure drop in the ACC is also plotted, shown in Figure 3.12.

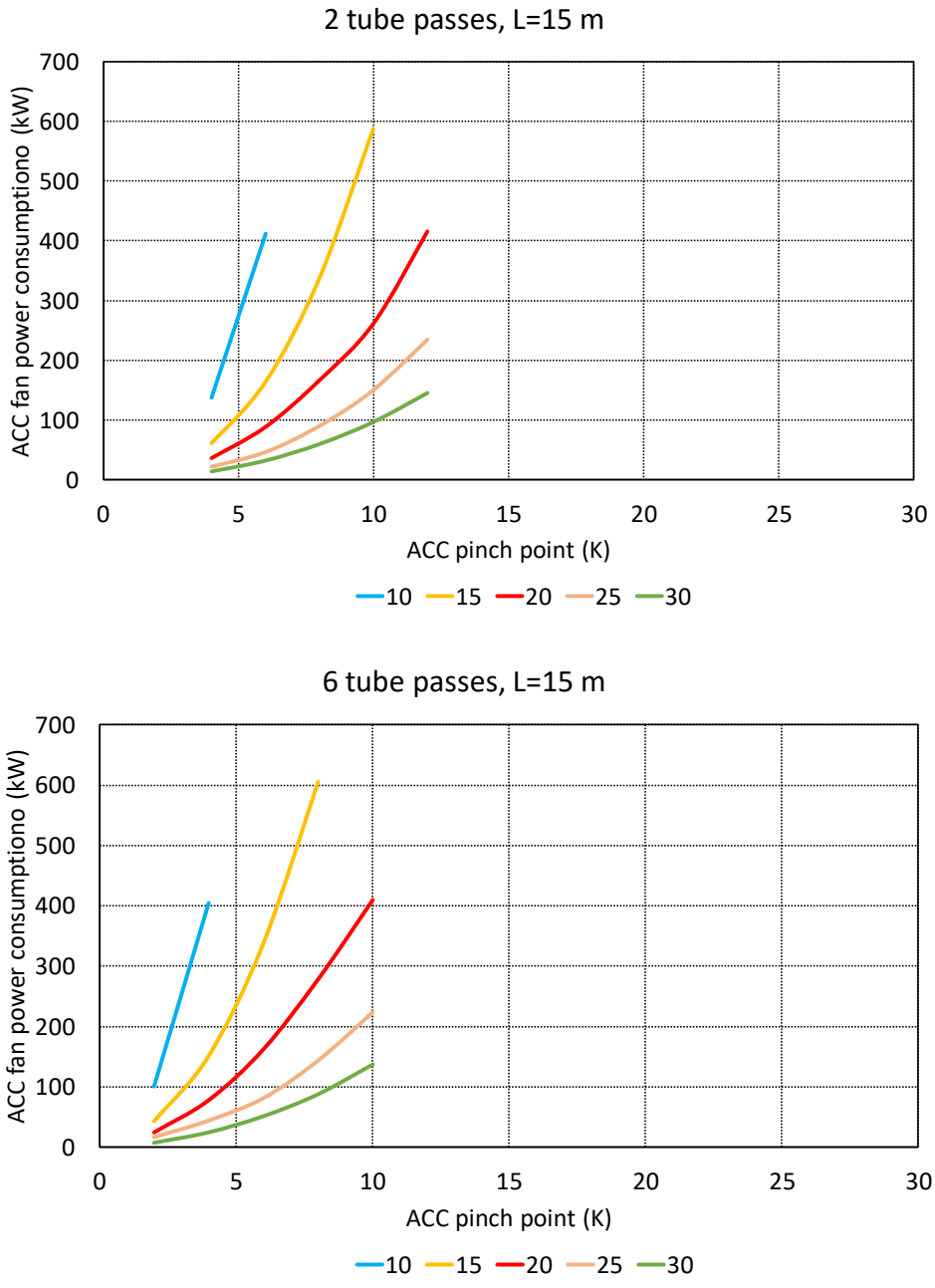

Figure 3.11: ACC fan power consumption vs ACC pinch point for 2 & 6 tube pass configuration and 15m total tube length. Each curve corresponds to a different air temperature rise.

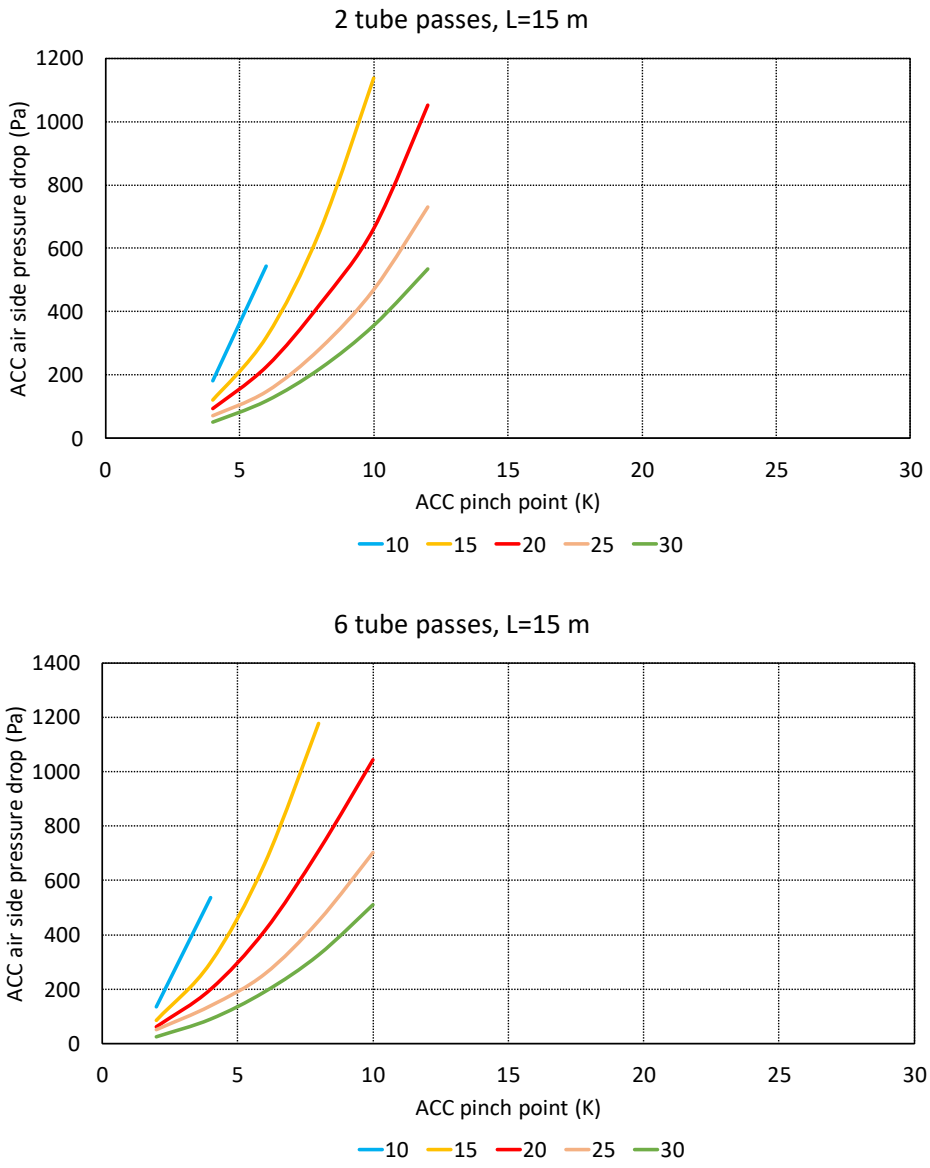

Figure 3.12: ACC air side pressure drop vs ACC pinch point for 2 & 6 tube pass configuration and 15m total tube length. Each curve corresponds to a different air temperature rise

The comparison for the L_t indicates that for $L_t = 15m$, ΔP_{air} has hiher values. The explanation comes from the definition of ΔP_{air} in equation 2.58. ΔP_{air} depends on $u_{air,max}$. From equations 2.31, 2.32, and 2.7 it can be concluded that an increase in the L_t reduces the A_{face} and therefore increases the $u_{air,max}$, resulting in a higher ΔP_{air}. ΔP_{air} is connectd with $P_{e,ACC,fan}$ through eq. 2.67, thus $P_{e,ACC,fan}$ has also higher values for $L_t = 15m$.

In Figure 3.13 ORC net power output vs the ACC pinch point is presented for 2 and 6 tube passes. The variation of the net power output is directly mirrored by the variation of the electric efficiency, which is shown in Figure 3.14. Therefore, the results are discussed together.

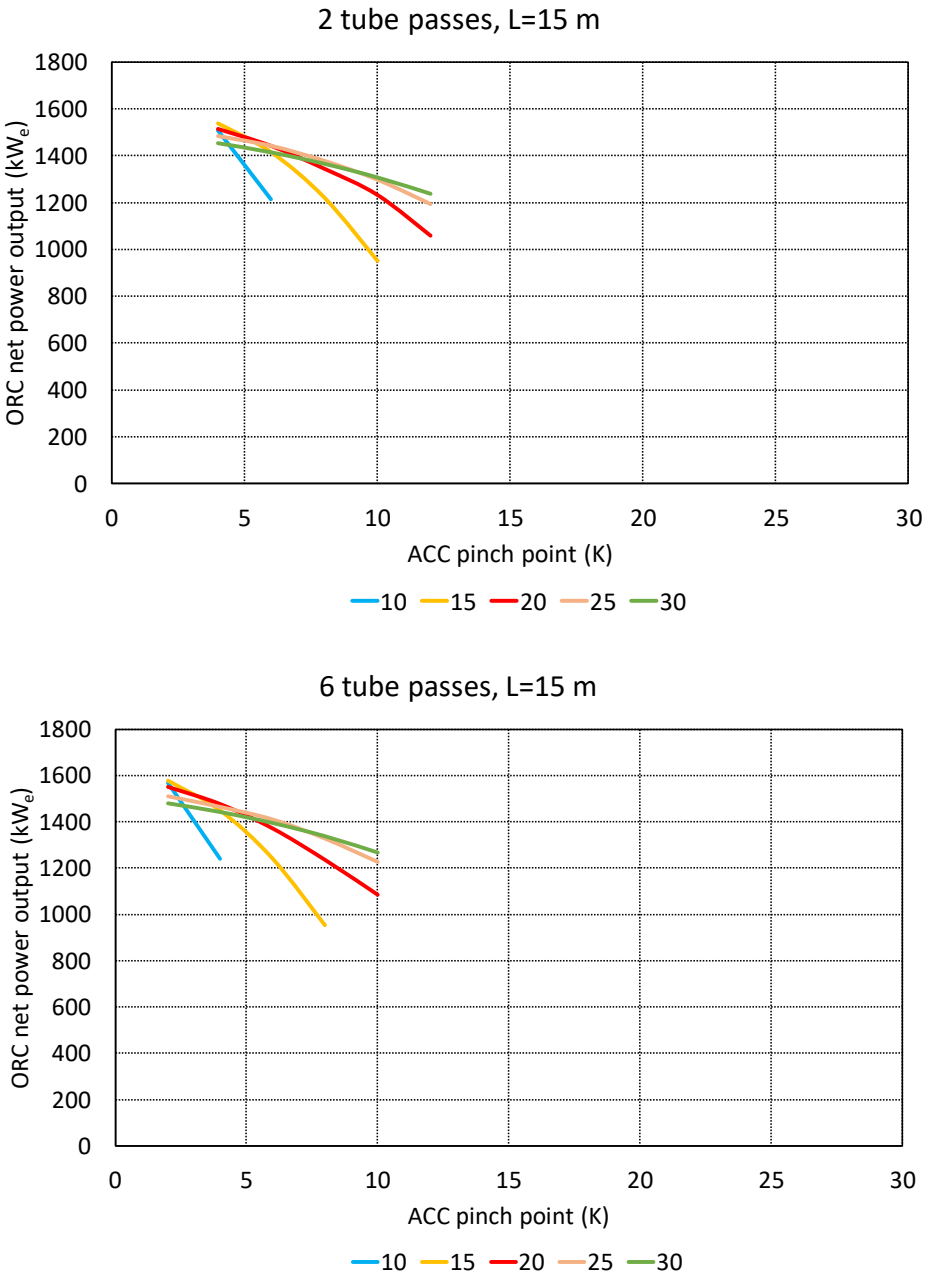

Figure 3.13: ORC net power output vs ACC pinch point for 2 & 6 tube pass configuration and 15m total tube length. Each curve corresponds to a different air temperature rise.

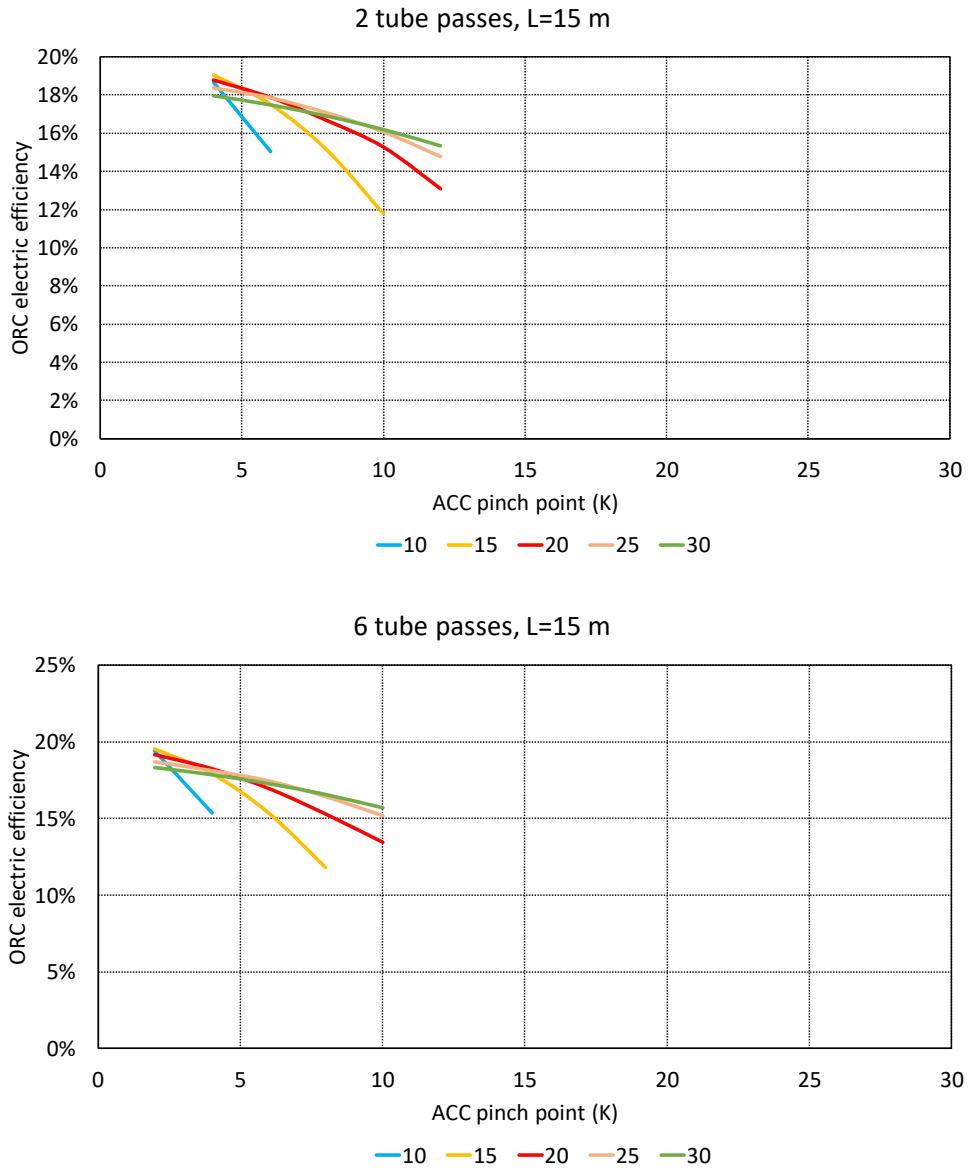

Figure 3.14: ORC electric efficiency vs ACC pinch point for 2 & 6 tube pass configuration and 15m total tube length. Each curve corresponds to a different air temperature rise.

As it was discussed previously, for $L_t = 15m$, $P_{e,ACC,fan}$ is increased for the same conditions of PP_{ACC} and ΔT_{air} comparing with $L_t = 10m$. Consequently, deterioration of $P_{e,net}$ and thus of the overall electric efficiency appears in the scenario of $L_t = 15m$.

In Figure 3.15 vs the PP_{ACC} is presented for 2 and 6 tube passes. According to eq. 2.70, the C_{ACC} is dependent on the heat transfer area A_{ACC}. Therefore, lower values of C_{ACC} are expected or $L_t = 15m$ for the common PP_{ACC} range and ΔT_{air}, due to the smaller A_{ACC}, as discussed in Figure 3.9. For

small PP_{ACC}, it is made clear from the diagram that C_{ACC} becomes notably higher and with a steeper slope. These values correspond to A_{ACC} bigger than $10{,}000\ m^2$. As mentioned in section 2.1.5, this range is outside the valid range of the cost correlation.

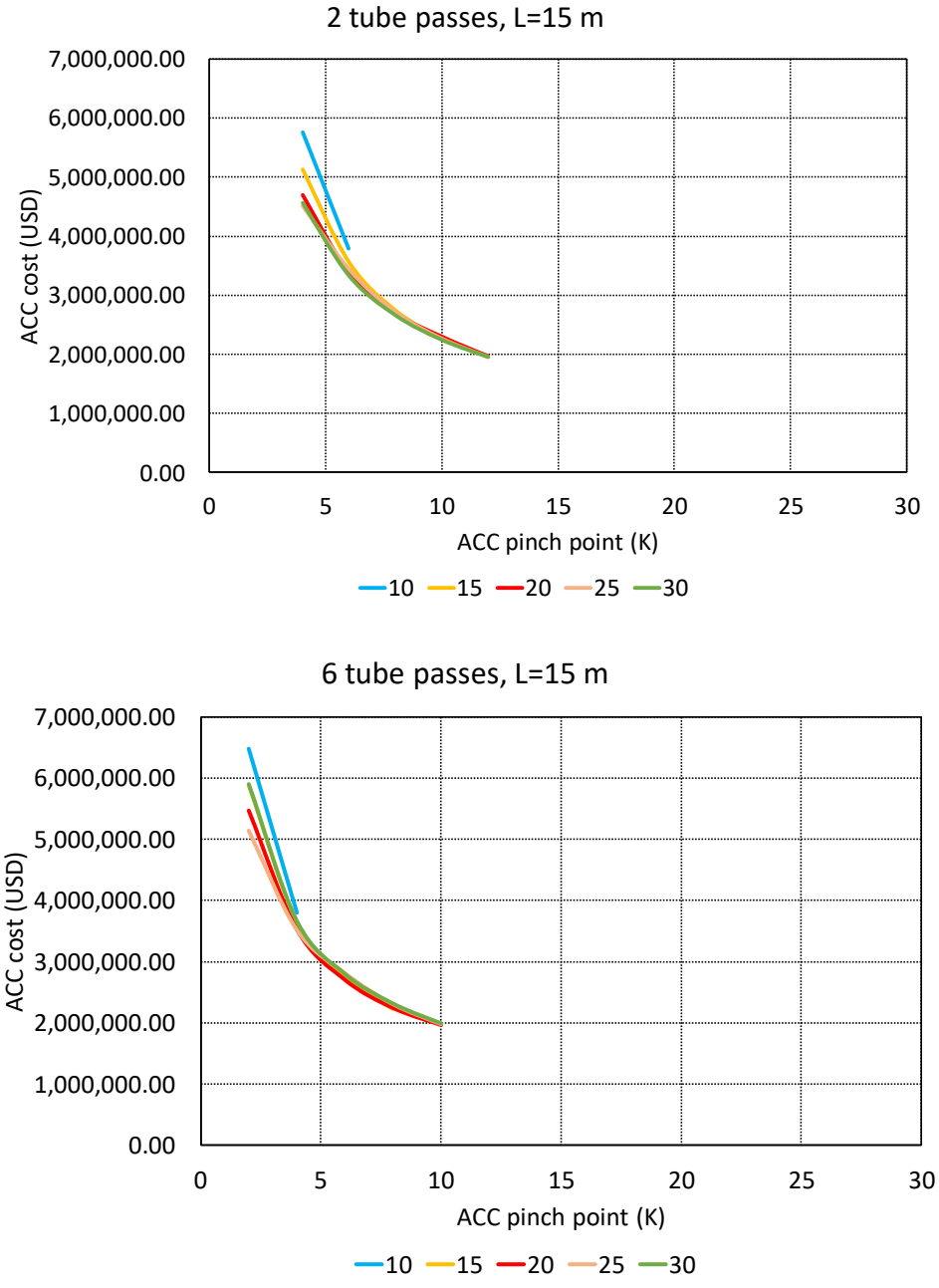

Figure 3.15: ACC cost vs ACC pinch point for 2 & 6 tube pass configuration and 15m total tube length. Each curve corresponds to a different air temperature rise

In Figure 3.16 the $C_{ACC,sp}$ vs the PP_{ACC} is presented for 2 and 6 tube passes. Relatively with the C_{ACC}, lower values of $C_{ACC,sp}$ are observed for the common PP_{ACC} range of 10 & 15 m tube length configurations. It can be observed that the optimal PP_{cond} ranges from 10-12 K for ΔT_{air} values of 20 K to 30 K. The global minimum of the specific ACC cost appears for the highest ΔT_{air} and is equal to around 1600 €/kW$_e$. Notably, this value is very high considering the reported specific investment costs of ORC units in the literature as mentioned earlier in this thesis.

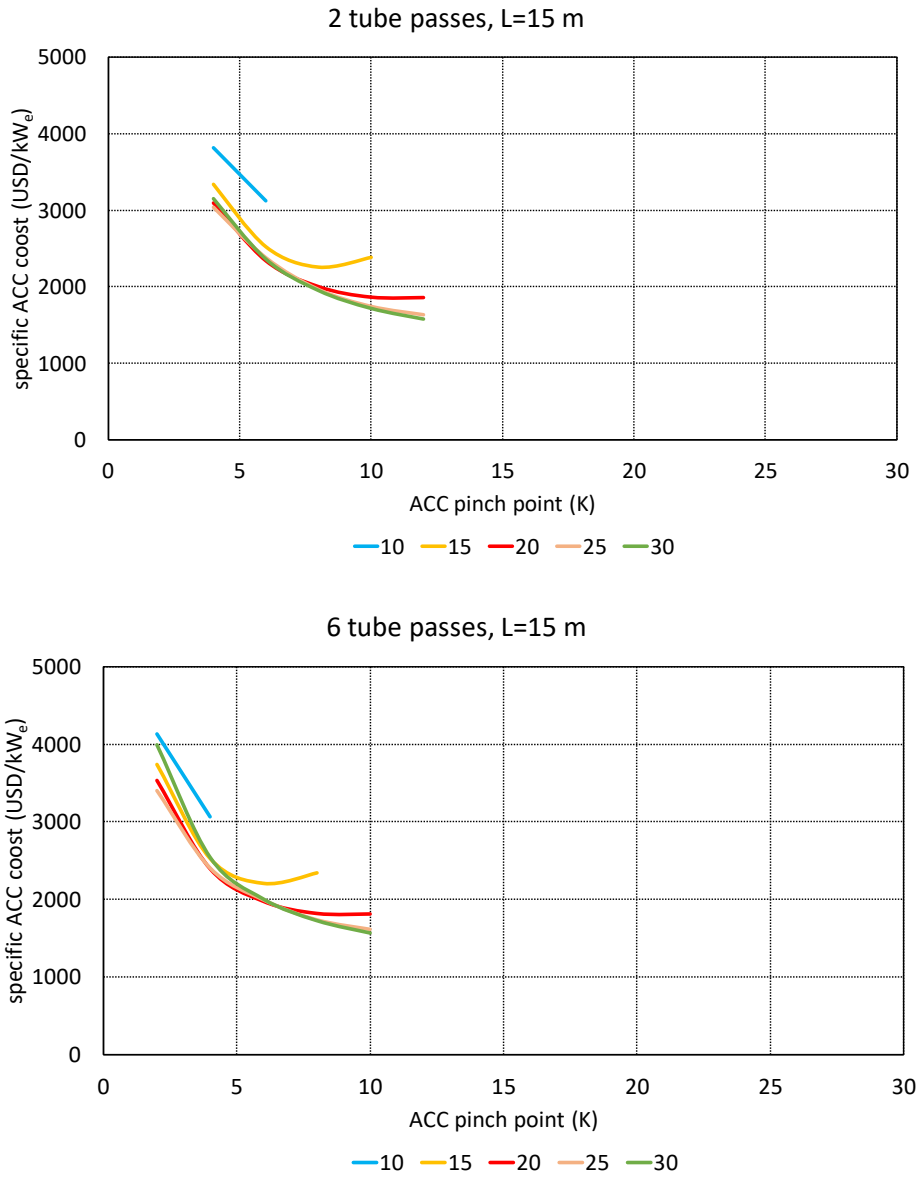

Figure 3.16: Specific ACC cost vs ACC pinch point for 2 & 6 tube pass configuration and 15m total tube length. Each curve corresponds to a different air temperature rise

3.3 Parametric analysis of ACC pinch point and air temperature rise 2, 6 tube passes and 20 m total ACC tube length

In Figure 3.17- Figure 3.24 the parametric analysis for the 20 m total tube length is presented. Each curve corresponds to a different air temperature rise (ΔT_{air}). All diagrams are of the same type as those that were presented in section 3.1, corresponding to a tube length of 10 meters. Generally, the qualitative relationships between the investigated parameters are similar to what was discussed in section 3.1. Therefore, all explanations and conclusions made in section 3.1 apply to this set of results too.

Moreover, it can be observed that the acceptable PP_{ACC} ranges (considering the constraints taken into account in the ACC model) of the curves are smaller than the 15m tube length set of results and transposed toward even smaller pinch point values. This happens again because of the constraint for the aspect ratio of the ACC. In particular, because the tube length is longer, the required ACC area is obtained with fewer tubes in the x dimension and thus with lower ACC widths. Therefore, generally, the aspect ratios of the ACC designs in the case of longer tube lengths are higher. For higher PP_{ACC} values, the required ACC area is lower, therefore, the ACC sizing model tends to produce designs with even smaller ACC widths, which are not acceptable based on the aspect ratio constraint. Therefore, all explanations and conclusions made in section **Error! Reference source not found.** about the comparison of 10 and 15 meters tube length, apply to this set of results too.

In Figure 3.17 the A_{ACC} vs the $PP_{ACC}$is presented for 2 and 6 tube passes.

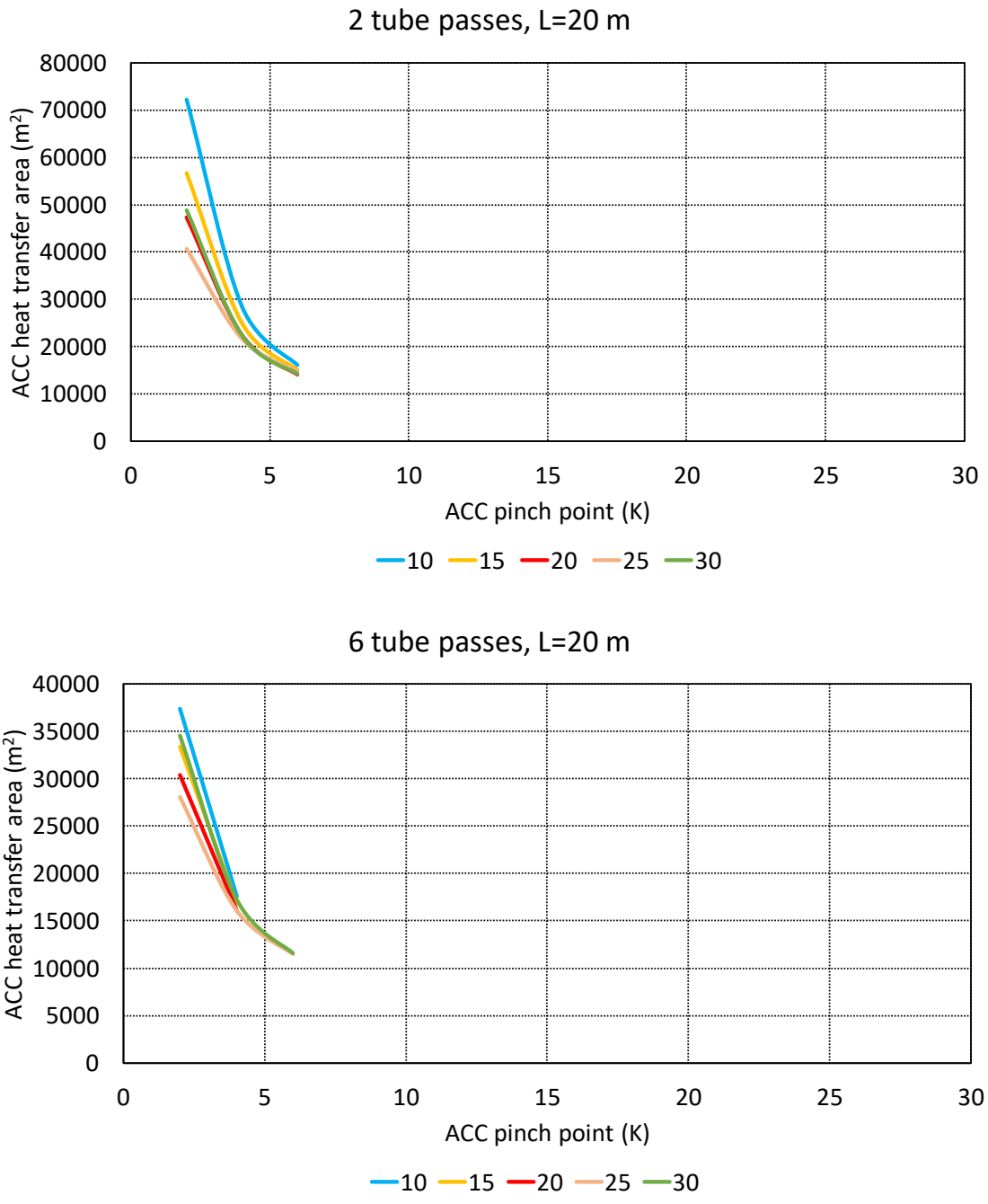

Figure 3.17: ACC heat transfer area vs ACC pinch point for 2 & 6 tube pass configuration and 15m total tube length. Each curve corresponds to a different air temperature rise

In Figure 3.18 A_{face} vs the PP_{ACC} is presented for 2 and 6 tube passes.

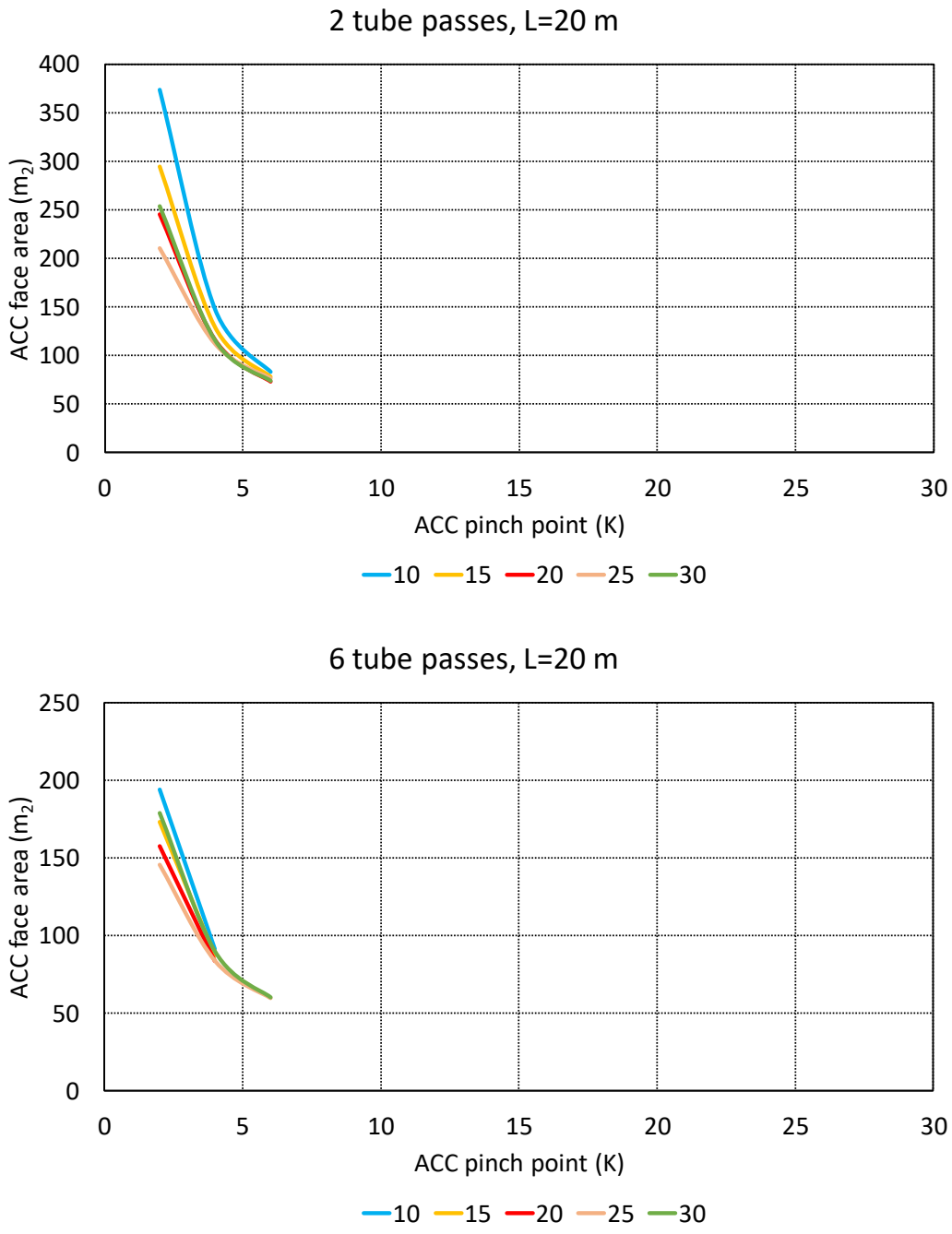

Figure 3.18: ACC face area vs ACC pinch point for 2 & 6 tube pass configuration and 20m total tube length. Each curve corresponds to a different air temperature rise

In Figure 3.19 $P_{e,ACC,fan}$ vs the PP_{ACC} is presented for 2 and 6 tube passes.

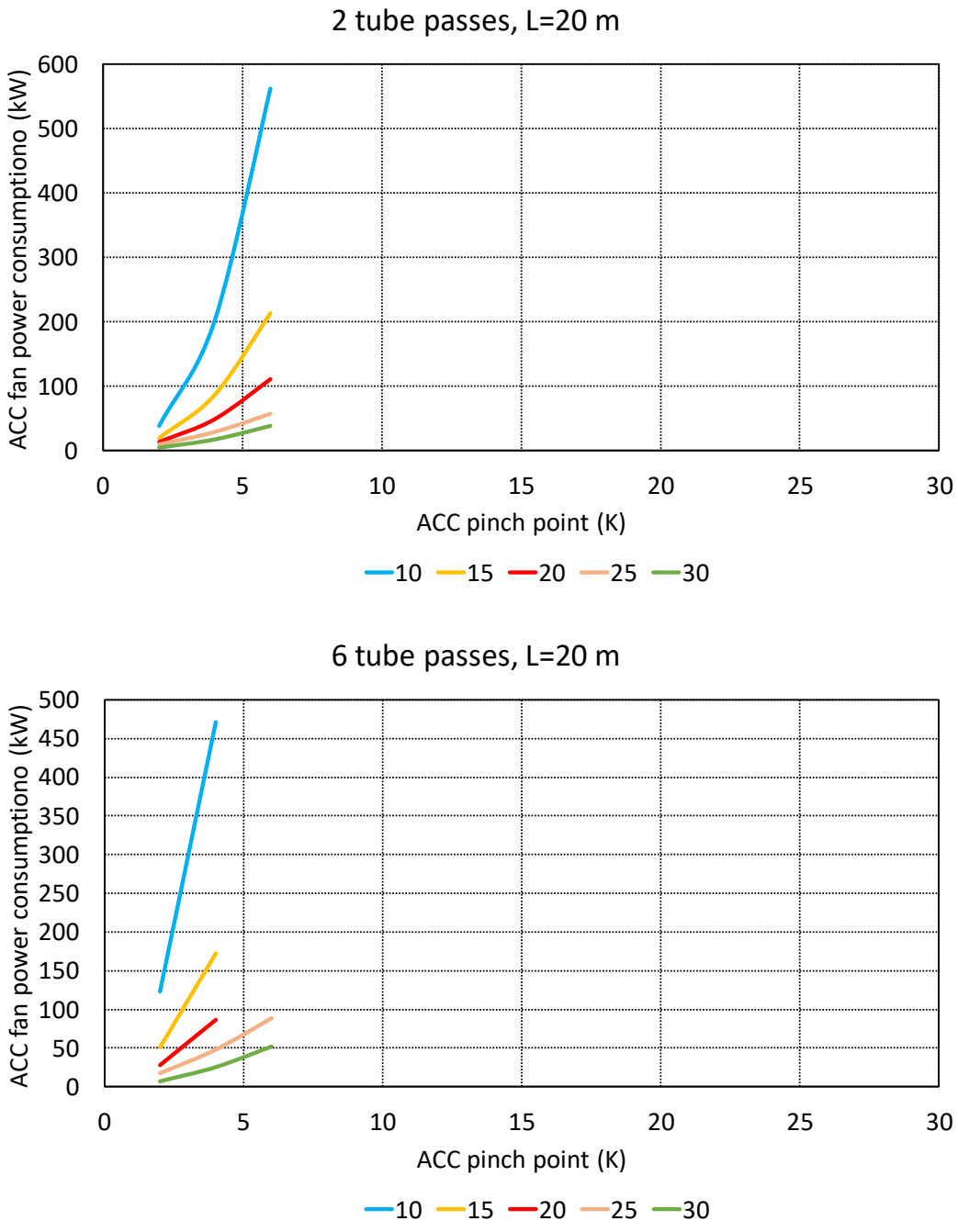

Figure 3.19: ACC fan power consumption vs ACC pinch point for 2 & 6 tube pass configuration and 20m total tube length. Each curve corresponds to a different air temperature rise

In Figure 3.20 ΔP_{air} vs the PP_{ACC} is presented for 2 and 6 tube passes.

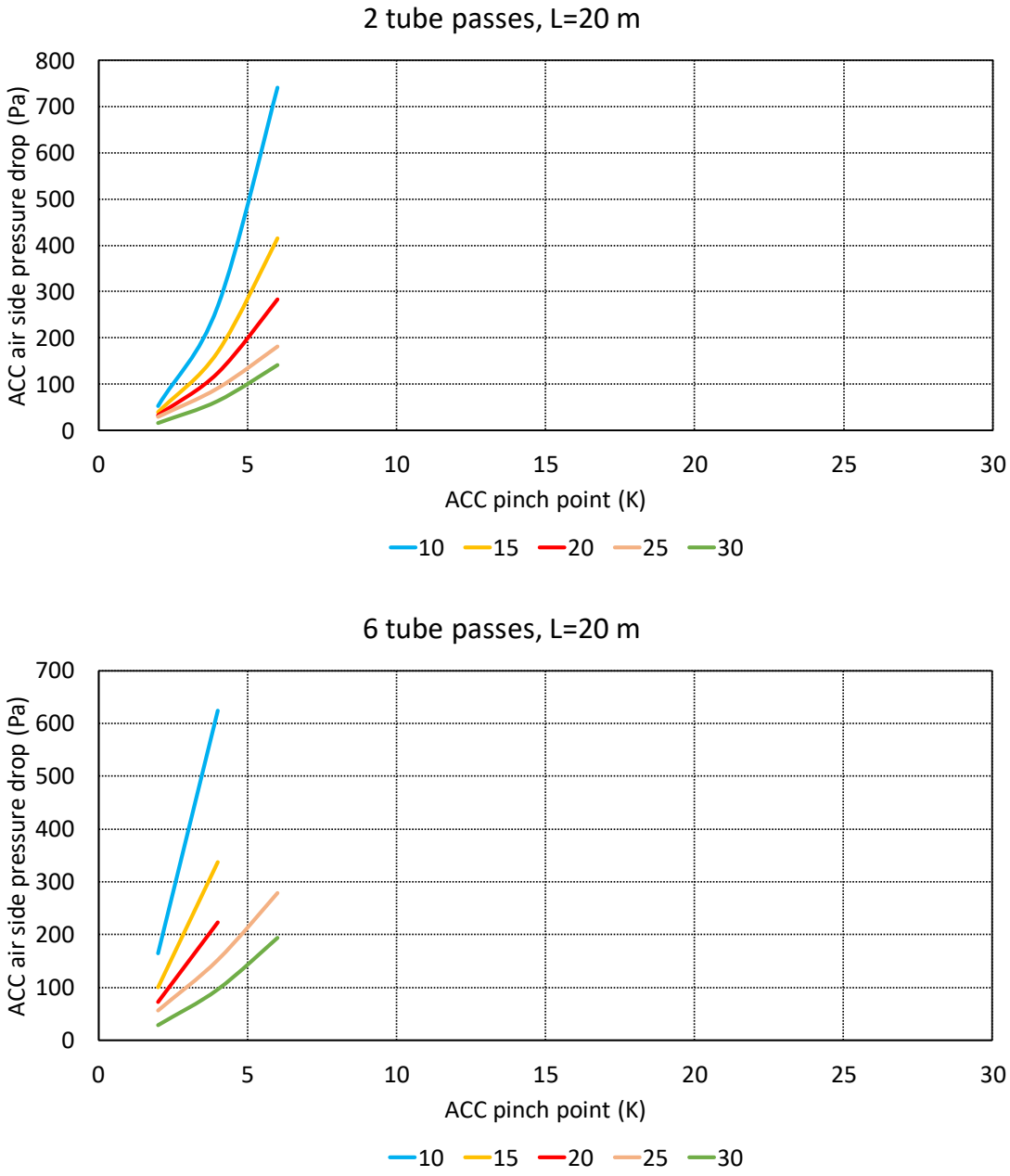

Figure 3.20: ACC air side pressure drop vs ACC pinch point for 2 & 6 tube pass configuration and 20m total tube length. Each curve corresponds to a different air temperature rise

In Figure 3.21 the electric efficiency vs the PP_{ACC} is presented for 2 and 6 tube passes.

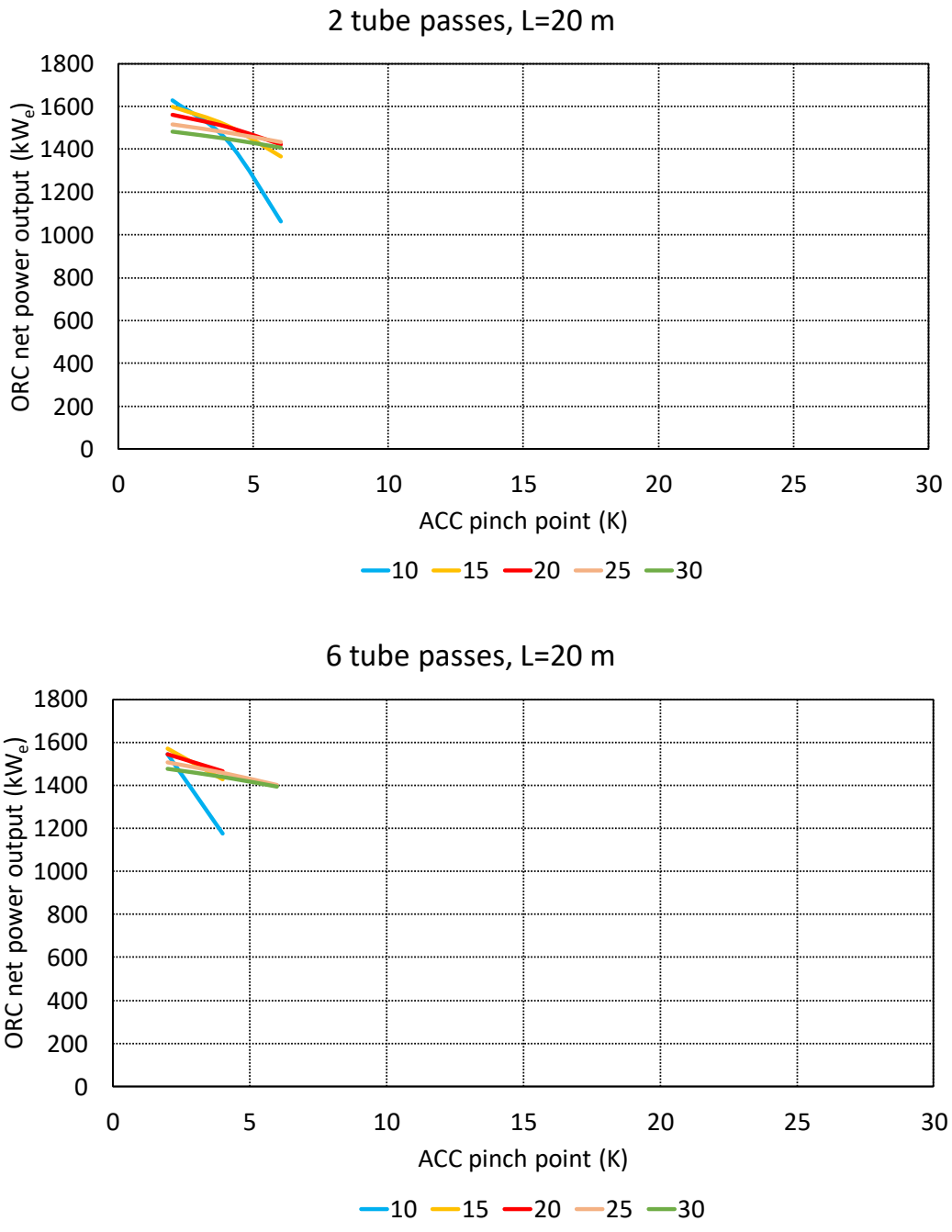

Figure 3.21: ORC net power output vs ACC pinch point for 2 & 6 tube pass configuration and 20m total tube length. Each curve corresponds to a different air temperature rise

In Figure 3.22 $\eta_{e,net,ORC}$ vs the P is presented for 2 and 6 tube passes.

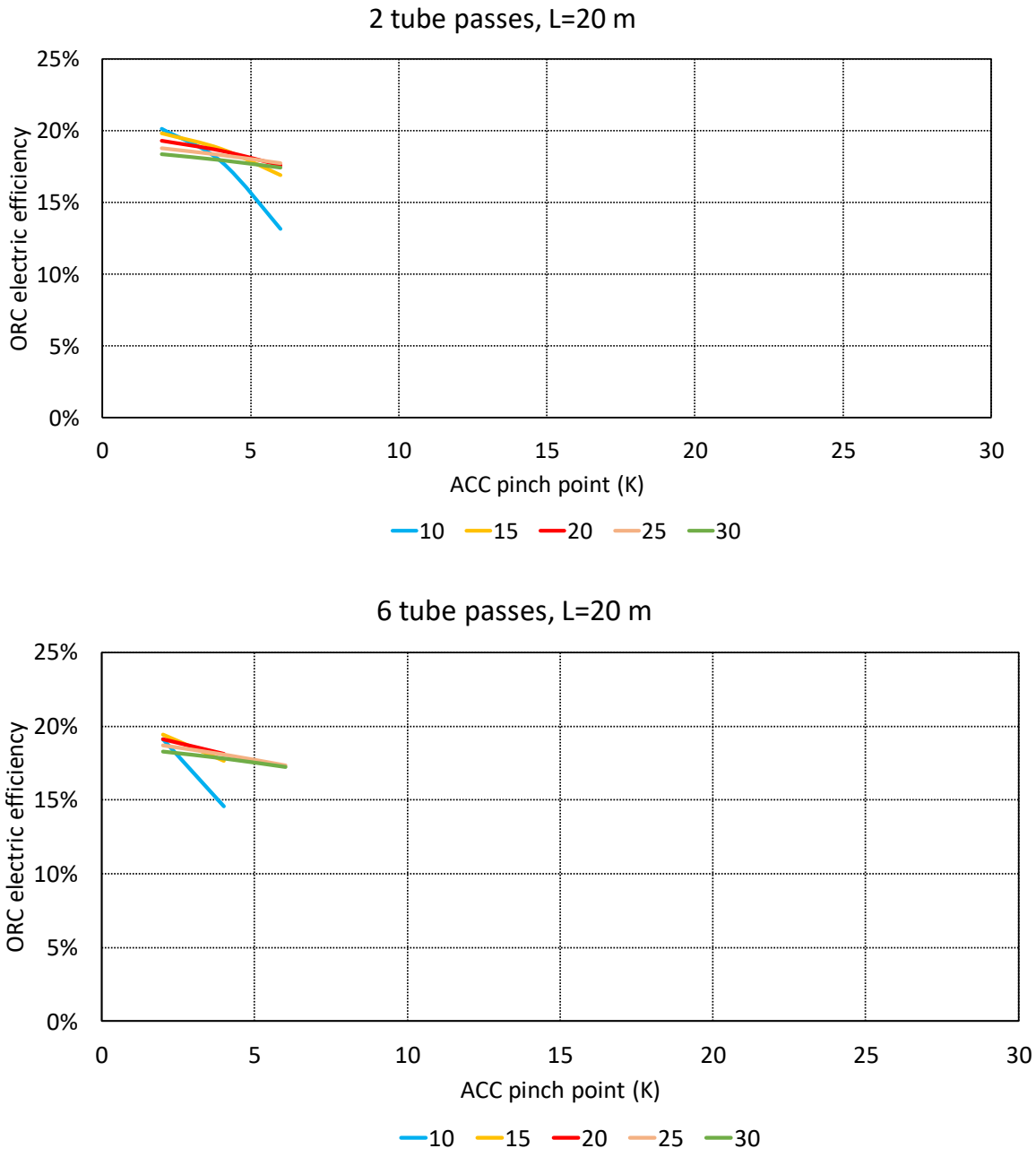

Figure 3.22: ORC electric efficiency vs ACC pinch point for 2 & 6 tube pass configuration and 20m total tube length. Each curve corresponds to a different air temperature rise

In Figure 3.23 ACC cost vs the ACC pinch point is presented for 2 and 6 tube passes.

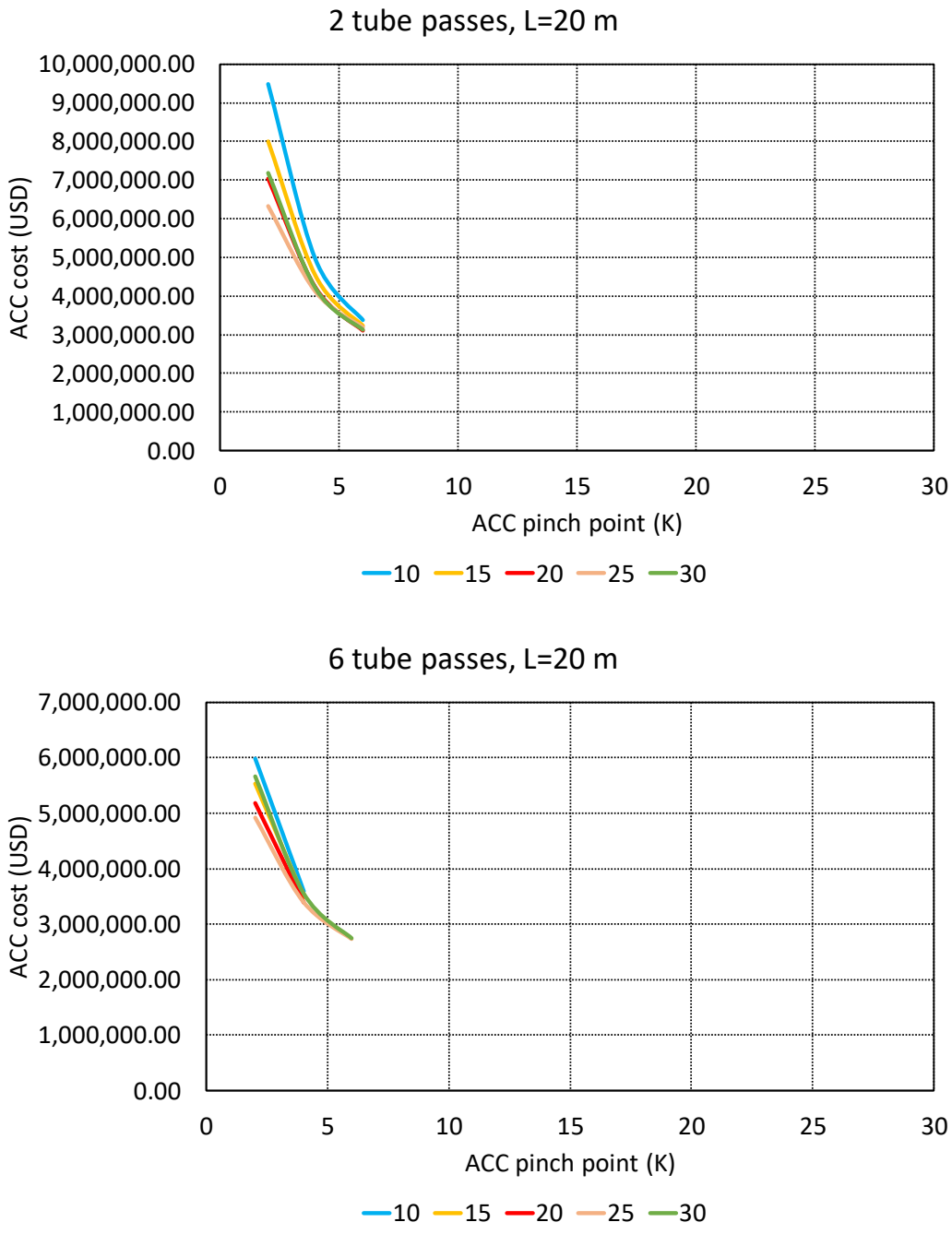

Figure 3.23: ACC cost vs ACC pinch point for 2 & 6 tube pass configuration and 20m total tube length. Each curve corresponds to a different air temperature rise

In Figure 3.24 specific ACC cost vs the ACC pinch point is presented for 2 and 6 tube passes.

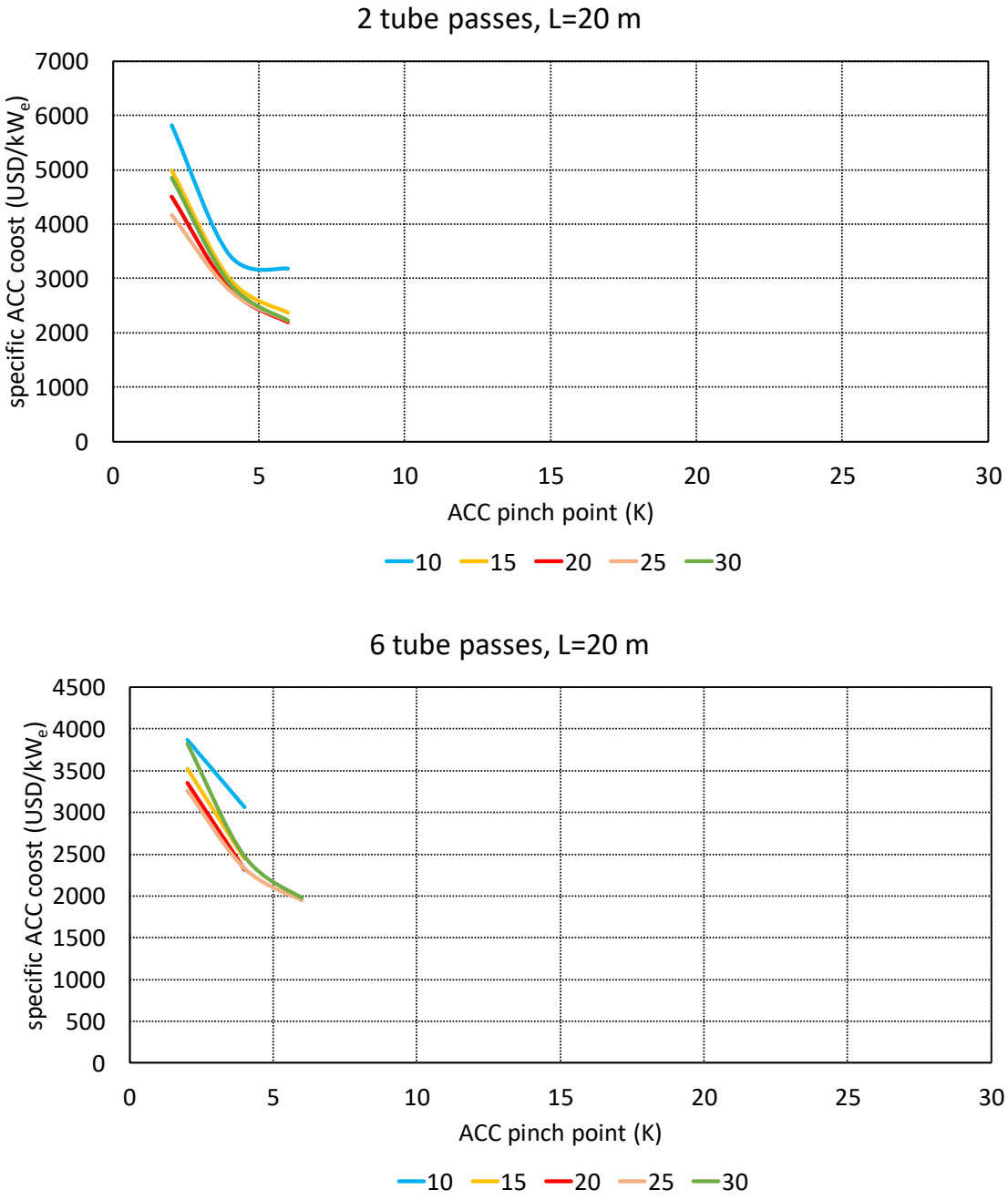

Figure 3.24: Specific ACC cost vs ACC pinch point for 2 & 6 tube pass configuration and 20m total tube length. Each curve corresponds to a different air temperature rise

3.4 Optimal design point for each scenario

In this section, the specific ACC cost will be further analysed in comparison with the ORC design ($PP_{ACC}, \Delta T_{air}$)and geometry variables (L_t, N_{tp}), that the parametric investigation was carried out . $C_{ACC,sp}$ is the parameter that combines both technical and economic factors, as analyzed in the previous diagrams. In this section the optimal design points for each scenario of geometry configuration will be examined. More specifically, for each combination of tube length (L_t) and number of tube passes (N_{tp}), the point that results in lower $C_{ACC,sp}$ will be collected for each PP_{ACC}. Each point will correspond in the respective ΔT_{air} that minimizes the $C_{ACC,sp}$. In Table 3.3 the set of poinst are presented for each scenario and PP_{ACC}.

Table 3.1: Optimal points that minimize Specific ACC cost for *L_t =10m*

	L_t=10m, N_{tp}=6		***L_t=10m, N_{tp}=2***	
Pinch Point (K)	ΔT_{air} (K)	Specific ACC cost *(USD/kW$_e$)*	ΔT_{air} *(K)*	Specific ACC cost *(USD/kW$_e$)*
4	20	2560	-	-
6	20	2057	30	2655
8	30	1786	30	2141
10	30	1605	30	1840
12	30	1504	30	1660
14	30	1459	30	1552
16	30	1466	30	1500
18	30	1524	30	1498
20	30	1655	30	1551

Table 3.2: Optimal points that minimize Specific ACC cost for *L_t =15m*

	Lt=15m, Ntp=6		**Lt=15m, Ntp=2**	
Pinch Point (K)	ΔT_{air} (K)	Specific ACC cost (USD/kW$_e$)	ΔT_{air} (K)	Specific ACC cost (USD/kW$_e$)
2	25	3406	-	-
4	20	2394	25	3039
6	20	1975	25	2338

8	30	1727	30	1950
10	30	1568	30	1716
12	-	-	30	1577

Table 3.3: Optimal points that minimize Specific ACC cost for L_t =20m

	Lt=20m, Ntp=6		Lt=20m, Ntp=2	
Pinch Point (K)	ΔT_{air} (K)	Specific ACC cost (USD/kW$_e$)	ΔT_{air} (K)	Specific ACC cost (USD/kW$_e$)
2	25	3259	25	4168
4	20	2315	25	2781
6	25	1946	20	2189

For a better visualisation of the results, Figure 3.25 and Figure 3.26 will be thoroughly explained in order to explain and interpret in detail the relationship between specific ACC Costs and the 4 design parameters of the parametric investigation.

In Figure 3.25 the Specific ACC cost vs the pinch point is displayed. Each curve represents a combination of tube length L_t and the number of tube passes N_{tp}. Each point corresponds to the respective ΔT_{air} that the $C_{ACC,sp}$ is minimum.

Right above Figure 3.26 illustrates the ΔT_{air} vs PP_{ACC} for each optimal point of $C_{ACC,sp}$. Each curve represents a combination of tube length L_t and the number of tube passes N_{tp}. Each point corresponds to the respective minimum $C_{ACC,sp}$ for each pinch point.

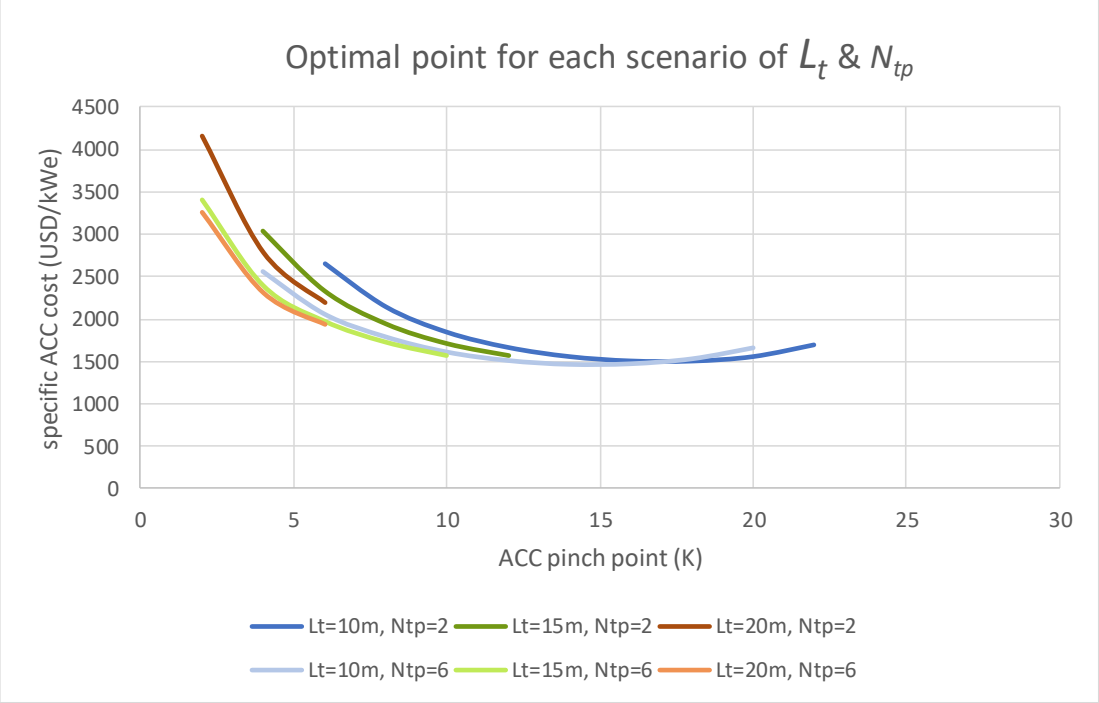

Figure 3.25: Minimum specific ACC cost vs ACC pinch point for each L_t and N_{tp} configuration

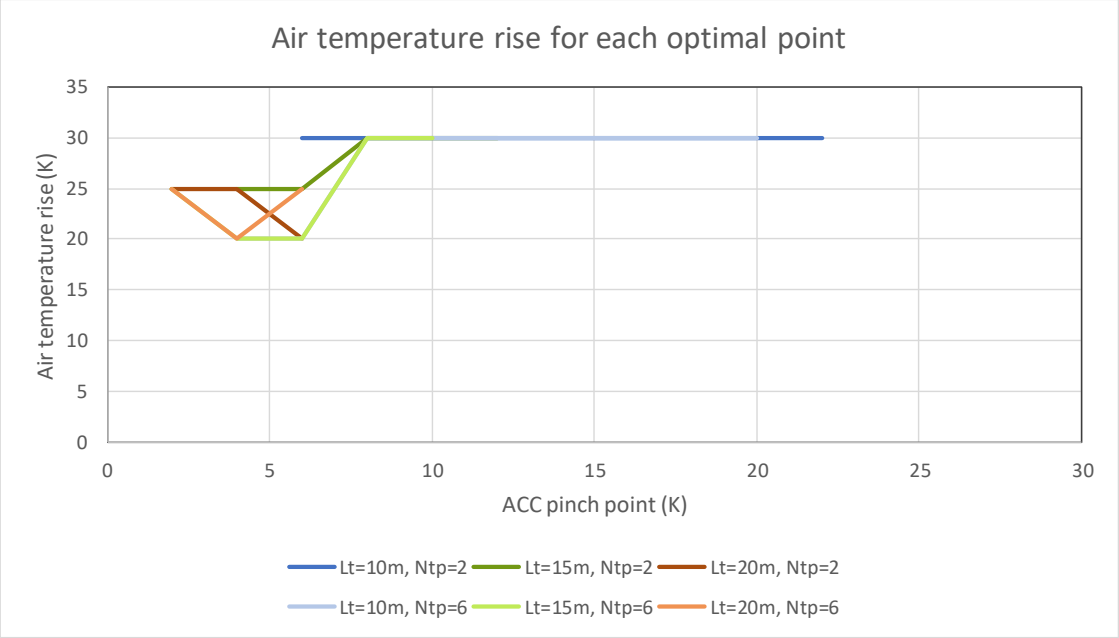

Figure 3.26: Air temperature rise vs ACC pinch point for each L_t and N_{tp} configuration that corresponds to minimum specific ACC cost

The analysis of these 2 diagramms summarises the key findings of the parametric investigation.

For each L_t it is observed that $C_{ACC,sp}$ is higher for $N_{tp} = 2$. N_{tp} effects on the heat transfer coefficient resulting in higher A_{ACC} for 2 tube passes, as explained in section 3.1. Therefore, due to the higher A_{ACC}, the $C_{ACC,sp}$ will have increased values too. For the same N_{tp}, the $C_{ACC,sp}$ is higher for smaller L_t. Again longer $\mathrm{L_t}$ effects on the A_{ACC} resulting in smaller required A_{ACC} and $C_{ACC,sp}$. These observations make more clear the impact of the of the geometry in the final $C_{ACC,sp}$. Changes in the geometry impact he the specific cost of the ACC through the A_{ACC}.

Regarding geometry, It can also be observed that the acceptable PP_{ACC} ranges (considering the constraints taken into account in the ACC model) of the curves are smaller and transposed toward smaller pinch point values as the L_t increases. This happens because of the constraint for the aspect ratio of the ACC. For longer $\mathrm{L_t}$, the required A_{ACC} is obtained with fewer tubes in the x dimension and thus with lower ACC widths. For higher PP_{ACC} values, the required A_{ACC} is lower, therefore, the ACC sizing model tends to produce designs with even smaller ACC widths, which are not acceptable based on the aspect ratio constraint.

At each scenario of L_t & N_{tp} the specific ACC cost decreases as the PP_{ACC} increases. As explained earlier the decrease in PP_{ACC} results in higher net electrical power output, however at the same time C_{ACC} increases with a steeper pace having a bigger influence in the $C_{ACC,sp}$. The global minimum point of all scenarios is detected at $\boldsymbol{PP_{ACC} = 14\ K}$ with a minimum value of $\boldsymbol{C_{ACC,sp} = 1459\ USD/Kw_e}$ and $\boldsymbol{\Delta T_{air} = 30\ K}$. Still, this number is extremely high for actual ORC systems. As it was mentioned earlier, this phenomenon is due to the correlation used and the +50% increase in the CEPCI.

All the optimal points of Figure 3.25 correspond to a $\Delta \mathrm{T}_{air}$ in which the $C_{ACC,sp}$ at each particular pinch point is minimum. In Figure 3.25 it is clear that for pinch points higher than 8 K the only ΔT_{air} minimizing $C_{ACC,sp}$ is the 30 K air temperature rise. This corresponds to $L_t = 10\ \&\ 15\ m$, as $L_t = 20m$ doesn't have feasible solutions in these PP_{ACC}ranges. The reason is that as ΔT_{air} is increased, the $P_{e,ACC,fan}$ tends and the net power output is reduced at a much lower rate for increasing PP_{ACC} values. Therefore, for higher ΔT_{air} values, as the PP_{ACC} is increased, the penalty in the net power output is not that significant, while the A_{ACC} is reduced at the same rate. For small PP_{ACC} it is observed that that the optimal point is achieved in lower ΔT_{air} , yet remaining high at 20-25K. There is no clear correlation on the behavior of the curves. It might be explained from the fact that in really small PP_{ACC}, the curves have really steep slopes, however these points are related with extremely high costs and therefore they are not, part of the general optimal solution.

As a conclusion of this analysis of the $C_{ACC,sp}$ related to the design variables of the parametric investigation it can be concluded that optimal design points are met in PP_{ACC} =12-18K , $\Delta T_{air} = 30K$ and $L_t = 10m$. The costs are yet extremely high for ORC systems and geometry though it affect $C_{ACC,sp}$ it is not so influential as PP_{ACC} and ΔT_{air}.

4. Conclusions

In the current study, a techno-economic evaluation of the impact of the air-cooled condensers in ORC systems was carried out. A unified sizing model for the ACC was developed and a detailed parametric investigation was presented to detect the key design variables of the ACC modeling and its integration into the ORC system. Observing the results of the overall system, the following conclusions and observations are made:

- An inrease in $\boldsymbol{\Delta T_{air}}$, results in a significant decrease of $\dot{m}_{air}$. Because of the significant increase, ΔP_{air} along with $P_{e,ACC,fan}$ are decreased. ΔT_{air} also effects on the condensation temperature/pressure of the cycle with an insignificant increase in $\dot{Q}_{ACC}$ and affectson of ΔT_{lm}.
- An increase in $\boldsymbol{PP_{ACC}}$ also effects insignificantly on $\dot{Q}_{ACC}$, however there is a notable increase in ΔT_{lm} that results in a decreased A_{ACC}.
- For $\boldsymbol{N_{tp}} = 2$ the working fluid stream is divided into 3 different streams, resulting in decreased values of heat transfer coefficient (U), and because $\dot{Q}_{ACC}$ remains the same, A_{ACC} is higher.
- $\boldsymbol{L_t}$ also effects on the U. Longer tubes are assassociated with bigger values of U and thus smaller A_{ACC}.
- For PP_{ACC} values below 10 K, A_{ACC} increases dramatically by almost 100% for a further decrease of the pinch point value by 5 K.
- The acceptable PP_{ACC} range of the curves are smaller and transposed toward smaller pinch point values as L_t increases. This happens because of the constraint for the aspect ratio of the ACC. Because L_t is longer, the required A_{ACC} is obtained with fewer tubes in the x dimension and thus with lower ACC widths.
- $C_{ACC,sp}$ combines both technical and economic criteria in the parametric investigation. Optimal PP_{ACC} ranges between a minimum of 8-10 K to a maximum of around 15 K for ΔT_{air} values of 20 K and 30 K, respectively. The global minimum of the specific ACC cost appears for the highest ΔT_{air} and is equal to around 1500 €/kW$_e$
- ACC costs are extemely high compared to the typical investment costs of ORC systems due to the +50% increase in the CEPCI.

5. Future Recommendations

The results of this study lead to the potential of further system's investigation. Some ideas for future work are presented below:

- Investigation of the pressure drop on the organic fluid for different geometry configurations and design variables of the ORC system.
- Further investigation of the surrogate model of the Correction factor in the desuperheating section for the calculation of the heat transfer coefficient.
- Creation of a sizing model for V-type condensers in ORC systems
- Technoeconomic analysis and comparison of different ACC types

6. References

1. *H. M. D. P. Herath, M. A. Wijewardane, R. A. C. P. Ranasinghe και J. G. A. S. Jayasekera, «Working Fluid Selection of Organic Rankine Cycles,» Energy Report, τόμ. 6, 2020.*
2. *K. Darvish, M. A. Ehyaei, F. Atabi και M. A. Rosen, «Selection of Optimum Working Fluid for Organic Rankine Cycles by Exergy and Exergy-Economic Analyses,» Sustainability, τόμ. 7, 2015.*
3. *Wieland, C., Dawo, F., Schifflechner, C., & Astolfi, M. (2021). Market report on Organic Rankine Cycle power systems: recent developments and outlook. In Proceedings of the 6th International Seminar on ORC Power Systems.*
4. *Han S, Seo J, Choi BS. Development of a 200 kW ORC radial turbine for waste heat recovery. J Mech Sci Technol 2014;28:5231–41.*
5. *"TURBODEN - ORC systems, gas expander and large heat pump." https://www.turboden.com/ (accessed Feb. 20, 2024).*
6. *S. Lecompte, H. Huisseune, M. van den Broek, B. Vanslambrouck, and M. De Paepe, "Review of organic Rankine cycle (ORC) architectures for waste heat recovery," Renew. Sustain. Energy Rev., vol. 47, pp. 448–461, Jul. 2015, doi: 10.1016/j.rser.2015.03.089.*
7. *Braimakis, K., et al., Comparison of Environmentally Friendly Working Fluids for Organic Rankine Cycles: From Numerical to Experimental Techniques. 2017. p. 377-426.*
8. *Quoilin, S., et al., Techno-economic survey of Organic Rankine Cycle (ORC) systems. Renewable and Sustainable Energy Reviews, 2013. 22: p. 168-186.*
9. *Jiménez-García JC, Ruiz A, Pacheco-Reyes A, Rivera W. A Comprehensive Review of Organic Rankine Cycles. Processes. 2023; 11(7):1982. https://doi.org/10.3390/pr11071982.*
10. *Karellas, S., et al., Solar Cooling Technologies. 2018: CRC Press.*
11. *A. Guercio and R. Bini, "Biomass-fired Organic Rankine Cycle combined heat and power systems," in Organic Rankine Cycle (ORC) Power Systems, E. Macchi and M. Astolfi, Eds. Elsevier, 2017, pp. 527–567.*
12. *A. Rentizelas, S. Karellas, E. Kakaras, and I. Tatsiopoulos, "Comparative techno-economic analysis of ORC and gasification for bioenergy applications," Energy Convers. Manag., vol. 50, no. 3, pp. 674–681, Mar. 2009, doi: 10.1016/j.enconman.2008.10.008.*
13. *S. R. Wood and P. N. Rowley, "A techno-economic analysis of small-scale, biomass-fuelled combined heat and power for community housing," Biomass and Bioenergy, vol. 35, no. 9, pp. 3849–3858, Oct. 2011, doi: 10.1016/j.biombioe.2011.04.040.*
14. *ΤΕΧΝΙΚΟ ΕΠΙΜΕΛΗΤΗΡΙΟ ΕΛΛΑΔΑΣ, "Συμπαραγωγη Ηλεκτρισμου, Θερμοτητας & Ψυξης: Εγκαταστασεις Σε Κτηρια, Τεχνικη Οδηγια Τεχνικου Επιμελητηριου Ελλαδας Τ.Ο.Τ.Ε.Ε. 20701-5/2017," Αθήνα, 2017.*

15. *ΦΕΚ Β΄4893, "Κύρωση του Εθνικού Σχεδίου για την Ενέργεια και το Κλίμα (ΕΣΕΚ)," 2019.*
16. *Colonna, P., et al., Organic Rankine Cycle Power Systems: From the Concept to Current Technology, Applications, and an Outlook to the Future. Journal of Engineering for Gas Turbines and Power, 2015. 137(10): p. 100801-100801-19.*
17. *Tartière T, Astolfi M. A World Overview of the Organic Rankine Cycle Market. Energy Procedia. 2017;129:2-9.*
18. *Lecompte S, Huisseune H, van den Broek M, Vanslambrouck B, De Paepe M. Review of organic Rankine cycle (ORC) architectures for waste heat recovery. Renewable and Sustainable Energy Reviews. 2015;47:448-61.*
19. *Lion S, Michos CN, Vlaskos I, Rouaud C, Taccani R. A review of waste heat recovery and Organic Rankine Cycles (ORC) in on-off highway vehicle Heavy Duty Diesel Engine applications. Renewable and Sustainable Energy Reviews. 2017;79:691-708.*
20. *Zhou, X., et al., Thermal Investigations into an Organic Rankine Cycle (ORC) System Utilizing Low Grade Waste Heat Sources. Procedia Engineering, 2017. 205: p. 4142-4148.*
21. *Exergy: Organic Rankine Cycle manufacturer. (2024, January 25). Exergy. https://www.exergy-orc.com/.*
22. *Tzivanidis, C., Bellos, E., & Antonopoulos, K. A. (2016). Energetic and financial investigation of a stand-alone solar-thermal Organic Rankine Cycle power plant. Energy conversion and management, 126, 421-433.*
23. *Douvartzides, S. and I. Karmalis. Working fluid selection for the Organic Rankine Cycle (ORC) exhaust heat recovery of an internal combustion engine power plant. in IOP Conference Series: Materials Science and Engineering. 2016. IOP Publishing.*
24. *Andersen, S.O., et al., The global search and commercialization of alternatives and substitutes for ozone-depleting substances. Comptes Rendus Geoscience, 2018. 350(7): p. 410-424.*
25. *Ε. Κακαράς and Σ. Καρέλλας, Αποκεντρωμένα Θερμικά Συστήματα. Αθήνα: Εκδόσεις Τσότρας, 2015.*
26. *U. Grigull, J. Straub, and P. Schiebener, Steam Tables in SI-Units / Wasserdampftafeln. Berlin, Heidelberg: Springer Berlin Heidelberg, 1990.*
27. *L. J. Brasz και W. M. Bilbow, «Ranking of Working Fluids for Organic Rankine Cycle Applications,» σε International Refrigeration and Air Conditioning Conference, 2004.*
28. *Sharma, P. K., & Mullick, S. C. (2003). Air-Cooled Condensers and Cooling Towers: Thermal Flow Performance Evaluation and Design, Volume 1. CRC Press.*
29. *Wang, L., et al. (2018). Experimental investigation on the performance characteristics of an air-cooled condenser for organic Rankine cycle system. Applied Thermal Engineering, 129, 1122-1131.*
30. *Kim, H. Y., & Kim, M. H. (2019). Performance evaluation of finned-tube air-cooled condensers for transcritical CO2 refrigeration cycles. Applied Thermal Engineering, 158, 113760.*

31. *Mohan, A. L., Kumar, A., & Ramalingam, V. (2015). Heat transfer and pressure drop analysis in plate finned tube heat exchangers with different fin geometries. Journal of Mechanical Science and Technology, 29(8), 3475-3482.*
32. *Illyés, V., Morosini, E., Doninelli, M., David, P. L., Guerif, X., Werner, A., ... & Manzolini, G. (2022, June). Design of an air-cooled condenser for co2-based mixtures: model development, validation and heat exchange gain with internal microfins. In Turbo Expo: Power for Land, Sea, and Air (Vol. 86083, p. V009T28A016). American Society of Mechanical Engineers.*
33. *Eckels, S. J. (2010). Heat exchanger design handbook. CRC Press.*
34. *Peng, N., Zhang, L. Z., & Wang, L. B. (2019). Performance analysis of air-cooled condenser in an organic Rankine cycle system for engine waste heat recovery. Energy Conversion and Management, 196, 951-962.*
35. *Sawant, A. P., & Ghajar, A. J. (2015). Effect of fin geometry on the performance of air-cooled compact heat exchangers. Journal of Heat Transfer, 137(7), 071302.*
36. *Kuppan, T., 2013. Heat Exchanger Design Handbook. CRC Press doi: 10.1201/b14877.*
37. *Incropera, F. P., & DeWitt, D. P. (2002). Introduction to heat transfer. John Wiley & Sons.*
38. *Modine Coolers - ECO and Coiltech Heat Transfer. (2022, March 9). Modine Coolers. https://www.modinecoolers.com/.*
39. *Welch, M., & Pym, A. (2015). Improving the flexibility and efficiency of gas turbine-based distributed power plants. Power Eng, 119(9), 1.*
40. *Versteeg, H. K., & Malalasekera, W. (2007). An introduction to computational fluid dynamics: the finite volume method. Pearson Education.*
41. *MathWorks - Makers of MATLAB and Simulink. (n.d.). MATLAB & Simulink. https://www.mathworks.com.*
42. *National Institute of Standards and Technology. (2024). REFPROP Version 10. NIST Standard Reference Database. Retrieved 15 February, 2024, from https://www.nist.gov/srd/refprop.*
43. *Serth, R.W., 2007. Process Heat Transfer: Principles and Applications. Elsevier doi: 10.1016/b978- 0- 12- 373588- 1.x50 0 0-1.*
44. *Ganguli, A. , Tung, S.S. , Taborek, J. , 1985. Parametric Study of Air-Cooled Heat Exchanger Finned Tube Geometry. In: AIChE Symp. Ser., vol. 81. Denver, CO, pp. 122–128 . 245*
45. *Gnielinski, V. , 1976. New Equations for Heat and Mass Transfer in Turbulent Pipe and Channel Flow. Int. Chem. Eng. 16 (2), 359–368*
46. *Gnielinski, V. , 1983. Heat Exchanger Design Handbook, vol. 1. Hemisphere Washington, DC, p. 5 . chapter Forced Convection in Ducts Gómez-Aláez, S.L., Brizzi, V., Alfani, D., Silva, P., Gio.*
47. *McQuiston, F. C. and D. R. Tree, Optimum space envelopes of the finned tube heat transfer surface,Trans. ASHRAE, 78, 144–152, 1972.*

48. *Langiu, M., Dahmen, M., & Mitsos, A. (2022). Simultaneous optimization of design and operation of an air-cooled geothermal ORC under consideration of multiple operating points. Computers & Chemical Engineering, 161, 107745.*
49. *Shah, M.M., 1979. A General Correlation for Heat Transfer During Film Condensation Inside Pipes. Int. J. Heat Mass Transf. 22 (4), 547–556. doi: 10.1016/ 0 017-9310(79)90 058-9*
50. *Shah, M.M., 2009. An Improved and Extended General Correlation for Heat Transfer During Condensation in Plain Tubes. HVAC&R Res. 15 (5), 889–913. doi: 10.1080/10789669.2009.10390871*
51. *Stasiulevicius, J., Skrinska, A., & Zukauskas, A. (1988). Heat transfer of finned tube bundles in crossflow.*
52. *Zukauskas, A. (1989). High-performance single-phase heat exchangers (Revised and enlarged edition). New York.*
53. *Stephan, P., & Atlas, V. H. (2010). B1 Fundamentals of Heat Transfer'. VDI Heat Atlas, 15-30.*
54. *Astolfi, M. (2014). An innovative approach for the techno-economic optimization of organic rankine cycles.*
55. *Decagone. (2024). Homepage. Retrieved from https://decagone.eu/.*
56. *Ghasemi, H., Paci, M., Tizzanini, A., Mitsos, A., 2013b. Modeling and Optimization of a Binary Geothermal Power Plant. Preprint, available at http://hdl.handle.net/ 1721.1/104031.*